Biomechanical Properties of the Ocular Globe Based on *Ex Vivo* Testing and Multiscale Numerical Modelling

Thesis submitted in accordance with the requirements of the University of Liverpool for the degree of Doctor in Philosophy by

Charles Whitford

July 2016

Primary supervisor:
Professor Ahmed Elsheikh
School of Engineering
University of Liverpool

Secondary supervisor:
Dr Steve Jones
School of Engineering
University of Liverpool

UNIVERSITY OF LIVERPOOL

Biomechanical Properties of the Ocular Globe Based on *Ex Vivo* Testing and Multiscale Numerical Modelling

Thesis submitted in accordance with the requirements of the University of Liverpool for the degree of Doctor in Philosophy by

Charles Whitford

July 2016

Abstract

Humans have been attempting to understand the workings and significance of the eye for at least 2500 years. Some ancient philosophers believed that the eye enabled creatures to see by emitting its own light. The function and structures of the eye became an area of particular interest to doctors in the Islamic Golden Age. In Renaissance Europe the work of thinkers including Kepler and Descartes revolutionised thinking about how the organ worked, but it took several hundred years for the eye to be thoroughly understood. Eyes have long attracted more than purely scientific interest, known even today as the 'windows on the soul'.

The present study is the culmination of quantifying and qualitative experimental and numerical research representing biomechanical behaviour of the human eye.

A new experimental technique for testing intact eye globes in a form that is representative of *in vivo* conditions is developed which is suitable for determining the material properties of the complete outer ocular tunic.

A test rig has been developed to provide closed-loop control of either applied intraocular pressure or resulting apical displacement, measurement of displacements across the external surface of eye globe using high-resolution digital cameras and digital image correlation software, prevention of rigid-body motion and protection of ocular surface from environmental drying. The method has been demonstrated on one human and one porcine eye globe, which were cyclically loaded. Finite element models based on

specimen specific tomography, free from rotational symmetry, were used along with experimental pressure-displacement data in an inverse analysis process to derive the mechanical properties of tissue in different regions of the eye's outer tunic.

The test method enabled monitoring of mechanical response to intraocular pressure variation across the surface of the eye globe. For the two eyes tested, the method showed a gradual change in the sclera's stiffness from a maximum at the limbus to a minimum at the posterior pole, while in the cornea the stiffness was highest at the centre and lowest in the peripheral zone. Further, for both the sclera and cornea, the load-displacement behaviour did not vary significantly between loading cycles.

The first methodology capable of mechanically testing intact eye globes, with applied loads and boundary conditions that closely represent *in vivo* conditions has been introduced. The method enables determination of the regional variation in mechanical behaviour across the ocular surface.

Two numerical models based in continuum mechanics theory have been developed which represent the 3D anisotropic behaviour of the corneal stroma. Experimental data has been gathered from a number of previous studies to provide the basis and calibration parameters for the numerical modelling. The resulting models introduce numerical representation of collagen fibril density and its related regional variation, interlamellar cohesion and age-related stiffening in anisotropic and viscoelastic models of the human cornea. Further, the models incorporate previous modelling developments including representation of lamellae anisotropy and stiffness of the underlying matrix. Wide angle X-ray scattering has provided measured data which quantifies relative fibril anisotropy in the 2D domain. Accurate numerical description of material response to deformation is essential to providing representative simulations of corneal behaviour. Representing experimentally obtained 2D anisotropy and regional density variation in the 3D domain is an essential component of this accuracy. The constitutive model was incorporated into finite element analyses. Combining with inverse analysis, the model

was calibrated to an extensive experimental database of *ex vivo* corneal inflation tests and *ex vivo* corneal shear tests. This model represented stiffness of the underlying matrix which is $2-3$ orders of magnitude lower than the mechanical response representing the collagen fibrils in the lamellae. The presented model, along with its age dependent material coefficients, allows finite element modelling for an individual patient with material stiffness approximated based on their age. This has great potential to be used in both daily clinical practice for the planning and optimisation of corrective procedures and in pre-clinical optimisation of diagnostic procedures.

The second constitutive numerical model based on the continuum mechanics theory was developed which extended the representation of the model above to include both age-related viscoelastic stiffening behaviour of the human cornea. Experimental data gathered from a number of previous studies on 48 *ex vivo* human cornea (inflation and shear tests) enabled numerical model calibration. The present study suggests that stiffness parallel to the lamellae of the cornea approximately doubles from an increase in strain-rate of $0.5-5\%$/min. While the underlying stromal matrix provides a stiffness $2-3$ orders of magnitude lower than the lamellae. The model has been simultaneously calibrated to within 5% error across three age groups ranging from $50-95$, multiple strain-rates and multiple loading scenarios. Age and strain-rate dependent material coefficients allow finite element modelling for an individual patient with material stiffness approximated by their age under varying loading scenarios. This present study addresses a significant gap in numerical representation of the cornea and has great potential in both daily clinical practice particularly in highly viscoelastic dependent simulations such as non-contact tomometry.

Related to this thesis, the author has either primarily or secondarily authored the following related journal articles which are included in this thesis in modified forms:

Whitford C. & Elsheikh A., **Corneal Biomechanics Testing Methods**, May 2014, Chinese Journal of Optometry and Ophthalmology Visual Science;

Whitford C., Joda A., Jones S., Bao F., Rama P. & Elsheikh A., **Ex-vivo Testing of Intact Eye Globes Under Inflation Conditions to Determine Regional Variation of Mechanical Stiffness**, July 2016, Eye and Vision.

Elsheikh, A., **Whitford, C.**, Hamarashid, R., Kassem, W., Joda, A., Büchler, P., **Stress free configuration of the human eye**. Febuary 2013, Medical Engineering & Physics.

Yu J., Bao F., Feng Y., **Whitford C.**, Ye T., Huang Y., Wang Q., Elsheikh A., **Assessment of Corneal Biomechanical Behavior Under Posterior and Anterior Pressure**. January 2013, Journal of Refractive Surgery.

Whitford C., Studer H., Boote K., Meek K.M. & Elsheikh A., **Biomechanical Model of the Human Cornea: Considering Shear Stiffness and Regional Variation of Collagen Anisotropy and Density**, Feb 2015, Journal of the Mechanical Behavior of Biomedical Materials.

Elsheikh A., McMonnies C.W., **Whitford C.** & Boneham G.C., **In-vivo study of Corneal Responses to Increased Intraocular Pressure**, 2015, Eye and Vision.

An additional journal publication has been prepared from the content in this present study:

Whitford C., Movchan N. & Elsheikh A., **A Viscoelastic Hyperelastic Anisotropic Model of the Human Cornea**.

Further, two book chapters have been published which related to this thesis:

Whitford C., Studer H., Boote C., Meek K. & Elsheikh A., **Modelo Biomecnico de**

la Crnea Humana Considerando la Variacin Regional de la Anisotropa, la Densidad y la Cohesin Interlaminar de las Fibrillas de Colgeno, in **Biomecnica y Arquitectura Corneal**, May 2014.

Geraghty B., **Whitford C.**, Boote C., Akhtar R,. & Elsheikh A., **Age-Related Variation in the Biomechanical and Structural Properties of the Corneo-Scleral Tunic**, in **Mechanical Properties of Ageing Soft Tissues**, January 2015.

In addition, a number of conference proceedings have been published.

Acknowledgements

Firstly I would like to thank my mum, Lesley. My mum has supported and guided me throughout my life. She supported me academically from the start of my life which was often not the easiest task. As someone who suffers from extreme dyslexia in a schooling environment which did not recognise the condition, my school days were a significant challenge. At times, my mum was the only person who supported me and fought for my condition to be recognised.

With the deepest gratitude I thank both my brother Robert and my wonderful sister-in-law Gill. There are many ways in which they have contributed to my studies. My older brother Robert, as a mathematics teacher, tutored me through my school years and beyond with an an incredible ability to teach. Both Robert and Gill where also there for me during my undergraduate degree, providing invaluable support without which I may not have been able to continue my studies.

I would like to thank my friend Sophie for grammatical proof reading my thesis. Sophie's literary knowledge is only matched by her wit which kept a smile on my face while reading her reviews.

I would also like to thank my internal examiner Prof. Yuyuan Zhao and my external examiners Dr Messaoud Saidani and Dr Carlo Knupp for their valuable time, constructive questioning and comments.

With the greatest respect I wish to thank my supervisors Ahmed and Steve. Steve has supported my at the university for nearly 10 years and continues to do so as my professional mentor. Steve has always inspired me with the highest level of professionalism. Steve supported me in gaining the opportunity to undertake this PhD at a time when I was unknown to my primary supervisor Ahmed. I wish Steve all the best in his forthcoming retirement.

I have huge appreciation and gratitude for my primary supervisor Ahmed for the opportunity to undertake this PhD and the support and inspiration he has provided along the way. My career and future has been greatly altered in the best possible way from the opportunities Ahmed has provided me. At the beginning of this doctorate I could not have imagined a more interesting field of study to engage in.

Summer and Skye... where do I begin... I will love you both with every part of my soul and I look forward to being a part of the rest of your lives. At the time of submitting this thesis you are eight and six years-old and you are growing up as beautiful people. The pride I have in you, and the pride I feel to to be your daddy, is immense. You have done more for me that you will ever realise. One of the primary reasons I decided to undertake my doctorate was so you both could see the potential that I know you both have. I will be there to support you in every way I can, in whatever it is you choose to do with your lives. This thesis is dedicated to you both.
I love you two little girls to the stars and back.
Lots of love, Daddy $\times \times \times$

Contents

Notation

Symbols

A	area
E	Young's modulus
e	error
F	load
h	height
G	relaxation function
K	stiffness
k	proportional gain
$\bar{I}$	strain invariants
J	product of the three principal stretches
L	linearity factor
l	length
N	order - relating to multi-order equations
P	pressure
PV	process variable
p	numerical parameter
S	first Piola-Kirchoff stress
SP	setpoint

U	material constitutive relating to volume change
w	width
z	distance for the centreline
$\mathbf{C}$	right Cauchy-Green tensor
$\boldsymbol{\mathcal{D}}$	internal dissipation of stresses
$\mathbf{D}$	stiffness tensor
$\mathbf{E}$	Green strain tensor
$\mathbf{F}$	deformation gradient tensor
$\boldsymbol{\mathcal{H}}$	stress history
$\mathbf{I}$	unit tensor
$\mathbb{P}$	4^{th} order projection tensor
$\mathbf{Q}$	non-equilibrium stresses
$\mathbf{R}$	rigid-body motion
$\mathbf{S}$	second Piola-Kirchoff stress tensor
α	material coefficient
β	non-dimensional strain energy factor
Γ	internal variables of viscoelasticity
γ	constitutive numerical parameter relating to non-linearity
δ	deformation
ϵ	strain
ζ	global collagen fibril density function
η	rotationally symmetric global collagen fibril density function
θ	azimuthal angle in the spherical coordinate system
λ	stretch
μ	constitutive numerical parameter relating to stiffness

ν	Poisson's ratio
σ	stress
τ	time-dimensional strain energy factor
ϕ	zenith / polar angle in the spherical coordinate system
χ	local anisotropic collagen fibril density function
ψ	strain energy
Ω	configuration
ω	angle of stiffness distribution

Abbreviations

BC	before Christ
CCT	central corneal thickness
DIC	digital image correlation
FEA	finite element analysis
FEM	finite element model
ILC	interlamellae cohesion - relating to fibrils bridging lamellae
IOP	intraocular pressure
OPA	ocular pulse amplitude
PCT	peripheral corneal thickness
PID	proportional differential integral
RMS	root mean square - relating to measurement of error
S-I	superior - inferior axis
SAXS	small-angle X-ray scattering
T-N	temporal - nasal axis
WAXS	wide-angle X-ray scattering

List of Figures

Chapter 1

Introduction

1.1 Background

Human eyes are extremely sophisticated organs, allowing us to see the world around us by characterising the shapes and colours of objects in our environment. They are able to adapt to variation in object position and changes in light conditions. Acting as a pair, they allow us to see the world in 3 dimensions, perceiving depth and scale.

The importance of sight relative to our other senses is subjective opinion. However, many regard it as the most important sense. Plato (*c.*400 BC) stated,
"The sight in my opinion is the source of greatest benefit for us, for had we never seen the stars and the sun and the heaven, none of the words we have spoken about the universe would ever have been uttered" (Plato, 1971)

[1]As a sense of such importance, its understanding and preservation has attracted a large amount of investigation over thousands of years. Plato, and other pre-Socratic Greek philosophers such as Empedocles (*c.*500 BC), were the first known theorists of the eye. These ancient thinkers believed the eye contained a mysterious and divine

[1]The following brief history of ocular science was gleaned from a number of sources including: Bragg et al. (2014); Darrigol (2012); Huff (2003); Ings (2008); Sabra (1981)

illuminating fire. The sense of sight was believed to be similar to touch, where this illuminating fire would reach out of the eye perceiving the world around the subject. This concept is known as extramission, or emission, theory.

Euclid of Alexandria ($c.300$ BC) was the first to consider the optics of the eye but also followed the theories of extramission introduced by his predecessors[2]. Euclid considered that light came from a point of a cone within the eye and, with this idea, calculated angles of incidence and reflection. Later, early medieval researchers were able to prove that extramission could not be the mechanism of sight. Despite this, as late as the 13^{th} century, philosophers such as Roger Bacon included extramission in their theories of optics. It is now known that extramission is not the process of vision. However, Euclid's calculations worked independently of the direction of light though the eye and therefore these early attempts to describe the optics provided a strong basis for what followed in later years.

Intromission was another theory held around the time of Euclid. Greek Atomists, such as Aristotle ($c.350$ BC), believed that an object's shape was transmitted into the eye as *idelons* as though the object itself was projected into the eye. At this time the organ of sight was believed to be the crystalline lens. This view was reinforced by the Roman employed, Greek surgeon, Galen ($c.129 - c.199$).

These early ideas were motivated by the pure pursuit of knowledge itself, but also an early desire to treat eye diseases. At this time surgeries for conditions such as cataracts were being explored. Even during these early investigations, it was known that treatment of these disorders would be more successful with a greater understanding of the behaviour of the eye. Aristole's ideas of intramission continued to form the basis of theory for 1500 years. Early medieval scientists also demonstrated that the early ideas of intramission could not be an accurate description. This was achieved through the assessment that objects thousands of years old did not get smaller or change shape, and could therefore not be projecting part of themselves into the eye.

[2]Euclid also gave rise to the method of geometric representation known as Euclidean space

During the 8^{th} to 12^{th} century it was the era of the Islamic world to lead scientific progress in visual science. Intramission theory developed into a theory that light rays passed into the eye transmitting information about an object, rather than part of the object itself. The mathematics used to describe the path of light in relation to the angle of incidence and the refractive index was first accurately described by Ibn Sahl at the Baghdad court in 984 (Rashed, 1990). This mathematical law is now known as *Snell's law* as these concepts were rediscovered during the 15^{th} century by the Dutch astronomer Willebrord Snellius. Rhazes $(854 - 925)$, another Islamic scientist and philosopher, was amongst others of the time who performed cataract surgeries by extracting the opaque crystalline lens from patients. The most celebrated scientist during this Islamic era of dominance in visual science was Alhazen $(c.965 - c.1040)$. Alhazen developed, through many experiments, theories of binocular vision and the interaction of light and the cornea writing detailed descriptions of physiological optics and the anatomy of the eye in the *Book of Optics*.

Johannes Kepler, a German scientist of the early 17^{th} century, focused on optical theory, these studies included the optics of the human eye. Kepler is generally considered to be the first to recognise that images are inverted and reversed by the eye's lens and projected onto the retina. Kepler's motivation was drawn from a desire to understand whether it was possible to make corrections for errors of refraction. In this sense, Kepler was the father of modern refractive correction procedures such as glasses, contact lenses and refractive surgery.

Sir Issac Newton $(1642 - 1726)$ recorded his earliest experiments in notebooks which are now held by the University of Cambridge library. He describes inserting a knitting needle behind his eye globe to investigate the effects on vision. Today we understand that such action would deform the sclera, leading to increased intraocular pressure (potentially of an order of magnitude). This would subsequently deform, most notably, the sections of the ocular vessel with the greatest mechanical compliance - the cornea and

lamina cribrosa, resulting in changes to the visual refractive power of the eye and, potentially, temporary disruption to the transmission of information along the optic nerve.

After Newton, vision science concentrated on sensory aspects including colour perception and the image capturing of the retina. For many years it was believed that an image was captured on the eye in a similar way to photographic film. This led to the inquest of Anne Chapman (victim of the notorious serial killer Jack the Ripper) in 1888 where the jury asked if photographs had been taken of her eyes in order to identify her killer.

Despite thousands of years of research and the development of many successful treatments for various degenerative visual conditions, there are still huge numbers of people who suffer from visual impairment. These conditions include myopia, glaucoma and keratoconus. Myopia is a condition which currently affects up to 84% of the urban East-Asian populations (He et al., 2004; Lin et al., 2001, 2004; Rose et al., 2008) with annually growing numbers. 21% are affected by high-myopia which is characterised by a refractive error over -6 dioptres [3]. The extreme elongation of the eye globe associated with high-myopia does not only degenerate vision but can lead to complete blindness through retinal detachment (Siam, 1969; Baba et al., 2003). Glaucoma is the leading cause of vision loss in the western world, affecting 105 million people globally (Thylefors and Négrel, 1994) including 5.2 million people who are considered blind. There are a number of risk-factors associated with the pathology of this condition which include: age, race, increased intraocular pressure and corneal/sclera stiffening (Brandt, 2004; Broman et al., 2008; Congdon et al., 2006; Leske et al., 2008). Keratoconus (from the Greek *cornea* - *cone* (Oxford English Dictionary, 2014)) affects, for example, 1 in 2000 Americans (Kennedy et al., 1986). This protrusion of the cornea is a result of its mechanical weakening.

It has been suggested that biomechanics did not truly emerge as a distinct field of study until the mid-1960s (Humphrey, 2003). Only in recent decades that biomechan-

[3]Dioptre is a unit for measuring the refractive power of lenses or curved mirrors.

ics has become involved in vision science and as such is in its relative infancy. Despite this relative infancy, there has been particular advancement in the development of biomechanical representation of the human eye. Numerical and mathematical simulations of the response of the ocular vessel to external and internal forces, and changes in mechanical characteristics associated with disease, injury and surgery are of particular interest as they can lead to developments in diagnostic and corrective procedures for many degenerative visual conditions (Elsheikh et al., 2006, 2011a; Ethier et al., 2004; Kapnisis et al., 2009; Norman et al., 2011; Roberts, 2000; Roy and Dupps, 2009, 2011) . Despite advances in biomechanical understanding and representation of the eye globe, there is clearly a great deal of improvement to be made if the above prevalence of degenerative conditions are to be addressed radically.

1.1.1 Anatomy of the Eye

The human eye is a pressurized vessel with a shape that can be described, in its simplest form, as two intersecting spheres (see Figure 1.1). The sclera, being the largest section of the eye globe, is typically white and opaque with an approximated spherical radius of 11.5 mm (adult eye) (Bron and Tripathi, 1998). The transparent cornea, located at the anterior of the eye, is one sixth the size of the sclera with an approximated central spherical radius of 7.87 mm and diameters of 10.6 and 11.75 mm in the nasal-temporal and superior-inferior directions respectively (Dubbelman et al., 2002). The anterior surface curvature of the cornea flattens towards the limbus with a typical asphericity of 0.82[4]. The intersection of the cornea and sclera is called the limbus, or limbal junction, and is a transitional zone with approximate meridional widths of 1.5 and 2 mm in the nasal-temporal and superior-inferior directions, respectively.

The ocular vessel varies with natural human variation, age, region and disease. The central corneal thickness (CCT) of the adult eye is approximately 550 µm (Aghaian et al., 2004; Chen et al., 2009; Doughty and Jonuscheit, 2007) increasing to a pe-

[4]This measurement of asphericity is provided in terms of the shape factor ratio (p) which quantifies the normalised deviation from a prefect spherical surface, from (Baker, 1943)

ripheral corneal thickness (PCT) *c*.670 µm near the limbus (Jonuscheit et al., 2007). Galgauskas et al. (2013) found that CCT thinned from 563 ± 44 SD µm in $20-29$ year olds to 540 ± 35 SD µm in $80-89$ year olds. Due to this change in thickness the posterior cornea's topography can be described by a central spherical radius of 6.40 mm with an asphericity of 0.62 (Dubbelman et al., 2002).

The thickness of the scleral is relatively homogeneous in early ages. However, it begins to thicken in the posterior and thin in the equatorial region from around $4-5$ years-of-age. The thickness in adults ranges from $500-600$ µm at the limbus, thinning to $400-500$ µm at the equator and then thickening to approximately 1000 µm in the posterior region (Norman et al., 2010; Olsen et al., 1998) (see Figure 1.2).

The geometry of the eye globe is significantly more complex than two intersecting spheres of simple asphericity. There is also a great deal of variation in the geometry between individual adult human eyes. These variations are a function of genetics, environment and/or disease. Select variations are discussed in context of the present study throughout this thesis.

The eye is attached to the human body by six extraocular muscles and the optic nerve and is held supported within the orbit (the bony cavities of the skull) by fatty tissue. The six muscles consist of the superior, inferior, nasal and temporal rectus, and the superior and inferior oblique muscles. The rectus muscles are attached to the eye globe by tendons in cardinal locations approximately $5.5-7.7$ mm from the cornea (Bron et al., 1999). They allow the slightly eccentric rotational movement of the eye inside the bony orbit in the longitudinal directions. The superior oblique muscle acts to rotate the eye approximately about the optic axis depressing the nasal side of the eye. The inferior oblique acts to raise the nasal eye by also rotating the eye about the optic axis. The optic nerve has an external diameter of *c*.3 mm and is located 3 and 1 mm from the posterior pole in the nasal and inferior directions respectively (Saude, 1993).

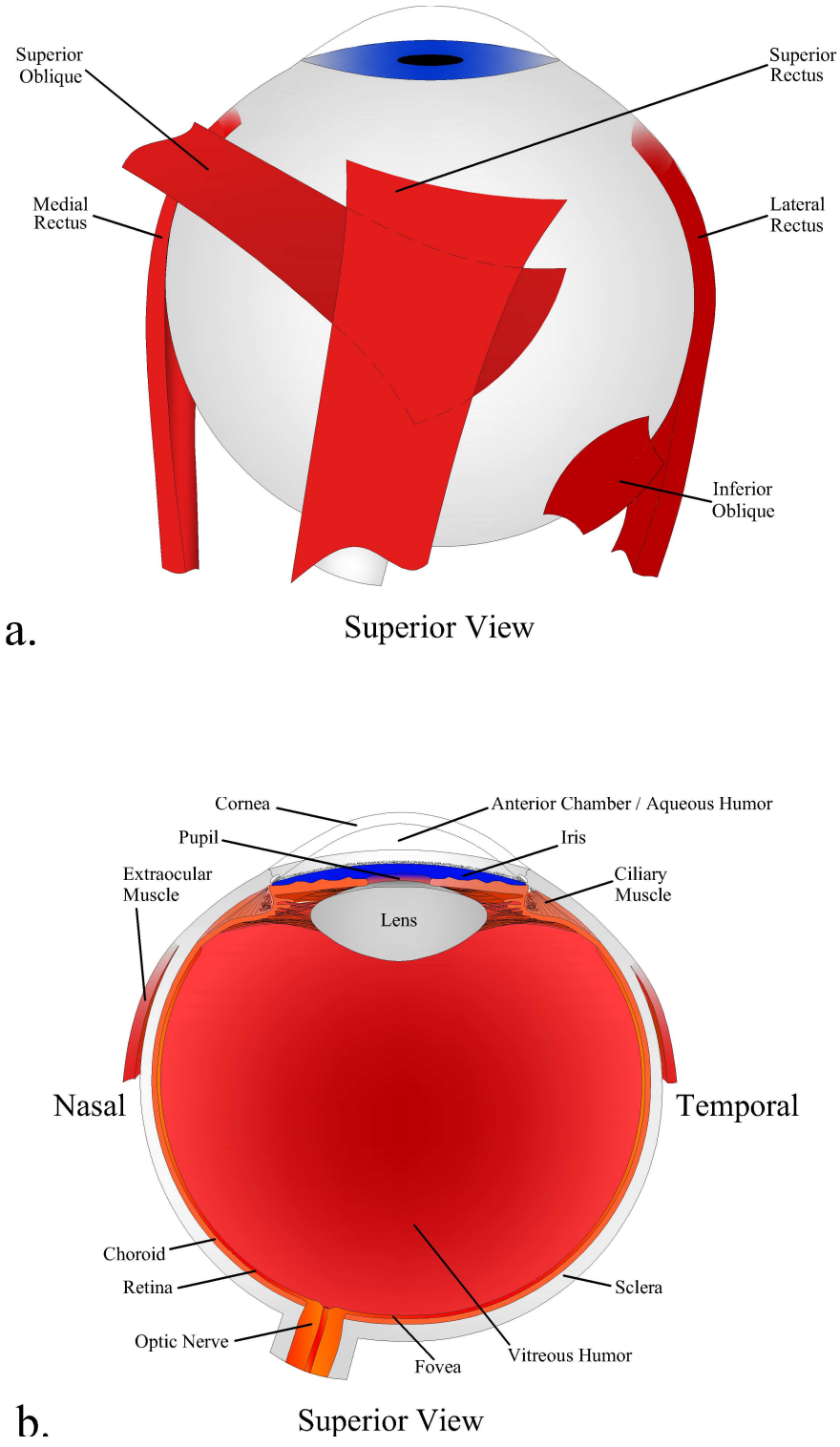

Figure 1.1: Diagram of the human ocular dexter (right) eye from the superior view point. (a) highlights the extraocular muscles. (b) provides a section view of the eye, highlighting the internal arrangement of the eye. Image modified from Geraghty et al. (2015).

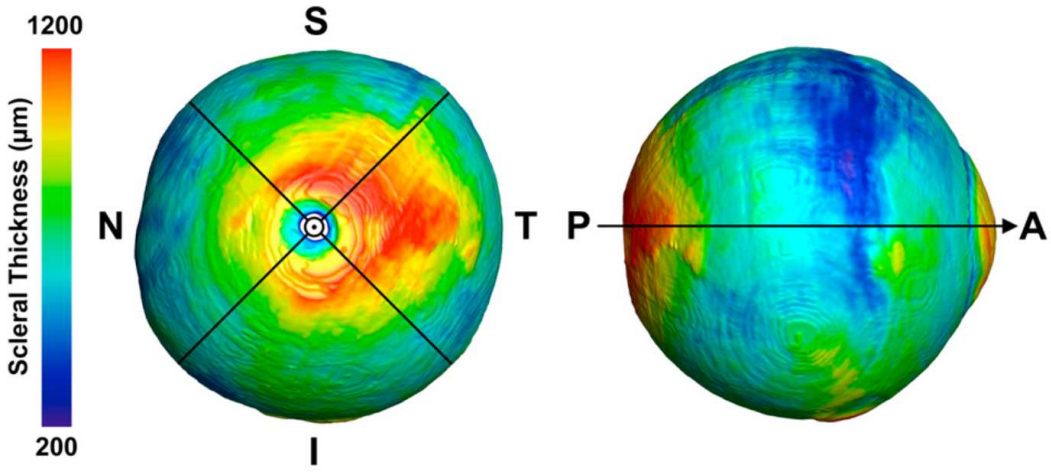

Figure 1.2: Human scleral thickness reported by Norman et al. (2010). The study was completed using micro-MRI.

1.1.2 Layers of the Eye

The Fibrous/Outer Layer

Behind the precorneal tear film there are six distinct tissue layers of the cornea. Arranged from anterior to posterior, these are: the epithelium, Bowman's layer, stroma, Dua's layer (Dua et al., 2013), Descement's membrane and the endothelium.

The epithelium consists of nucleated cells with type IV collagen appearing at the periphery (Bron and Tripathi, 1998) and has been measured by high-frequency ultrasound at 50.7 μm. An experimental study by Elsheikh et al. (2008a) suggested that the contribution to stiffness from the epithelium could be ignored as negligible.

The Bowman's layer is an acellular homogeneous zone $8-14$ μm thick.

The stroma is the dominant layer of the cornea in terms of size and its contribution to mechanical stiffness. At approximately 500 μm thick, it constitutes 90% of the human corneal thickness. This layer consists of over 200 stacked lamellar sheets of predominantly type I collagen fibrils ($50-55$% of dry weight) (Freegard, 1997; Komai and

Ushiki, 1991; Oyster, 1999; Marshall et al., 1993) embedded in a hydrated matrix of proteoglycans, glycoproteins, and keratocytes (Borcherding et al., 1975; Berman, 1991; Cogan, 1951; Marshall et al., 1993; Maurice, 1957, 1969). Smaller quantities of types III, V and VI collagen ($\leq 1\%$, $8-10\%$ and $25-30\%$ of dry weight respectively) are also found in the stroma (Berman, 1991; Marshall et al., 1993). Proteoglycans constitute most of the matrix and have been found in a fixed ratio to collagen in the cornea (Meek and Leonard, 1993).

The recently discovered Dua's layer has been measured between $6.3 - 15.83$ µm thick and made of 5 to 8 thin lamellae of tightly packed collagen bundles running in longitudinal, transverse, and oblique directions (Dua et al., 2013).

The Descement's membrane has been measured between $7.8 - 13.98$ µm (Dua et al., 2013) and predominately consists of tightly packed type IV collagen in a glycoprotien and proteoglycan matrix.

The endothelium is the inner most layer of the cornea. At a thickness of only 4 µm, is formed from polygonal, flattened cells (Zavala et al., 2013).

The sclera consists almost entirely of collagen of which is predominantly collagen type I ($\approx 39\%$ of dry weight) (Keeley et al., 1984) with lesser amounts of types III, V, VI and VIII present ($\approx 11\%$ of dry weight combined) (Keeley et al., 1984; Marshall et al., 1993) and there are no apparent variations in tissue mass between equatorial and posterior regions. The matrix components of the sclera are less than the cornea (Bron and Tripathi, 1998). The most significant variations in the collagen composition between the cornea and sclera is the quantity, diameter and anisotropic arrangement of fibrils, further details of which are presented in Section 1.1.3.

The Mid Layer

The mid layer of the eye, also called the uvea, consists of the choroid, ciliary body and the iris.

The choroid is a vascular membrane laying between the sclera and the retina. It is loosely attached to the sclera, except where it is traversed with vessels and nerves (Saude, 1993).

The ciliary body predominantly comprises of the ciliary process and ciliary muscle. The ciliary muscle is an annular smooth muscle and is dominant in terms of providing mechanical stiffness to the eye globe with respect to the ciliary process. The geometry of the muscle changes with accommodation and age (Burd et al., 2002; Ludwig et al., 1999; Glasser and Kaufman, 1999; Sheppard and Davies, 2010, 2011; Stachs et al., 2006; Strenk et al., 1999). While there is variation in reported geometries, it measures in the region of 4500 μm in width beginning behind the limbus and ending at the scleral spur. Measured anterior, the thickness ranges for a $\approx$ 350 μm, increasing to a maximum of thickness $\approx$ 820 μm at $\approx$ 540 μm from its anterior most point where it thins approximately linearly to a spur at its posterior most location (see Figure 1.3).
The cilary muscle has been hypothesised to provide mechanical stiffness to the eye globe. Literature observing its mechanism is sparse; a letter published in the Journal of Investigative Ophthalmology & Visual Science (Bailey, 2011) calls for "a much needed dialog regarding how the ciliary muscle should be measured". Describing this muscle as; "one of the most understudied structures in the human body". To the author's knowledge, literature exploring the mechanical properties of the ciliary muscle does not exist.

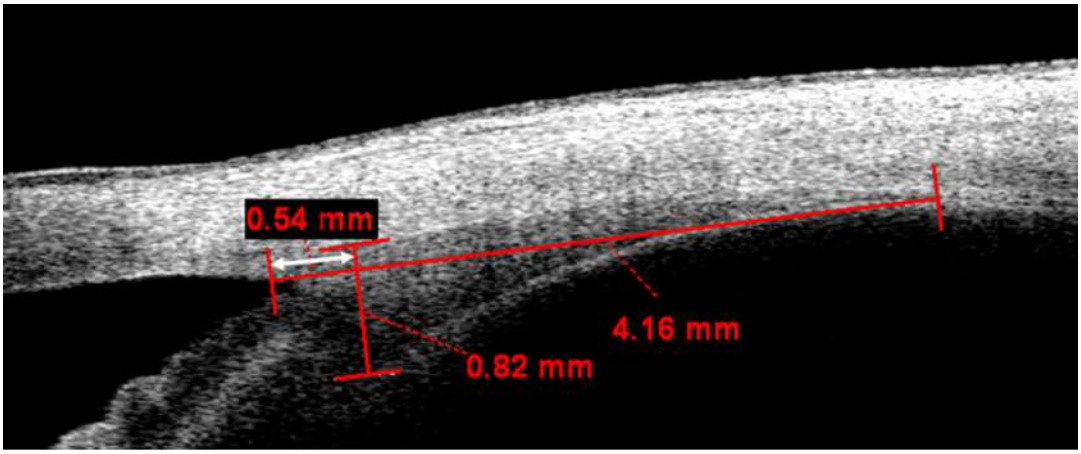

a)

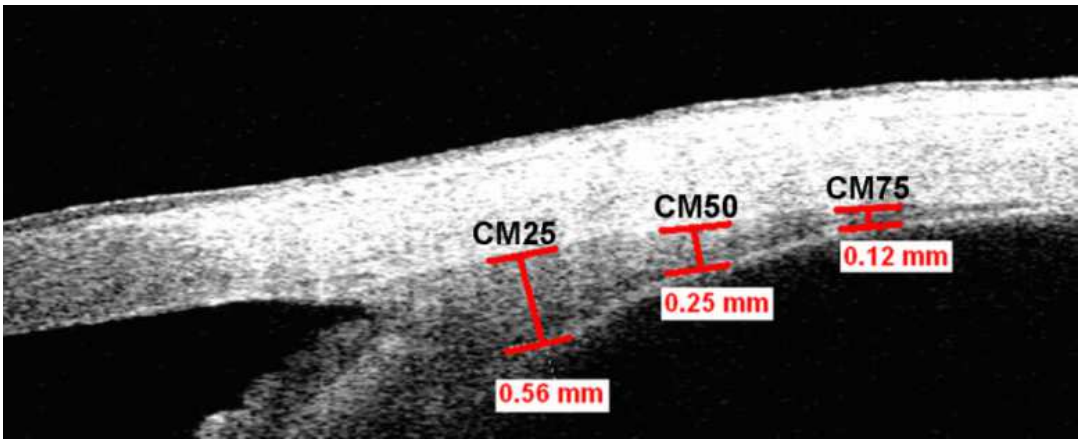

b)

Figure 1.3: Assessment of the ciliary muscle geometry using optical coherence tomography from Sheppard and Davies (2010). (a) provides an assessment of the width of the muscle from the scleral spur to the posterior visible limit (here 4160 µm) and the position of maximum thickness. (b) measurement of the ciliary muscle thickness (same eye as in (a)). CM25, CM50, and CM75 are thickness measurements at 25%, 50% and 75% of the total ciliary muscle width respectively.

Internal Ocular Media and Pressure

The volume of the eye is approximately 6.5 ml (Forrester, 1996). The intraocular media is responsible for maintaining a physiological intraocular pressure between 10 and 20 mmHg (Eysteinsson et al., 2002).

The internal volume of the ocular vessel consists of the transparent aqueous humor, crystalline lens and the vitreous humor. The vitreous humor and crystalline lens, located in the posterior chamber, are relatively stable in their volume. The aqueous humor, which fills the anterior chamber and passes around the vitreous and lens, is secreted by the ciliary process and expelled from the ocular vessel through the trabecular meshwork. It is the regulation of aqueous through this transportation which is responsible for the quasi-static intraocular pressure. As such, blockage of the trabecular meshwork can lead to increased intraocular pressure and glaucoma (Robert, 2007; Tektas and Lütjen-Drecoll, 2009; Tamm, 2009).

To understand the biomechanics of the eye globe it is essential to consider variation and levels of IOP as this is the dominant force acting the ocular vessel during normal physiological conditions. While quasi-static IOP is regulated by aqueous transportation, IOP varies as a result of the dynamic behaviours of body position, ocular pulse amplitude (OPA), accommodation and exercise. Changes in the body orientation, such as inversion, can result in twice baseline IOP (Baskaran et al., 2006). OPA is related to heart rate and produces change of IOP in the range of 1 to 7 mmHg (Kaufmann et al., 2006). IOP has been shown to decrease with accommodation (Mauger et al., 1984; Read et al., 2010). This decrease has been measured at 2.38 ± 0.65 SD mmHg for 4 dioptre accommodation. Vieira et al. (2006) found an increase > 10 mmHg can occur from exercise. No studies have been found describing the compound effects of amultiple causes of increasing IOP. Logically, compound effects are possible. There is clearly significant variation in IOP[5].

[5]Intra-ocular pressure is always referred to in this study as a single value at any particular moment for a particular eye. This is obviously not the case. The human eye is approximately $22 - 24$ mm

1.1.3 Material Behaviour of the Eye

The shape of the eye relies on the equilibrium between its mechanical stiffness (resistance to deformation) and the forces acting upon it. The mechanical stiffness of the cornea depends on its geometry (thickness and topography) and material stiffness.

The multi-faceted behaviour of corneoscleral tissue can be described as incompressible (Humphrey, 2003; Kampmeier et al., 2000), hyperelastic (Woo et al., 1972), anisotropic (Elsheikh et al., 2008c; Elsheikh and Alhasso, 2009; Elsheikh et al., 2009; Pinsky et al., 2005; Roy and Dupps, 2009) and viscoelastic (Boyce et al., 2007; Downs et al., 2005; Elsheikh et al., 2008d)[6].

Collagen arrangement

Collagen has been assessed to be the governing load-carrying constituent of the cornea and sclera; this was evidenced by experimental studies including: Jue et al. (1991), Newton and Meek (1998), Boote et al. (2003) and Boote et al. (2009). As it is the collagen of the stroma which provides both hyperelastic and anisotropic behaviours, it is important to quantify significant collagen arrangement characteristics.

The collagen based mechanical response is related to the density, anisotropic arrangement and the size of collagen fibril bundles (referred to as collagen fibres). The collagen fibres in the cornea are of relatively consistent diameter of ≈ 30 nm where in the sclera they typically increase to a ranging diameter $35 - 145$ nm, as evidenced by (Borcherding et al., 1975) (see Figure 1.4). The quantity of collagen fibrils per unit area of stroma

high internally when the body is in the standing and supine positions respectively. This assumption is made for two reasons: (i) typical intra-ocular pressure is $13 - 20$ mmHg, while the deviation in pressure resulting from the gradient of hydrostatic pressure would relate to $\approx \pm 0.8$ mmHg and is therefore negligible, (ii) it is the objective of the research conducted for this thesis and in the field to affect diagnosis and treatment procedures for conditions of visual degeneration. It is therefore practical to adopt accepted convention in the fields of optometry and ophthalmology when it does not significantly compromise reported findings.

[6]Many other important studies have been conducted describing these properties, too numerous to list.

decreases from the cornea to the sclera; the quantity, not density, was also measured by (Borcherding et al., 1975) to be $100 - 1100 \times 10^8$ nm^2.

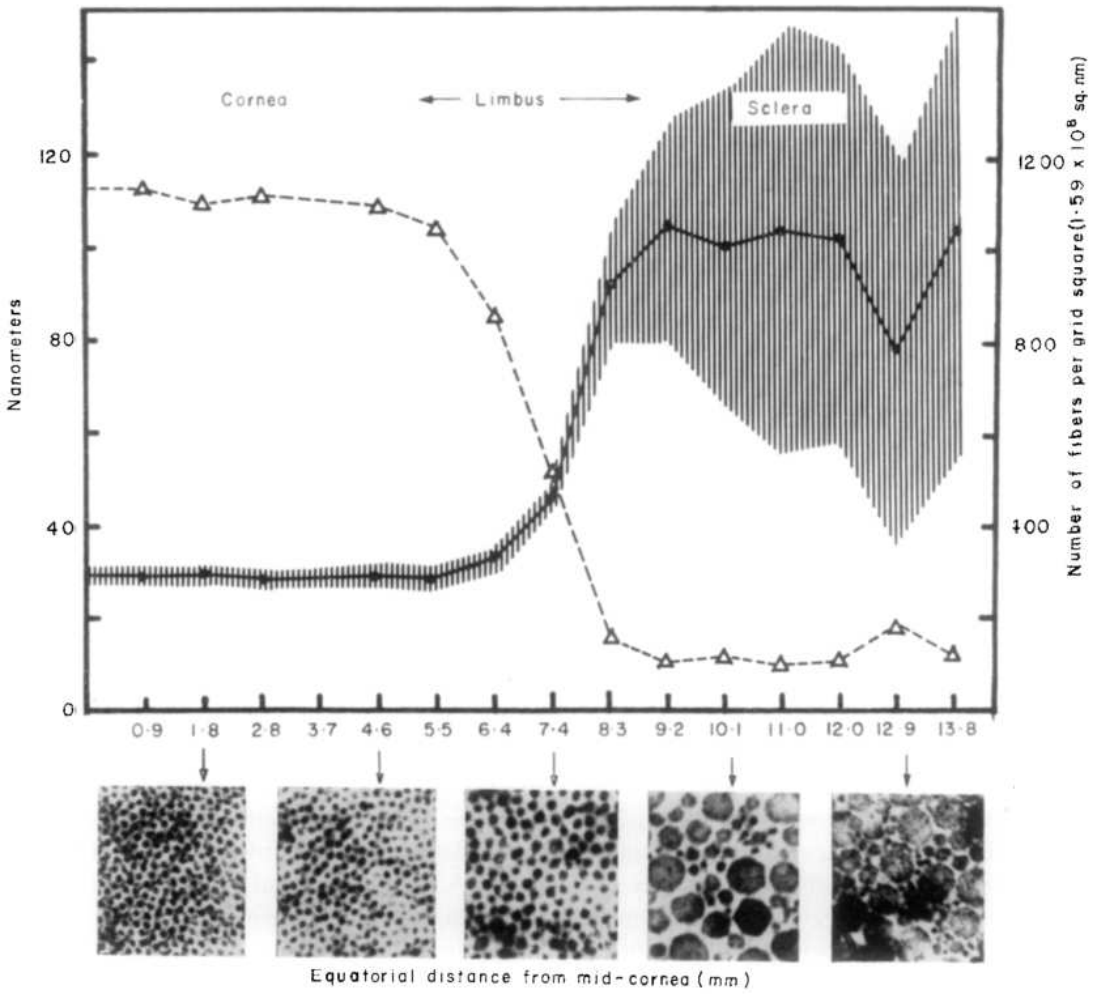

Figure 1.4: The average number of collagen fibril bundles (fibres) per unit area ($\triangle - \triangle$) with the mean diameter ($\bullet - \bullet$) $\pm$ SD (shaded area) as a function of distance from the mid-cornea. Arrows indicate the location of electron micrographs along the central vertical axis from mid-cornea to sclera (original magnification $\times$40000). Image from Borcherding et al. (1975).

Studies using wide angle X-ray scattering (WAXS) detailed the anisotropic arrangement of collagen fibrils in the human cornea and quantified typical characteristics including: (1) a preferred orthogonal orientation in the central cornea in temporal-nasal (T-N) and superior-inferior (S-I) directions; (2) circumferentially arranged fibrils in the limbus and corneal periphery; (3) a transition zone between (1) and (2); and (4) a

greater, total quantity of fibrils in the peripheral region compared to the central cornea (Aghamohammadzadeh et al., 2004; Meek and Boote, 2004; Boote et al., 2006), for example see Figure 1.5. Within these studies the discrete anisotropic distribution and regional variation of total fibril quantity was presented. These studies presented total relative quantities of fibrils at each measurement location.

The corneal stroma comprises over 200 lamellae (Freegard, 1997; Oyster, 1999) which are formed of a proteoglycan-rich matrix containing tightly packed and ordered collagen fibrils. Komai and Ushiki (1991) observed the 3D organisation of collagen fibrils in the human cornea using electron microscopy (see Figure 1.6). That study provided information relating to the arrangement of the lamellae and the fibrils connecting the lamellae providing interlamellar cohesion (ILC).

The collagen arrangement of the sclera is more complex and has not been studied as extensively as the cornea. However, WAXS has shown an increase in collagen quantity with a preferred circumferential arrangement around the optic nerve (Pijanka et al., 2012). A recent study presented at The Association for Research in Vision and Ophthalmology (Spang et al., 2015) mapped the collagen arrangement for the total corneoscleral envelope (see Figure 1.7)[7]. This study reinforced earlier studies highlighting the collagen fibril arrangement around the optic nerve. Between the limbus and the optic nerve region there is less obvious organisation to the collagen fibril arrangement. However, there are four areas in the anterior sclera, Figure 1.7(a), where uniaxial fibril arrangement was observed; corresponding to the locations where the four restus muscles were attached.

Relative regional stiffness of the corneoscleral stroma

The stiffness of the cornea varies across its regions in a relatively clearly definable pattern. A study by Hjortdal (1996) measured the secant elastic modulus between different

[7] *Study conducted adjacent to the primary research presented in this thesis in collaboration with the University of Cardiff:* Spang M., Sorensen T., **Whitford C.**, Elsheikh A. & Boote C., **Individual-specific microstructural characterisation of human ocular tunics for whole eye numerical modelling**, May 2015, The Association for Research in Vision and Ophthalmology

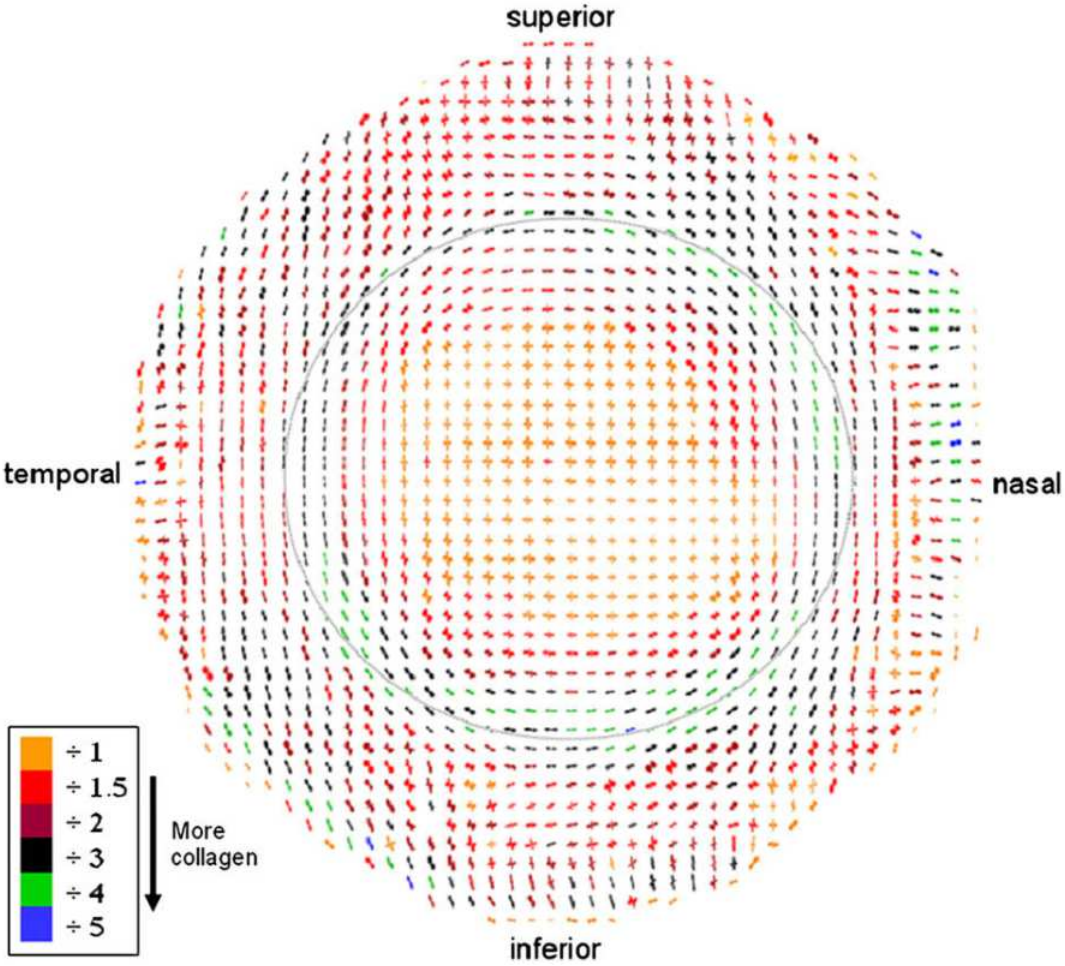

Figure 1.5: Preferential collagen fibril orientation across a right human cornea, limbus and adjacent sclera. There is clear, preferred orthogonal organisation in the central cornea gradually transitioning to circumferential alignment at the limbus. Measurements taken at 0.4 mm intervals. Image from Boote et al. (2006).

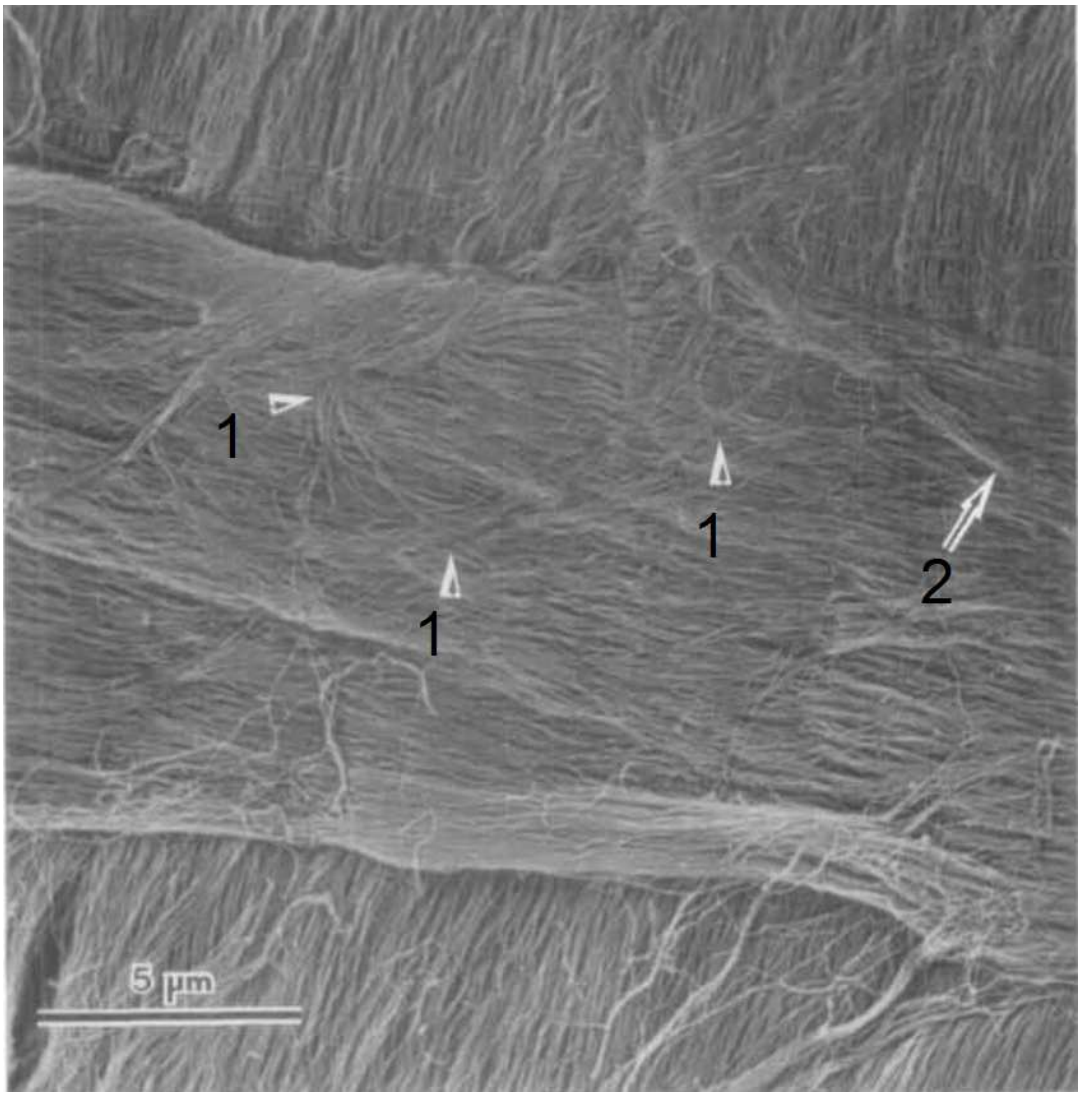

Figure 1.6: A ×6200 magnification of the collagen arrangement of the cornea. The small arrows (marked 1), point to examples of collagen fibrils. These fibrils form together in clear lamellae. This image shows two stacked lamellae running in perpendicular directions. The smaller bundle (marked 2) links between the two lamellae providing cohesion. Image from Komai and Ushiki (1991).

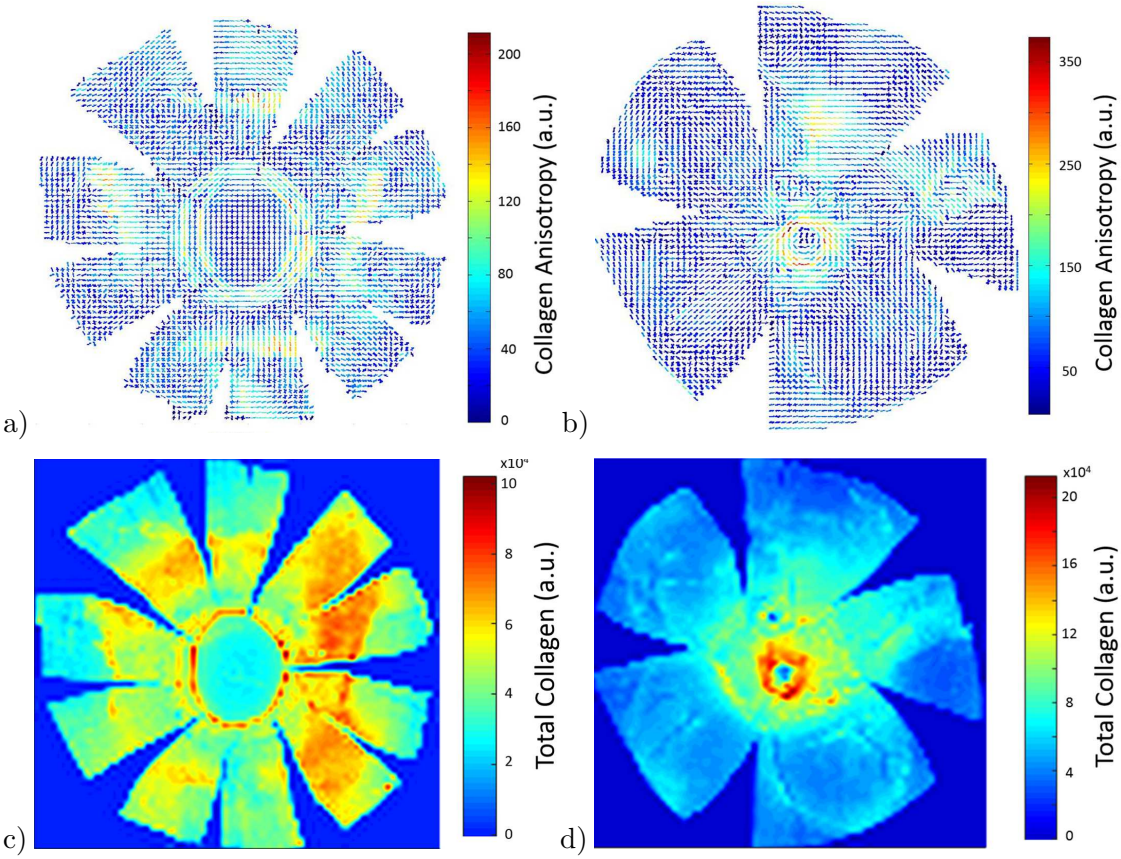

Figure 1.7: Human left eye after dissection into anterior and posterior cups. Corresponding montages of polar vector plots of anisotropic collagen for the anterior (a) and posterior (b) segments and the relative total collagen content for the anterior (c) and posterior (d). WAXS measurements were taken at 0.5 mm intervals. Figure reproduced from Spang et al. (2015).

intraocular pressure level at the central cornea, para-centre, the peripheral cornea and the limbus from 18 *ex vivo* eyes. They calculated that the meridian stiffness reduced from the central cornea and the para-centre (where the values were almost equal) to the periphery by $20-25\%$; while circumferential stiffness was calculated to reduce linearly from centre to periphery by a similar amount. Comparing the limbus to the central cornea, the circumferential stress almost doubled while the meridional stress reduced by $30-35\%$.

The stress-strain relationship of the sclera also varies with region. Elsheikh et al. (2010a) and Geraghty et al. (2012) tested strips from 3 locations of 36 and 45 donor sclera, respectively. Those studies were able to characterise both regional, and age-related stiffness relationships. The findings of these and an earlier study by Friberc and Lace (1988) showed that the sclera becomes more compliant in the posterior compared to the anterior region. Elsheikh et al. (2010a) expanded Friberc and Lace (1988) including a comparative assessment of the equatorial region where there was found to be no significant variation in stiffness with respect to the posterior region; shown by comparing stress levels under 0.01 strain, as seen in Figure 1.8. Regional variation in viscoelastic response across the sclera was shown to vary with stiffness.

Age-related properties mechanical properties of the stroma

It is known that there are changes to the collagen within the stroma as a result of the ageing process. Daxer et al. (1998) showed that the mean radii of collagen fibrils in the cornea changed with ageing. In two age-groups across 65 years of age, an increase from 15.4 to 16.1 μm was observed. These, and other changes to the collagen structure, are likely to change the mechanical behaviour of the stroma. Despite likely mechanical age-effects, there has been little research in this area; perhaps due to the difficulty in obtaining enough donor specimens. This is compounded by the inherent variation of behaviour due to natural variation between humans as a large number of specimens are therefore required to identify variation resulting from ageing.

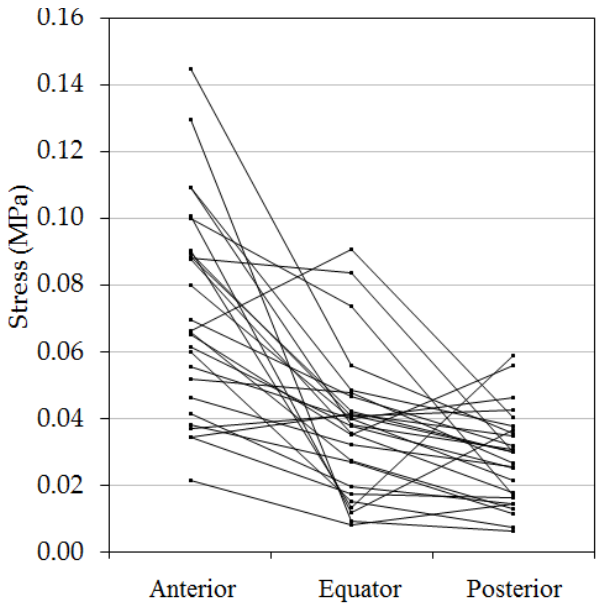

Figure 1.8: Stress values plotted for specimens extracted from the same sclera. All stress values were obtained at 0.01 strain from strip-extensometry conducted at a strain-rate of 8%/min. Figure reproduced from data (Geraghty, 2012).

The stiffness of the cornea and sclera increases with age; this has been consistently demonstrated by numerous studies including: Elsheikh et al. (2007a) and Elsheikh et al. (2010b) (cornea) and Avetisov et al. (1983), Friberc and Lace (1988) and Geraghty et al. (2012) (sclera). Elsheikh et al. (2010b) measured stress-strain behaviour from 57 corneal specimens by inflating separated corneas, the results of this study have been reproduced in Figure 1.9 and clearing shows increasing stiffness from $30-99$ years of age.

Elsheikh et al. (2008d) assessed viscoelastic properties of the cornea and how these varied with age from donors ranging $50-95$ years-of-age and found a decrease in all characteristics of viscoelasticisty (strain-rate effect, creep, stress-relaxation and hysteresis) with ageing.

Similarly, Geraghty et al. (2012) identified increasing stiffness in the sclera with age (Figures 1.10.**a**-**c**). A study utilising scleral inflation by Coudrillier et al. (2012) also

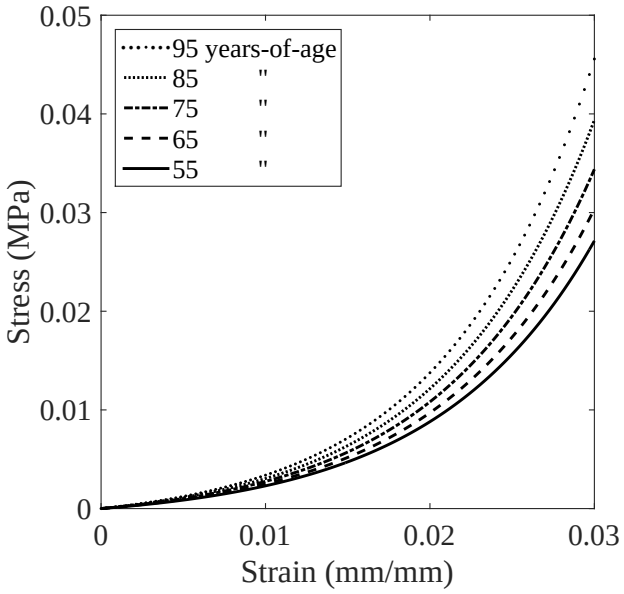

Figure 1.9: Stress-strain behaviour of human eye cornea derived from 57 specimens aged $50 - 99$. Plot reproduced from data (Elsheikh et al., 2010b).

demonstrated age-related stiffening across 33 donor specimens $40 - 80$ years-of-age.

1.1.4 Continuum Biomechanics

Nonlinear continuum mechanics, together with nonlinear constitutive modelling, are essential prerequisites for numerical analysis of biological tissues such as those of the ocular vessel.

Continuum biomechanics is the applied field of nonlinear continuum mechanics, which is a based in the generalised form of continuum mechanics theory. Continuum biomechanics emerged during the 1960s and since this time has contributed significantly to the improvement of healthcare. The development of this field, which has yet to reach its full potential, has followed the increasingly complex understanding of biological matter at the cellular and microstuctural levels and the increase in the computational power required to solve complex boundary- and initial-value problems.

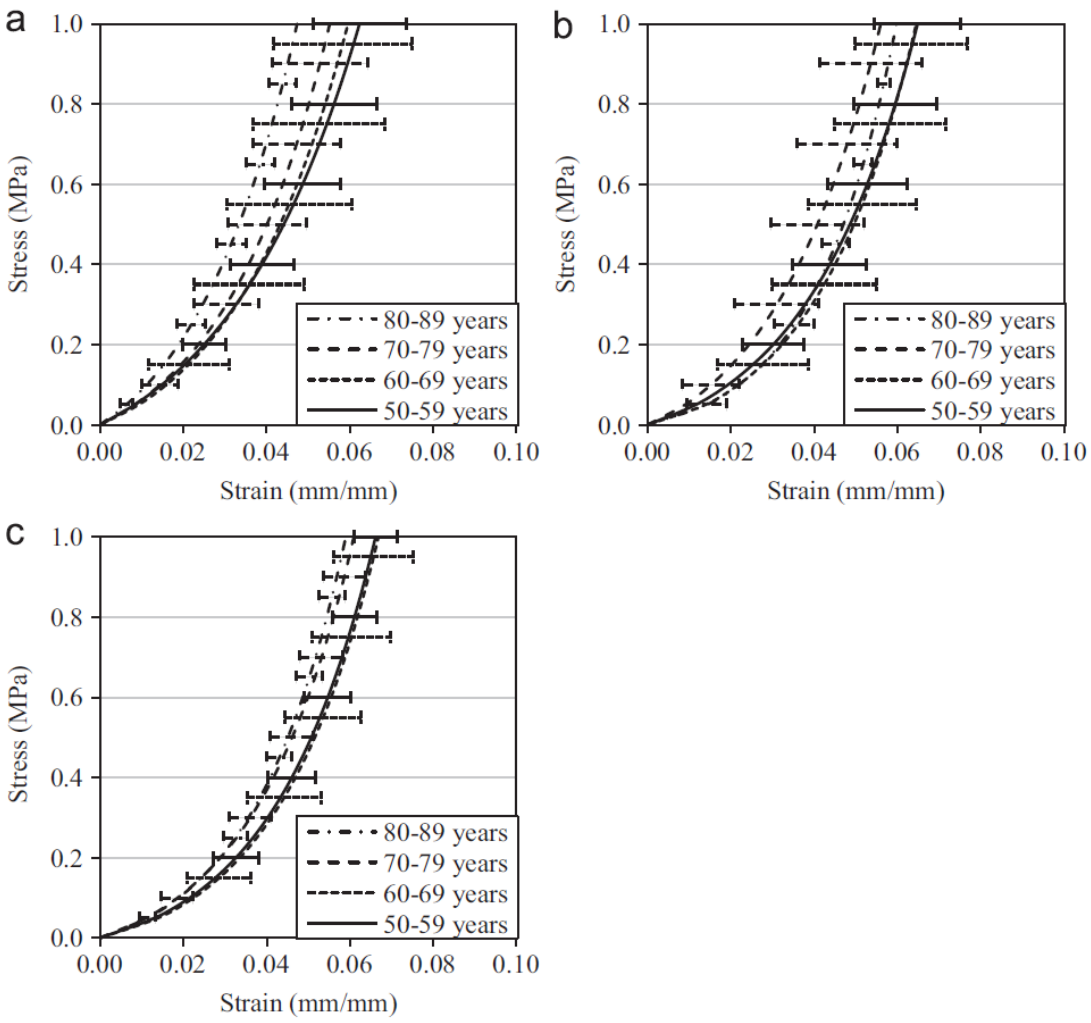

Figure 1.10: Comparison of average stress-strain behaviour within the four age groups for (a) anterior specimens, (b) equatorial specimens, and (c) posterior specimens. Experimental data obtained from uniaxially tested strips of sclera. Error bars depict the standard deviation of strain values. Plot reproduced from data (Geraghty et al., 2012).

When considering the role of continuum mechanics in general, and in relation to this present study it is import to consider that it is not the intent of continuum mechanics to fully describe a material. The purpose of the continuum mechanics frameworks and their application is to describe relevant characteristic behaviours within the boundaries of observation and interest. The following section seeks-only to contextualise continuum biomechanics within existing frameworks and these boundaries. There are a number of frameworks associated with continuum mechanics, of which the current study builds on finite elasticity and viscoelasticity.

Finite elasticity

Concerned with nonlinear elastic behaviour over finite strains Fung (1967); Tong and Fung (1976) explored the application of finite elasticity to soft tissue. Fung demonstrated that there was a near linear relationship between the uniaxial stiffness and stress, where uniaxial stiffness is given by $dP_{11}/d\lambda$, P_{11} is the first Piola-Kirchoff stress and λ is the stretch ratio. This led to the linear approximation $dP_{11}/d\lambda = \alpha + \beta P_{11}$ where α and β are material parameters. Integration of this relationship suggested an exponential stress-strain relationship. The advances in continuum biomechanics by Fung and his colleagues during this period resulted from possibly the most important hypothesis witnessed in this field in the last century: leading from the the uniaxial exponential function - Fung introduced the 3D pseudostrain energy function $W = c\left(\exp^{Q} - 1\right)$, where Q is a function of the Green strain tensor $\mathbf{E} = \frac{1}{2}\left(\mathbf{F}^T\mathbf{F} - \mathbf{I}\right)$, with $\mathbf{F}$ the deformation gradient tensor, $\mathbf{I}$ the unit tensor and c is a material parameter. Of particular importance in the above Green strain tensor equation is the product $\mathbf{F}^T\mathbf{F}$ which eliminates rigid body rotation, $\mathbf{R}$, from the problem[8]. Similar to the derivation of the uniaxial exponential relationship, this led to the relationship between the second Piola-Kirchoff stress tensor, $\mathbf{S}$, and the Green strain tensor,

$$\mathbf{S} = \frac{\partial W}{\partial \mathbf{E}} = c \exp^{Q} \frac{\partial Q}{\partial \mathbf{E}} \tag{1.1}$$

[8]The second order tensor $\mathbf{F}$ transforms as a vector and it follows that rigid-body translation is already eliminated

Based on these relationships, a number of descriptions for $Q(\mathbf{E})$ have been derived to fit to experimental data which included linear and nonlinear expressions.

Of course the field of finite elasticity is much broader than the above introduction and too broad to include here in its entirety. Details relating to the present study are described within Chapter 2; while Chapter 4 expands these frameworks presenting two new constitutive numerical models based in continuum mechanics theory. Further background on kinematics related to this topic can be found in a number of texts including Holzapfel (2000), Irgens (2008) and Epstein (2012).

Viscoelasticity

Development of viscoelastic theory is largely due to the development of polymeric materials (Christensen, 1982). However, in recent years advances focusing on the viscoelastic representation responses of soft tissue have been made.

Due to the large strains observed with soft tissue, early linear viscoelastic models are not applicable. Fung began to address this issue through the introduction of a quasi-linear viscoelastic theory. Describing 1D behaviour, Fung (1990) related the first Piola-Kirchoff stress and stretch in a time domain, t; with a relaxation period, τ:

$$P_{11}(t) = \int_{-\infty}^{t} G(t-\tau)\frac{\partial P_{11}^{e}}{\partial \lambda}\frac{\partial \lambda}{\partial \tau}\mathrm{d}\tau \tag{1.2}$$

where P_{11}^{e} is the nonlinear elastic response. This quasi-linear theory assumes the relaxation function is dependent on extension and time, where $G(t)$ is the reduced relaxation function (of time only) with $G(0) = 1$.

It has been shown more recently however, that to more accurately describe strain-rate and both long- and short-term viscoelastic responses nonlinear viscoelastic models are required. There have been a number of recent studies exploring such models in the context of soft biological tissues, for example Pioletti and Rakotomanana (2000)

and Holzapfel et al. (2000). Pioletti and Rakotomanana (2000) suggested a general viscoelastic description, describing the elastic, the short- and long-term memory contributions:

$$\mathbf{S} = \mathbf{S}_e\left(\mathbf{C}\left(t\right)\right) + \mathbf{S}_v\left(\dot{\mathbf{C}}\left(t\right);\mathbf{C}\left(t\right)\right) + \int_{\delta}^{\infty}\sum\left(\mathbf{G}\left(t-\tau\right),\tau;\mathbf{C}\left(t\right)\right)\mathrm{d}\tau \tag{1.3}$$

where $\mathbf{C}$ is the right Cauchy-Green strain tensor.

Despite recent advances in the viscoelastic representation of soft tissues, very little progress has been made in the development of models specifically appropriate for ocular tissue; this is exploded further in Chapter 4 where a new viscoelastic constitutive model of the stroma is presented.

Mechanobiology

It is appropriate to introduce a complementary and emerging field known as mechanobiology. A survey article by van der Meulen and Huiskes (2002) described these complementary fields with '...form follows function follows form...' where biomechanics focuses on understanding how function follows form and mechanobiology focuses on the understanding of form following function. Both of these fields are critical in the further understanding the function of soft tissue and the eye by experimental and numerical techniques. However, the current study focuses on the concept of function following form and therefore adopts the continuum biomechanics frameworks.

1.2 Aim and Objectives

Researchers are often motivated by previous achievements, current requirements and ambition. In ocular biomechanics the ultimate goal and motivation must remain clear: the improvement of healthcare; specifically in the diagnosis and treatment of visually degenerating conditions.

With this in mind, this present study aims to:

further understand the biomechanical properties of the ocular globe by *ex vivo* testing and multiscale numerical modelling.

To achieve this, the study will:

1. develop methodology and equipment capable of measuring deformation across the intact eye globe;
2. develop methods to generate specimen specific, and characteristic, geometries of the eye globe;
3. determine the regional variation of mechanical behaviour across the intact eye globe;
4. validate the experimental procedure based on pre-existing material representation methods;
5. develop a new constitutive model of the human cornea representing age-related stiffening, 3D anisotropy and inhomogeneity based on a large database of previous experimental data from separated cornea;
6. develop a second new constitutive model of the human cornea representing the viscoelastic response of the human cornea based on the smaller database of previous experimental data, also from separated corneal buttons.

1.3 Thesis Structure

This thesis is arranged as follows:

- Chapter 1 describes how the study of ocular science has progressed to the present day, current relevant knowledge of the anatomy and general behaviour of the eye

is provided and the background of continuum biomechanics is introduced;

- Chapter 2 examines current techniques used to experimentally study and model the ocular vessel with the aim to inform the methodology of the present study;
- Chapter 3 presents the experimental study of intact eye globe biomechanical properties, including the development of new methodology and analysis of results;
- Chapter 4 describes the numerical analysis developments which formed part of this present study, in particular two new constitutive material models are presented which describe the behavioural characteristics of the corneal stroma;
- Chapter 6 provides an overall discussion of the present study and its main conclusions, in addition to a number of recommendations for future work.

Chapter 2

Review of Current Experimental and Modelling Techniques

The following chapter examines techniques used to determine the material behaviour of ocular tissue including experimental analysis, mathematical and numerical data analysis. In addition, the development of constitutive material modelling associated with the current study is explored.

2.1 Experimental Techniques

Components of the following section have been published in a alternate forms in:

Whitford C. & Elsheikh A., **Corneal Biomechanics Testing Methods**, May 2014, Chinese Journal of Optometry and Ophthalmology Visual Science;

and

Whitford C., Joda A., Jones S., Bao F., Rama P. & Elsheikh A., **Ex-vivo Testing of Intact Eye Globes Under Inflation Conditions to Determine Regional Variation of Mechanical Stiffness**, July 2016, Eye and Vision.

This section concentrates on experimental techniques used to determine hyperelasticity, anisotropy, viscoelasticity (hysteresis, strain-rate dependency, creep and stress-relaxation), age-related stiffening and the changes in these biomechanical properties associated with the treatment of degenerative conditions. A discussion of the main techniques is presented to illustrate how they compare in simplicity, accuracy and reliability. The techniques include strip-extensometry, corneal button inflation, scleral cup inflation, whole eye globe inflation and *in vivo* analysis. Literature illustrates that these techniques have typically been tested extensively on non-human eyes. This is probably due to the difficulty obtaining specimens which are typically for human transplantation. Many of the studies discussed in this section pertain to the experimental techniques themselves and not the specific results and therefore cover human and non-human testing. However, the importance of obtaining credible data from priceless human specimens is the focus of the application of these procedures in the context of this current study.

2.1.1 Strip-extensometry

Strip-extensometry testing involves extracting a strip of tissue with a constant width and subjecting it to uniaxial tension while monitoring its behaviour. The stresses and strains are calculated from the load and the elongation data using simple calculations relating to the reference configuration (for more information see Section 2.2). This common form of deriving stress-strain relationships leads to the mechanical relationship more accurately known as the engineering stress-strain relationship (for further information on this analysis see Section 2.2).

The simplicity of this technique makes it quite common in ocular biomechanics research. However, there are a number of inherent deficiencies, which can reduce its reliability, and must be considered and accounted for. The deficiencies mainly originate from the non-physiological loading, initial curve form of the specimen, the non-uniform specimen

thickness, the termination of the collagen fibrils at the edges of the specimen that are not aligned with the specimen's orientation, and the relatively large thickness of the specimen. The latter leads to unequal clamping of the internal and external layers of the tissue.

The straightening of the specimen from its curved form results in initial stresses that affect the behaviour under subsequent loading (Greene, 1985).

2.1.2 Corneal Inflation Tests

Corneal inflation tests were developed to avoid the problems associated with strip-extensometry and enable testing of cornea in nearer to physiologic conditions, for example Boyce et al. (2008), Bryant and McDonnell (1996), Elsheikh et al. (2010b) and Metzler et al. (2014). In this method an intact cornea, along with a ring of scleral tissue, is supported along the limbus and subject to a hydrostatic, uniform, internal pressure (simulating intra-ocular pressure). This pressure acts on the posterior surface of the cornea while deformation is monitored using non-contact methods.

Due to the clamping conditions, typically at, or adjacent to, the limbus, the strain patterns in this area are not representative of *in vivo* conditions.

2.1.3 Sclera Inflation Tests

Sclera inflation provides the same benefits as corneal inflation techniques and is also subject to the same limitations. In addition to providing nearer physiological conditions with which to analysis the scleral stroma, this technique provides the opportunity to assess the behaviour in the fascinate of the optic nerve (Coudrillier et al., 2012; Girard et al., 2008, 2009a). Examination of this area is not possible by strip-extensometry. A number of other studies have been conducted using this technique including: Boschetti et al. (2012), Boyce et al. (2008), Coudrillier et al. (2012) and Myers et al. (2010).

2.1.4 Whole Eye Globe Inflation Tests

Despite the advantages of corneal and sclera inflation over strip-extensometry there are still major shortfalls in its ability to provide physiologic loading conditions. This is due to the clamped boundary, usually at or near the limbus. This excludes deformation effects in these areas and induces stress distributions which do not represent physiologic conditions. For this reason inflation tests involving intact eye globes were developed, for example Jaycock et al. (2005), Kling et al. (2010), Lari et al. (2012), Mattson et al. (2010) and Wong et al. (2012). However, while being more accurate and reliable, globe testing introduces new major challenges in the test regime of ocular tissue. There are significant difficulties in obtaining intact human donor eye globes for research compared to separated cornea or sclera. This is often due to the protocol for human tissue donation which first considers whether cornea are suitable for transplantation; during this analysis it is typical to remove the cornea from the sclera. In addition, the tests involve removing the vitreous, supporting the eye (without introducing non-physiologic boundary conditions), applying intra-ocular pressure changes, capturing surface deformations and post-processing the experimental data to obtain meaningful stress-strain relationships.

Once these challenges are addressed, globe testing offers additional benefits compared to separated corneal, or scleral, inflation in addition to the more reliable results expected. With globe testing it becomes possible to also determine the material properties of the sclera and cornea as they act together to resist intra-ocular pressure.

2.1.5 *In Vivo* Test Methods

It is obvious that the ability to measure biomechanical properties *in vivo* provides the only true measure of *in vivo* behaviour and has numerous applications in ophthalmology. Currently there is no definitive technique or device that can acheive this outcome. However, there have been studies which have assessed the feasibility. Brubaker et al.

(1975) presented a method to measure the *in vivo* biomechanics which was later applied to in Rhesus monkeys Brubaker et al. (1977). This method could not be applied to humans as it required an acrylic contact lens to be glued to the cornea. In addition, the technique required intra-ocular pressure to be controlled by a hypodermic needle inserted into the eye globe. Elsheikh et al. (2015)[1] measured the variation of stiffness across the human cornea with an *in vivo* study. Due to approximations that were required for that study, such as corneal thickness and intra-ocular pressure, material stiffness values had to be presented in relative terms across the corneal surface. The study provided valuable information on corneal stiffness whilst also progressing *in vivo* testing methods. However, it was not able to provide accurate stress-strain relationships, and cannot therefore replace *ex vivo* testing of corneas.

There are a number of studies which discuss the evaluation of biomechanical properties obtained from the Ocular Response Analyzer or OCULUS Corvis® ST. These include *ex vivo* (Bao et al., 2015)[2] and *in vivo* (McMonnies, 2012; Pepose et al., 2007; Qazi et al., 2009) studies. Currently these techniques cannot provide stress-strain relationships; instead they provide an indicator to mechanical properties in the form of metrics such as corneal hysteresis (CH) and corneal resistance factor (CRF). They also included the applanation times (A1T, A2T), lengths (A1L, A2L) and velocities (A1V, A2V), in addition to the highest concavity time (HCT), peak distance (PD), radius (HR) and deformation amplitude (DA), obtained by the Corvis® ST. While these metrics are extremely useful indicators to relative behaviour, they do not provide stress-strain behaviour and are therefore not currently suitable to provide properties that can be utilised for numerical simulations.

[1] *Study conducted adjacent to the primary research presented in this thesis in collaboration with The University of New South Wales:* Elsheikh A., McMonnies C., **Whitford C.**, & Boneham G. C., **In vivo study of corneal responses to increased intraocular pressure loading**, December 2015, Eye and Vision

[2] *Study conducted adjacent to the primary research presented in this thesis in collaboration with WenZhou Medical University:* Bao F., Deng M., Wang Q., Huang J., Yang J., **Whitford C.**, Geraghty B., Yu A. & Elsheikh A., **Evaluation of the relationship of corneal biomechanical metrics with physical intraocular pressure and central corneal thickness in ex vivo rabbit eye globes**, August 2015, Experimental Eye Research

2.1.6 Discussion of Methods

Despite the shortfalls in the strip-extensometry technique, several previous tests have been conducted on *ex vivo* ocular tissues which describe the mechanical behaviour in detail (Boschetti et al., 2012; Downs et al., 2003, 2005; Elsheikh et al., 2010a; Jayasuriya et al., 2003; Govrin-Yehudain et al., 1986; Girton et al., 2002; Hoeltzel et al., 1992). While these, and similar studies, may not provide exacting data pertaining to physiologic responses, they have provided extremely valuable information particularly regarding directional, location and age-related variation in mechanical behaviour. Jayasuriya et al. (2003) assessed relative stiffness in relation to anisotropy and effects of hydration. Hoeltzel et al. (1992) compared mechanical properties across species. This technique has been used to great effect to test numerous specimens allowing for the determination of characteristic trends; which requires the assessment of large numbers of specimens due to natural human variation, for example Coudrillier et al. (2012) and Geraghty et al. (2012) (results of these studies were presented in Chapter 1).

To quantify the affect on derived measurements of material behaviour Elsheikh and Anderson (2005) compared the results of separated cornea inflation and strip-extensometry tension tests reporting that strip-extensometry tests exhibited a 32% increase in stiffness. This increased stiffness was attributed in part to the initial curvature of the strip and variations in thickness and length. However, there is also an increased degree of surgical manipulation and change in the anisotropic strain distribution, compared to the *in vivo* conditions, that cannot be disregarded. A study by Lari et al. (2012) compared strip-extensometry and whole eye globe inflation tests; they found increased reliability of the globe test results and reported different stiffness-strain relationships between the test methods. However, that study was limited to observations of posterior sclera behaviour; while other studies on intact eye globes were limited to observations on the anterior eye (Jaycock et al., 2005; Kling et al., 2010). Mattson et al. (2010) performed experiments on intact rabbit eyes reporting deformation on a single horizontal plane. They demonstrated the benefit of studying intact eye globes, highlighting the

consistency with *in vivo* geometry and load distributions.

In addition, collagen is known to remodel its microstructural arrangement in line with strain distribution and preconditioning in ligaments (Quinn and Winkelstein, 2011). A recent, ongoing, study[3] (Bell et al., 2016) began to quantify the changes in collagen orientation in the cornea. Wide-angle X-ray scattering images were taken following uniaxial static strains of 1.4%, 2.8%, 5% and 8% on excised cornea strips. The direction of preferential fibrillar orientation shifted from naso-temporal to superior-inferior following the 1.4% uniaxial strain application and the degree of anisotropy increased with strain. The largest change was observed between 2.8% and 5% uniaxial strain increments, after which the total collagen aligned in the superior-inferior direction was $24 \pm 10\%$ greater than in other directions and the ratio of collagen aligned in the superior-inferior direction to that in the naso-temporal direction changed from 0.86 ± 0.04 at rest to 1.90 ± 0.40.

These alterations in the mircostructure through non-physiological strain suggest that derived stress-strain relationships from tests which do not replicate *in vivo* loading conditions are not fully representative. Given that collagen is the primary contributor to stiffness in the ocular vessel (see Chapter 1), remodelling in-line with non-physiological strain would result in proportional changes in stiffness.

One of the most important aspects of strip-extensometry and, to a lesser extent, inflation of separated corneas or scleras, is the requirement for pre-conditioning. This is a much discussed and perhaps less understood necessity, as highlighted by Cheng et al. (2009). Based on this understanding it was hypothesised that if physiological loading is achieved, preconditioning will no longer be required.

Currently, derivation of accurate stress-strain relationships from *in vivo* tests has not been achieved. However, due to the progression of the science, it is feasible that true mechanical measurement of the *in vivo* human cornea will be achieved within the next

[3] *Study conducted adjacent to the primary research presented in this thesis in collaboration with Cardiff University:* Bell J., Hayes S., **Whitford C.**, Elsheikh A., & Meek K., **Hierarchical changes in corneal collagen structure under load**, May 2016, ARVO

decade; it is less foreseeable that *in vivo* techniques will be capable of measuring the properties of the sclera due to its location. For this reason, *ex vivo* techniques will continue to provide valuable advances in visual science. Furthermore, the application of strip-extensometry and separated corneoscleral still provide important tools in ocular biomechanics despite recent advances in intact eye globe testing.

2.2 Mathematical Analysis

From the simplest engineering stress-strain analysis of strip-extensometry, to advanced inverse analysis using novel and bespoke constitutive numerical models, experimental data requires analysis to provide the mechanical properties which describe the material response of the ocular stroma. The following sections describe the most relevant of these techniques with respect to the current study.

Mathematical analysis provides simple methods by which to derive stress-strain relations from experimentally obtained load-deformation relationships. These methods typically consider initial geometry. In analysis of strip-extensometry data, the stress (σ) and strain (ϵ) can be calculated by:

$$\sigma = \frac{P}{A_0} \; and \; \epsilon = \frac{\delta}{L_0} \tag{2.1}$$

where A, L and P represent the cross-sectional area, length and load respectively, the subscript 0 denotes the initial (reference) geometry and δ is the deformation.

As previously described, there are deficiencies in strip-extensometry including the initial curvature of the specimen. This particular deficiency is considered by a mathematical technique which has been developed to account for the initial specimen curvature. This leads to a value of strain which varies with distance, z, from the centreline of the specimen and distance, h, from the specimens mid-thickness surface (Elsheikh and

Anderson, 2005):

$$\epsilon = \frac{\delta}{2\alpha\sqrt{R_m^2 - z^2}} + \frac{h}{R_m} \tag{2.2}$$

where 2α is the angle of curvature of the specimen in radians (assuming spherical curvature) and R_m is the assumed spherical corneal median surface and considers the reference configuration. From this mathematical formulation, an equation relating the applied force, P, and the resulting strain:

$$P = \int_{-t/2}^{+t/2} \int_{-w/2}^{+w/2} \left(a\epsilon^3 + b\epsilon^2 + c\epsilon\right) \mathrm{d}z \cdot \mathrm{d}h \tag{2.3}$$

where a, b and c are constants to be determined such that the best fit with experimental data is achieved. The corresponding stress is calculated as:

$$\sigma = a\epsilon^3 + b\epsilon^2 + c\epsilon \tag{2.4}$$

The effect of thickness variation from a minimum at the centre, t_1, to a maximum at the clamps, t_2, can be considered next in the stress calculations to develop a modified stress, σ', in the form (Elsheikh and Anderson, 2005):

$$\sigma' = \sigma \cdot \frac{t_1}{(t_2 - t_1)} \left[\ln\left(\frac{t_2 L_0}{2}\right) - \ln\left(\frac{t_1 L_0}{2}\right)\right] \tag{2.5}$$

The assumption of linear variation between t_1 and t_2 is adopted to simplify the development of this form.

These formulations were able to address some of the earlier deficiencies in standard engineering stress-strain calculations regarding strip-extensometry. Other deficiencies such as: non-uniform thickness; variation of material properties; practical issues regarding the clamping of the specimen; the termination of the collagen fibrils along the sides of the specimen; and possible rearrangement of collagen fibrils cannot currently be addressed with this, or similar, mathematical techniques.

Mathematical techniques have successfully been adopted to analyse corneal inflation

tests. *Shell theory* has been the dominant method of numerical analysis applied to the cornea, Anderson et al. (2004), Elsheikh et al. (2007b), Howland et al. (1992), Li and Tighe (2007), Moiseeva and Stein (2013), Orssengo and Pye (1999) among many others. These methods make a number of substantial approximations that include a cornea's spherical topography and homogeneous properties. Typically uniform thickness is assumed, however Li and Tighe (2007) developed a technique to vary thickness along the meridian. These assumptions are necessary to enable a simple analysis of the results based on the closed-form equations (see Anderson et al. (2004) for more details, starting with an estimate of secant modulus, E, for a particular pressure-apical rise $(p - \delta)$ behaviour point:

$$E = \frac{pR_m^2}{2\delta t}(1 - v)\left[1 - \exp^{-\beta\eta}\cos(\beta\eta)\right] \tag{2.6}$$

where R_m is the radius of the corneal median surface, t the average thickness, η half the central angle of curvature $\left(\eta = \sin^{-1}(R_i/R_{ant})\right)$, R_i radius of the corneo-scleral intersection, R_{ant} radius of the cornea's anterior surface, $\beta = \sqrt{R/t} \cdot \sqrt[4]{3(1 - v^2)}$, and v Poisson's ratio taken as 0.49, assuming corneal tissue behaves as an almost incompressible material. The strain at this point is defined as:

$$\epsilon = \frac{pR_m}{2Et}(1 - bv)\left[1 + v\exp^{-\beta\eta}\cos(\beta\eta)\right] \tag{2.7}$$

and the stress is:

$$\sigma = \epsilon E \tag{2.8}$$

While shell analysis is simple enough to program in a spreadsheet, the associated approximations have reduced the reliability of the resulting stress-strain behaviour predictions and made it difficult to use them in the increasingly sophisticated, numerical simulations of the corneal biomechanical performance. This made it necessary to develop another method based on the use of inverse analysis, which sacrifices simplicity for the sake of much improved accuracy and reliability.

Mathematical methods often provide stress-strain relationships which are relative to

the initial geometry, Equation 4.11. It is typical to utilise material properties in finite-element analysis for various purposes, such as trialling surgical procedures. Finite-element analysis utilises stress-strain in terms of the current configuration, not the reference configuration. For non-linear materials in particular there can be significant differences between properties described in reference and current configurations and the utilisation of one in the other setting introduces errors in such instances.

Coudrillier et al. (2012) utilised multi-point measurements of the posterior sclera to measure regional strain under inflation. This modified form of shell analysis was able to obtain regional variations in stiffness. Despite its increased sophistication it was also limited to approximations of spherical topography and uniform thickness.

2.3 Numerical Analysis

Numerical analysis is performed using a number of different methods including: finite-difference method; finite-element method; computational fluid dynamics and many others. The numerical analysis discussed in this study is contained within the field of finite-element method. This method was originally introduced in 1956. In 1972 Ogden (1972) introduced a form of non-linear finite-element method suitable for soft-tissue.

Finite-element method is a numerical technique which enables simulations of complex boundary- and initial-value problems within a continuum framework. Calculation of stresses and strains in a structure can be performed by discretizing the large problem in to smaller elements through a procedure called *meshing*. Analysis which encompasses finite-element method within the assessment of a real-world problem is often referred to as finite-element analysis.

The application of finite-element analysis requires the definition of boundary- and initial-conditions, geometry and material response in the form of numerical relationships

between deformation, stress and stiffness. Boundary- and initial-conditions include: internal and external forces and rules governing translation and rotation.

Finite-element analysis is well established and therefore requires no justification in itself. Its application in the field of ocular biomechanics is less-well established, however, perhaps due to increasing computational power and the requirement for more complex representation of the ocular response, this technique has become the dominant method of analysis in recent years. This is evidenced by a large collection of published studies too numerous to list. Within these studies the application of this method has been demonstrated through its application to provide improved ocular healthcare solutions. Elsheikh et al. (2006, 2011a) and Khan (2014) provided correction equations obtained through finite-element analysis which improved the reliability of Goldman-applination tonometry. Sánchez et al. (2014), Pandolfi et al. (2008), Dupps and Wilson (2006) applied these techniques to greater understand the mechanical processes associated with photorefractive keratecomy. Similarly, Roy and Dupps (2009, 2011) investigated the relationship between corneal stiffness and LASIK. Within these, and many other studies, there are implementation variations such as software, mesh density, material representation, loading, geometry and boundary conditions. However, the methods adopted in those studies contain many similarities.

2.4 Numerical Representation of Material Behaviour

Single-faceted hyperelastic models that are strain-rate independent have been developed by Fung (1967); Mooney (1940); Ogden (1972); Rivlin (1997) and others, while viscoelastic models (Kobayashi et al., 1973; Holzapfel et al., 2002) describe the strain rate-dependency of material stiffness. These, and other similar models were used to describe the mechanical response of stromal tissue for human and non-human eyes. However, the microstructure of the stroma is extremely sophisticated which leads to a level of complexity in the mechanical response which requires models not found in existing literature.

The representation of the anisotropic behaviour of corneal stroma in numerical modelling has advanced greatly in the last two decades through studies by Alastrue et al. (2006), Pandolfi and Manganiello (2006), Pandolfi and Holzapfel (2008), Pinsky et al. (2005), Petsche and Pinsky (2013), Studer et al. (2010), Grytz and Meschke (2009), Grytz and Meschke (2010), Nguyen and Boyce (2011) and others. These studies partially represented the non-uniform distribution of collagen fibrils, as obtained using WAXS, with anisotropic distributions of material stiffness. Most importantly, Pinsky et al. (2005) introduced an angular integration method to represent the anisotropic distribution of stromal fibrils within a continuum framework; Pandolfi and Manganiello (2006) introduced a new constitutive model representing the matrix and collagen fibrils along with material stiffness parameters based on experimental corneal inflation and uniaxial data. These models often incorporated numerical laws derived by others, such as those by Holzapfel and Gasser (2001), Gasser et al. (2006) and Markert et al. (2005), to describe the constitutive behaviour of corneal stroma. Another example of a constitutive model by Studer et al. (2010) combined two numerical laws; the neo-Hookean material model to describe dilation and distortion of the matrix; and the polynomial Ogden law (for example, Ogden (1984)), modified by Markert et al. (2005), to describe the behaviour of, both the lamellae and the ILC, collagen fibrils. Despite these, and other advances in numerical representation of corneal stroma, only one previous study by Petsche and Pinsky (2013) presented a model with parameters describing out-of-tangential stiffness, whose values were derived from experimental analysis which was able to isolate out-of-tangential behaviour[4]. That study relied on the results obtained from four corneas tested under torsional shear. The specific quantification and modelling representation of shear stiffness in that study was limited to 0.01 strain.

Dynamic (non-static) behaviour of the cornea was modelled in various studies. Glass et al. (2008) developed an isotropic, homogeneous, analytical model describing the effect of viscosity and elasticity on hysteresis in the human cornea. Perez et al. (2013) devel-

[4]A second study has been published which includes specific out-of-tangential stiffness representation and forms a latter part of this thesis (Whitford et al., 2015)

oped a viscoelastic model of the eye, however this model was limited to linear-elastic, isotropic representation of porcine eyes with homogeneous corneal representation. Kling et al. (2014) considered an isotropic, linear viscoelastic corneal model in context in a multi-physics model considering air-puff tonometry. Su et al. (2015) Cui et al. (2015). Boyce et al. (2007) and Nguyen et al. (2008) developed viscoelastic constitutive models which where used to describe the behaviour of bovine cornea, however those studies where limited to representation of strip-extensiometry.

To the author's knowledge there are no studies which have combined either the complex anisotropic representation, shear stiffness and regional variation of density of the human cornea with its known, and significant, viscoelastic behaviour.

Chapter 3

Experimental Study

3.1 Introduction

The following chapter has been accepted for publication in a shorter form:
Whitford C., Joda A., Jones S., Bao F., Elsheikh A.. ***Ex Vivo* Testing of Intact Eye Globes Under Inflation Conditions to Determine Regional Variation of Mechanical Stiffness**, 2016, Eye and Vision.

Several biomechanical studies have been conducted on *ex vivo* ocular tissues employing mainly uniaxial tension tests (Curtin, 1969; Downs et al., 2003; Elsheikh et al., 2008c, 2010a, 2011b; Hoeltzel et al., 1992; Montiani-Ferreira et al., 2003) and inflation tests on separated corneas (Boyce et al., 2008; Bryant and McDonnell, 1996; Elsheikh et al., 2007a, 2008b) and part scleras (Coudrillier et al., 2012; Girard et al., 2009b; Myers et al., 2010). Comparative studies of the mechanical stiffness (as measured by the tangent modulus) obtained from uniaxial and inflation tests observed a significant increase in values obtained from the former tests (Elsheikh and Anderson, 2005; Lari et al., 2012). The higher stiffness estimation was attributed in part to the non-physiologic loading conditions and the higher strain rates commonly employed in uniaxial tension tests (Elsheikh and Anderson, 2005). Further, inflation tests of separated corneas or part

scleras have a number of drawbacks, namely that (1) the behaviour trends obtained for the corneas and scleras cannot be correlated since the specimens rarely come from the same donor, (2) the anterior sclera is not characterised since it is usually the clamp site for both cornea and sclera specimens, and (3) providing the cornea and sclera specimens with rigid edges during the test creates edge conditions and local stress distributions that are not physiological. These test techniques are explored further in Chapter 2.

In this study, a case is made for applying the inflation concept on intact eye globes to avoid the shortfalls of both the uniaxial testing of tissue strips and the inflation testing of corneal buttons or scleral cups. While globe inflation testing has been attempted before, the studies were limited to observations of parts of the eye globe; such as posterior sclera (Lari et al., 2012), anterior segment (Jaycock et al., 2005; Kling et al., 2010) or around a single horizon (Mattson et al., 2010). Further, earlier studies have employed boundary conditions that were dissimilar to *in vivo* conditions and may therefore have affected the globes response to internal pressure loading.

The present study extends behaviour observations to the whole ocular surface, attempts to use more physiologic boundary conditions and illustrates the new method through an initial experimental test programme involving cyclic inflation of intact eye globes. Attention has been given, as much as possible, to ensure consistency with the *in vivo* conditions of the eye in order to avoid the main sources of error affecting the reliability of the target material properties of the ocular tissue.

In addition to the experimental testing method, the procedure includes a numerical inverse analysis method that uses the experimental pressure-deformation data to determine the tissues hyperelastic stress-strain properties across the ocular surface.

3.2 Methodology

3.2.1 Challenges

There were a number of challenges which needed to be overcome to achieve successful results, the most significant of which were:

1. providing a support condition which minimised free-body motion, while allowing full-field observation of deformation;
2. providing a visual texture to the surface of the eye globe with the appropriate resolution and contrast suitable for digital image correlation, which was stable on the surface of the tissue during the introduction of the support media in its liquid state (see Sections 3.2.4 and 3.2.6 for more details), while not affecting the mechanical properties under investigation;
3. removal of the innermost contents of the eye globe;
4. applying above physiological intra-ocular pressure without forcing fluid to pass through the trabecular meshwork, which would expel the applied media designed to obtain deformation measurements through digital image correlation;
5. maintaining hydration of the stroma without inducing swelling, and;
6. measuring the intra-ocular pressure.

3.2.2 Physical arrangement

Instrumentation has been developed to support, protect and monitor the intact eye globe while allowing simple computer control of test procedure and data collection. A diagram of the test rig is provided in Figure 3.1. A fixed borosilicate glass box contains the intact globe and enables its suspension in a clear gelatin material that (1) protects the external surface of the ocular vessel from environmental conditions, (2) provides the

eye with a support system, which restricts free-body motion, is more uniform and offers better representation of physiologic conditions than traditional support systems, and (3) enables an unobstructed view of the entire ocular surface from outside the glass box.

A 2 × 50 mm hypodermic needle was inserted into the ocular cavity through the posterior pole, passed through the back wall of the glass box and its support system and connected through a pipe network to a motor-driven syringe pump, which provided changes in the applied pressure. Fixed at the same elevation as the centre of the eye is a pressure transducer (FDW 060-K262-01, RDP Electronics, USA) that measured the applied pressure with a 0.1 mmHg resolution.

The deformation of the eye that resulted from changing the internal pressure by the syringe pump was measured using a system of three high-resolution digital cameras (550D, Canon, Japan), with 100 mm (fixed-focal-length) macro lenses that were mounted on a support frame designed for both access and rigidity. The cameras were positioned around the equator of the eye globe facing perpendicular to the sides of the triangular support box. The camera images were initially used to obtain sufficient topography information to construct the eye-specific FE numerical model of the test specimen used in later inverse analysis. The cameras (Figure 3.1) were further used during the test to obtain images of the deformed shape of the eye, which were then analysed using digital image correlation (DIC) software (Istra4D, Dantec Dynamics A/S, Denmark) to quantify the displacement distribution across the surface of the eye.

In addition, a laser displacement sensor (LK-2001, Keyence, UK) measured the displacement at the corneas apex with 1 μm resolution. This addition to the test rig helped (1) enable the conduct of the test while controlling the displacement at the apex, and (2) provided a direct measurement of an important displacement parameter that aided the validation of the deformation measurements obtained from analysis of the camera images.

The control of the stepper-motor was the most critical component in the functionality of the set-up. The rig was designed in such a way that the pump providing either an increase or decrease in pressure had the smallest cross-sectional area possible. This was designed to induce to the smallest change of pressure possible from a corresponding linear actuation of the pump. This provided the greatest stability in the system and also reduced the effect of backlash to within the capacity of the software control system (further details describing the software are in Section 3.2.3). A stepper-motor was chosen to control the actuation of the syringe due to its high resolution and ability to operate at both low and high speeds efficiently. One potential disadvantage of stepper-motors is their low torque. However, this was not an issue in this situation due to the very low resistance of the syringe pump.

3.2.3 Control

A LabVIEW program has been developed to record data and control the test using a closed-loop system through a data acquisition card (DAQpad 6015, National Instruments, USA). The control and data acquisition system is shown schematically in Figure 3.2. The system enables the conduct of the test through either control of applied pressure (p) or resulting displacement (δ) at the corneal apex using a non-linear, proportional-gain, control of the motorised syringe pump. Trials have been conducted to ensure the system provides stable rates of change in pressure $\left(\frac{dp}{dt}\right)$ or displacement $\left(\frac{d\delta}{dt}\right)$. During the test, applied pressure and displacement at the corneal apex were recorded every 50 ms, and filtered through a 4 Hz low-pass filter, which was assessed to be a suitable sampling rate at the calibration trials. Further, the LabVIEW software triggered all cameras simultaneously at specified times during the test, and the images were collected and used later in the construction of specimen-specific eye models and determining the distribution of deformation across the ocular surface.

LabVIEW is a graphical language, significantly different to the other, syntax based,

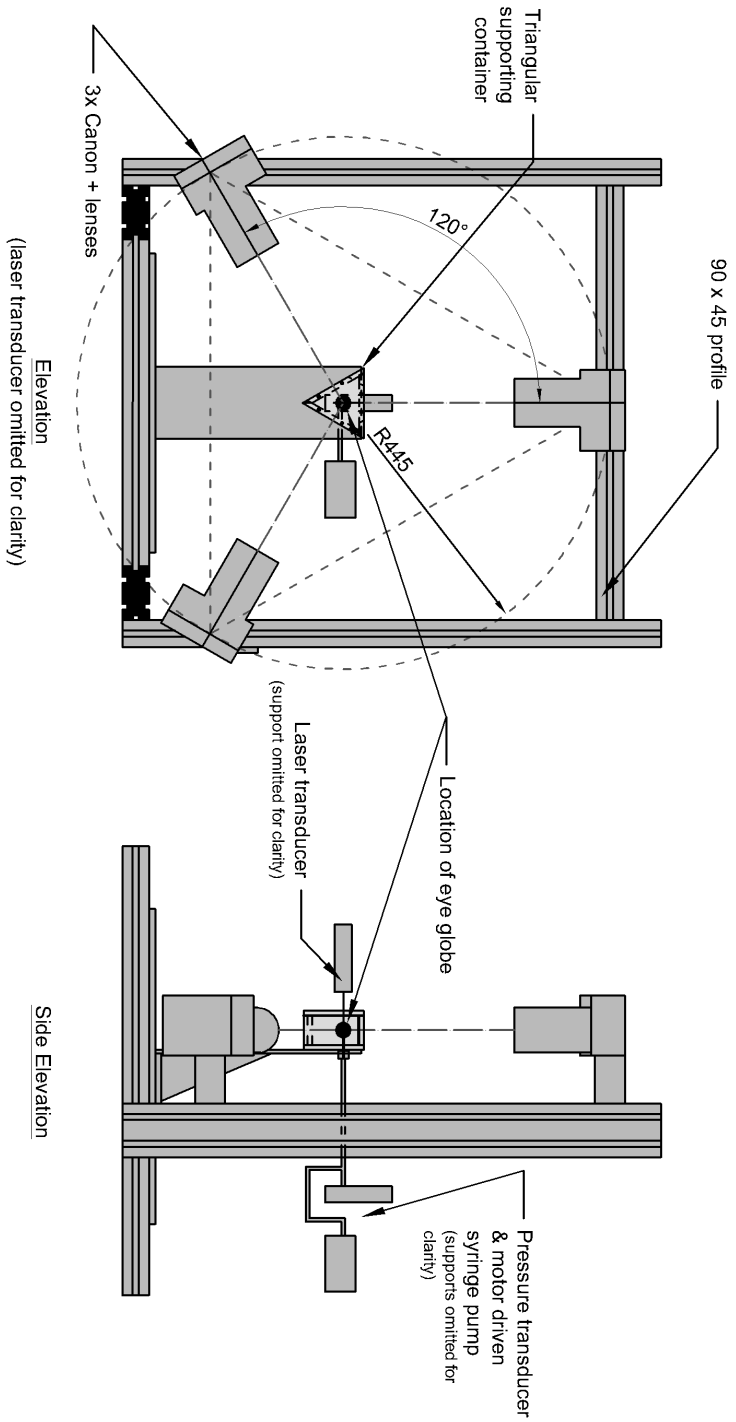

Figure 3.1: Diagram of the test rig highlighting key components and the arrangement of the measurement equipment in relation to the orientation of the eye globe.

languages and command processes utilised for this thesis research (Matlab, Python, Abaqus, Fortran, DOS and Unix) but was adopted due to its ability to communicate directly, input and output (I/O), with the DAQpad at a suitable speed. This language was utilised to provided graphical interfaces and control/feedback to experimental hardware.

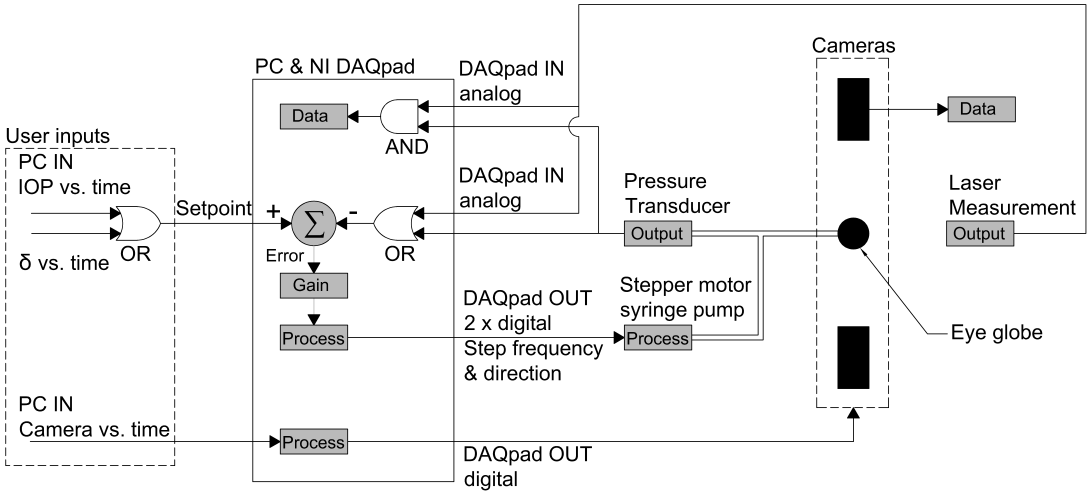

Figure 3.2: Schematic diagram of test arrangement presented in Figure 3.1. Logic symbols follow the stand format.

The most significant difference between the fore-mentioned languages and LabVIEW is the sequence of execution. Unless specific control is adopted, LabVIEW code will jump between branches of code during run-time in an uncontrolled manner. The first control over this phenomenon was to split into three distinct sections (known as *sequence structure frames*) where each frame must complete before the next frame initiates:

1. set-up of run-time constants;
2. allows the users to input variables for the test period. These variables include:
   (a) the specimen type;
   (b) specimen name;

(c) IOP or apical displacement control with respect to time;

(d) the time at which the cameras will fire during the test period.

This section of the software also allows the user to observe current IOP and laser measurements which allows the user to prepare the test environment correctly;

3. test period.

The software running on a standard (dual-processor) PC communicates with the DAQ-pad which is connected to the active components of the test rig. The DAQpad reads the voltages emitted from both the pressure and laser displacement transducers. Providing the transducers were transmitting signals based on their linear phases of measurement, the voltage was converted to measurements of pressure (mmHg), and position (μm) by calibration parameters. Calibration was performed on the pressure transducer by applying known levels of water head pressure and reading the corresponding voltage. The calibration of the laser displacement transducer was a more complex procedure due to the specific test arrangement and is covered in further detail in Section 3.2.5. In addition to reading data signals from the transducers the DAQpad also transmits signals as variation in voltage. The specific voltages were determined by the LabVIEW program. There were four signals transmitted simultaneously from four channels on the DAQpad: (1) a high/low digital signal switching on and off the stepper-motor; (2) also a high/low digital signal which controlled the direction of the stepper-motor; (3) a digital pulse wave controlling the speed of rotation of the stepper-motor; (4) another a high/low digital signal which controlled the firing of the cameras.

Changes in pressure were provided by the motorised syringe pump. The speed of actuation of the pump was controlled by the rotation speed of the stepper-motor and the pitch of the lead screw. The LabVIEW program transmits a digital pulse wave with a duty cycle of 0.5. Each occasion the stepper-motor (Nanotec L4018S1204-M6) receives a rise from low to high (once per digital pulse) it rotates by a specific rotation of 1.8°; this corresponded the a linear actuation of 5 μm; further corresponding to an applied volume of 0.06mm^2. The increase of pressure related to this applied volume was

a function of the entire system including the surface area and stiffness of the eye globes. However, an applied volume of 0.5 ml provides an increasing IOP $\approx 40 - 80$ mmHg. Due to the variation of eye globes the control had to provide stability across a wide range of systems[1]. The maximum rate of pressure increase the syringe pump was able to proved was ≈ 5000 mmHg/min.

During frame (2) the user first decides whether a displacement, or pressure, controlled test will be performed. Then the setpoint must be defined. The software was designed to allow the user to input discrete values of either δ-t or IOP-t. With these inputs the software generates a complete setpoint curve. Also during frame (2), the user enters the times at which the cameras will be fired. The software triggers all cameras simultaneously at specified times during the test. Figure 3.3 provides an example of a setpoint curve with designated moments at which the cameras fire. Images are collected and referred back to the relevant IOP after completion of the test.

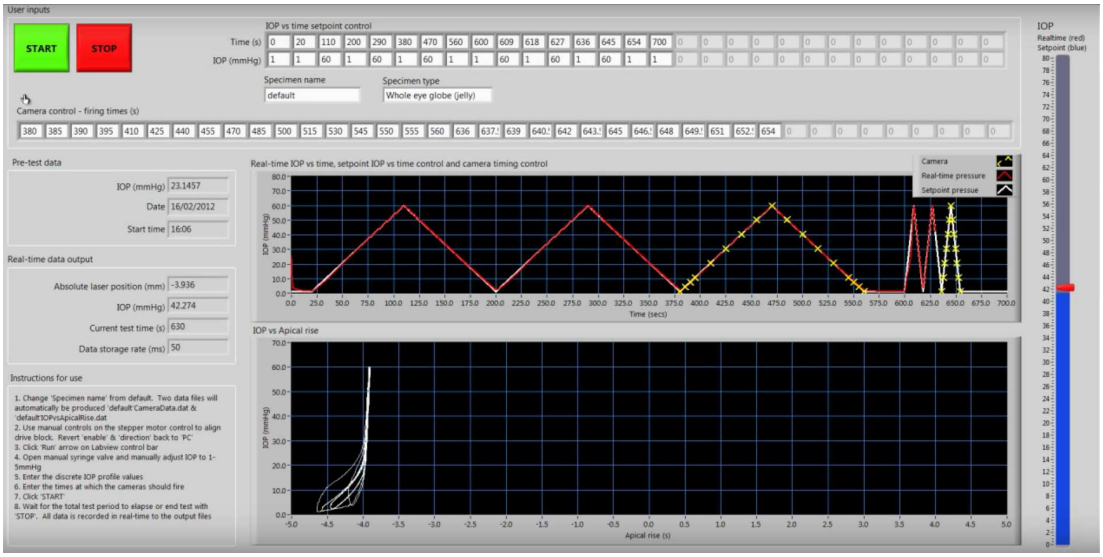

Figure 3.3: Example of setpoint (target) curve in the graphical user interface of the LabVIEW program. The white line shows a user defined IOP-t curve, the red line denotes the recorded pressure as obtained during the test, yellow crosses show the times the user has set for the cameras to fire. The bottom plot shows the IOP-displacement curve recorded from the laser and pressure transducers respectively.

[1]To further increase the scope where the system should provide effective control, the test rig was designed to test a range of specimen types (not included in this study) including rabbit corneas. Due to their size and therefore reduced compliance to increasing volume, an increase of 0.01 ml provides an increase in pressure of $\approx 30 - 50$ mmHg

Once the test has been defined the user was able to commence the test. At this moment the LabVIEW software enters frame (3). To enable appropriate control of IOP, or deformation, the software must output an appropriate digital pulse wave frequency. As neither have a linear relationship with the induced change in volume, this frequency will constantly change to accommodate the required change in response. To provide the appropriate response the program must know the current pressure or displacement. IOP and displacement are also displayed during the test and recorded for post-test analysis. Readings from both transducers are collected every 1 ms and recorded every 50 ms after filtering through a 4 Hz low-pass filter. The filter frequency and sample rates were assessed to be a suitable from calibration trials.

The output frequency of the digital pulse wave and the high/low determining the speed and direction of the stepper-motor are determined using non-linear proportional comparison. This is a modification to the commonly known *Proportional Integral Differential* (PID). The difference between the displacement or IOP setpoint and the corresponding measured value is assessed. Based on the error the output is modified. The greater the error, the faster the stepper-motor will react. There is a great deal of documentation describing the trial-and-error calibration approach to determine the most suitable proportional gain (k) value. Essentially it is a balancing process between having a system that reacts quickly enough to provide a suitable test and a stable system. Increasing k tends the system to react quickly to errors between the actual measurement and the setpoint (target). However, increasing k will also tend to increase the instability to the system. As this instability increases the actually measurement can jump around the setpoint. Decreasing k tends the system to react very slowly, in an extreme case the system can react so slowing that it never reaches the setpoint. Two adaptations were made to the standard proportional error analysis to improve the effectiveness of the system and its stability across various different system environments:

1. the error (e) as a function of the gain was non-linearised in context with the range

of setpoint by:

$$e(k) = (SP - PV)\left(L + (L-1)\frac{|SP - PV|}{SP_{range}}\right) \tag{3.1}$$

where L is the linearity factor from $0 - 1$, where 1 provides linearity and 0.1 provides a parabolic response, SP is the momentary setpoint value, PV is the process variable (in this case the stepper-motor frequency). Through an extensive range of trials a linearity factor of 0.01 was determined to be appropriate;

2. standard PID systems are a reactionary tool, such that they compare the current value with the setpoint and adjust the output accordingly. This is appropriate when a constant output will maintain the desired result once the measured value reaches the setpoint. However, this is not the case in this system. Typically IOP and deformation were required to change during the test. Even in situations were they are required to remain constant for periods, the viscoelastic behaviour of the eye globes results in required changes to the applied volume to maintain pressure and, to a lesser extent, deformation. To compensate for the reactionary behaviour of the standard PID system, the comparison was made with the future setpoint by a period of 100 ms.

Figure 3.3 provides a example of the setpoint in comparison to the measured IOP-t.

The integral and differential components of the PID were not required[2].

The runtime (control and data collection) was the most critical aspect of the program and required careful coding. To achieve a system where an acceptable match to the setpoint was achieved, and maintained, shared-memory parallel programming was adopted. Utilising dual-cores, the 1st core ran a *producer* loop (NI, 2016), while the 2nd ran a *consumer* loop. Running on a dedicated computer core, the consumer loop was centrally timed and wrote the digital-pulse-wave output to the stepper mo-

[2]Integral and differential components of the PID are typically utilised in systems altering at rates orders of magnitude faster than required in this system.

tor. This ensured that the desired frequency of digital-pulse-wave was achieved and not slowed/interrupted by the core performing other tasks. This would be performed infinitely by the *consumer* loop until which time when the *producer* loop altered the frequency and sent this command through the shared memory. The *producer* contained everything else required during the runtime including the non-linear PID, data acquisition, filtering, recording, camera firing, etc...

3.2.4 The gelatin support system

The use of a gelatin support system provided a solution to a number of challenges which presented in testing intact eye globes, namely (1), (4) and (5) (see Section 3.2.1). However, the gelatin support system introduced new challenges:

1. achieving a support condition with visual clarity and appropriate stiffness;
2. calibrating displacement measurement techniques through the transparent support system.

The eye specimen was cast into a gelatin support, which was produced from Type-A gelatin flakes derived from porcine skin (Sigma-Aldrich cat. No. G2500). This particular gelatin was chosen from trials for its clarity and low spring stiffness and because it had been reported not to chemically alter collagen based tissue (Bayless et al., 2009). In order to determine the effect of the gelatin on eye globe deformation, its spring stiffness k was measured using an Instron uniaxial machine fitted with a 10 N load cell and found to be linear of the value ($k' = \frac{F}{\delta A}$) = 0.0001 N/mm^3, where F is the applied force, δ the resulting deformation and A the cross-sectional area of gelatin material.

Finite element analysis was conducted using the non-linear solver Abaqus/Standard 6.13 (Dassault Systmes Simulia Corp., Rhode Island, USA) to determine the effect of this stiffness on the deformation of an inflating eye globe. The topography of the model was described by: a corneal radius (7.8 mm) and shape factor (0.82); a sclera radius

(11.5 mm); a central corneal thickness, CCT (545 μm reported as average value in a number of previous studies (Bennet and Rabbetts, 1989)) and a peripheral corneal thickness (695 μm, which was consistent with Gullstrands No. 1 schematic eye (Hjortdal and Jensen, 1995)). The intraocular void was represented by fluid cavity bound by the internal surface of the ocular vessel, to which it provided a uniform hydrostatic pressure that varied in the analysis to inflate the eye globe model from $0 - 30$ mmHg.

Comparison between a control finite element model (FEM) with no gelatin support and a model with an external spring condition matching the measured spring stiffness of the gelatin was conducted. Table 3.1 provides the deformations and comparison at 30 mmHg. The difference in deformation ranges between 0.05% and 0.52%. Cavity volume was also estimated in the analysis, and the internal volume of the spring-supported model was 0.06 mm^3 ($> 0.01\%$) less than the control model, once both were loaded to 30 mmHg. Based on these results the spring effect of the gelatin on the experiments was considered negligible.

Table 3.1: Deformation at discrete nodal locations from $0 - 30$ mmHg

	Control FEM deformation (μm)	FEM with simulation of gelatin support deformation, difference (μm, %)
Corneal pole	202	201, 0.49
Limbus	69.8	69.5, 0.52
Equator	58.2	58.2, -0.05
Posterior sclera	86.8	86.3, 0.52

FEM = finite element model

3.2.5 Calibration of the laser displacement sensor

The laser displacement device uses an optical triangulation position sensor to determine the distance to a near object by the recorded change in angle between the output beam and the reflected beam. Altering the media the laser travels through consequently alters the refractive angle, which in turn affects the triangulation angle. A linear

displacement calibrator with a resolution of 1 μm was used to recalibrate the laser displacement transducer through the glass box and gelatin by directly controlling and changing the distance measured by the laser. The relationship between the known relative distance and the relative distance measurements from the laser provided the calibration factor to correct the laser readings. The resulting root mean square (RMS) error after recalibration was 2.7 μm.

3.2.6 Deformation measurement by digital image correlation

DIC is an established technique that relies on the analysis of successive camera images taken for a test specimen to derive the deformation distribution across the specimen surface (Roy and Dupps, 2011). This technique has already been successfully applied, in various forms, to ocular tests (Boyce et al., 2008; Elsheikh et al., 2010a; Myers et al., 2010). This chapter describes the application of two-dimensional DIC to determine the planar deformation of the eye globes. For each camera we consider the circumferential horizon of the eye to be the planar surface. DIC was performed using the software Istra4D. There were errors in the interpretation of initial images with all image processing techniques. This was particularly apparent from distortion, which usually occurs as a result of the lens geometry and due to diffraction in the glass box and the gelatin. The process of minimising the distortion and removing, to a reasonable degree, its influence on the data is described below.

Discrete speckles of cellulose-based paints were chosen for their stability, rapid solvent evaporation and organic nature. The speckles optimised the DIC output and did not provide another surface layer to the specimens. Uniaxial tests were performed on corneal tissue, both with and without applied media, to ensure no mechanical effects resulted from this process.

Referring back to the physical setup described in Figure 3.1, the cameras were located orthogonal to the sides of the glass box. This minimises the distortion, which occurs

when light was refracted while passing between the air and the glass and between the glass and the gelatin. The error in this system of measurement was quantified using the same setup as used to calibrate the laser beam. Multiple known positions within the gelatin were measured through DIC, and the resulting RMS error between known positions and their associated measurement was 1.7 μm.

During the test, all deformations were measured relative to the single fixed position, i.e. the junction with the inflation needle. However, if this measurement was used to perform inverse modelling, the deformation at the anterior of the eye would be a function of the deformation locally and the deformation of the posterior part, therefore, all modelling errors describing the response of the posterior region would be carried forward to the analysis of the anterior region. To rectify this, the position from which the relative displacement was measured was redefined. This process is diagrammatically described in Figure 3.4; in (a) and (b) the non-deformed topographies are identical. In (b) the origin was moved to the intersection point of the line representing the limbus with the axis of the laser beam. Measurement of deformation was also obtained relative to the topography at IOP = 2mmHg, which was the minimum pressure necessary to remove initial wrinkles on the ocular surface. Ten discrete locations were measured from each camera: corneal apex and posterior pole; the mid cornea, limbus, equator and posterior sclera on the left and right sides of the images. In total, twenty-six measurements of deformation were obtained from each camera. The deformation at more points could be obtained using this process, but it was found in this work that having pressure-deformation behaviour at 26 points was sufficient for obtaining unique values for the material parameters of ocular tissue as described below.

3.2.7 Tissue thickness measurements

Measuring the topography of the eye accurately is of clear importance when building geometric numerical representations. Equally important is to accurately determine the internal topography. This is typically done by measuring the thickness of the ocular

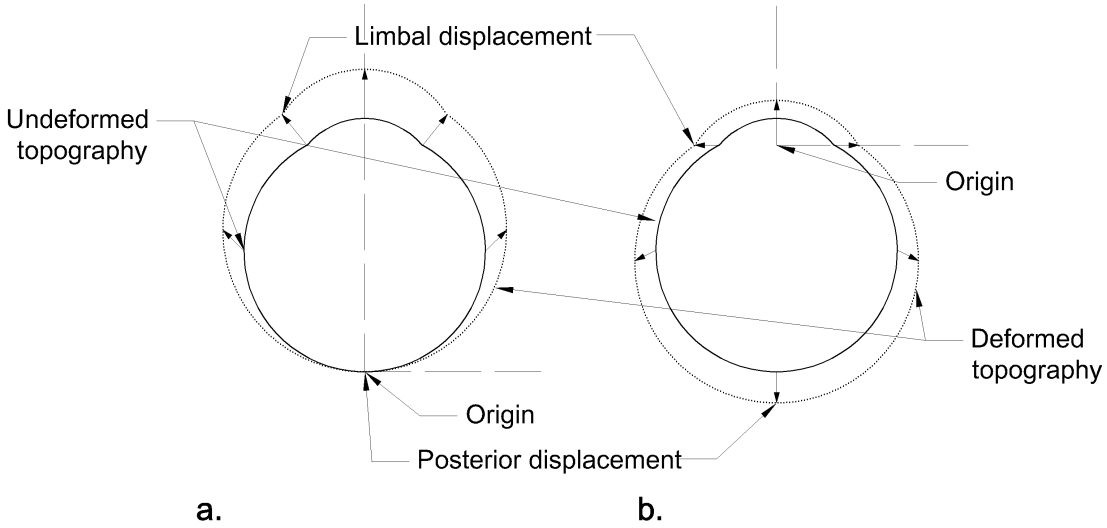

Figure 3.4: Diagrammatic representation of the analysis of displacement. (a) and (b) share the same reference and deformed topographies. (a) represents the displacement as initially measured. (a) shows the deformed image that has been reoriented such that the origin is the intersection point of the line representing the limbus with the axis of the laser beam.

vessel (Elsheikh et al., 2010a) at which time the internal topography becomes a relationship between the external topography and the thickness. Implementation of this is presented in Chapter 4.

In a number of previous studies the thickness has been measured by a Pauchymeter (DGH 55, Exton PA, USA). This device is widely considered to be suitable for measuring corneal thickness *in vivo*. However, there are limitations to consider when measuring thickness of the entire ocular vessel *ex vivo*:

1. the device is limited to a thickness measurement range upto 1 mm which is on the boundary of thickness observed in some sclera (see Chapter 1);

2. the device is reliant on consistent media density to provide consistent thickness measurements due to its use of ultrasound;

3. the device is reliant on the user to apply a consistent normal force to the tissue when acquiring readings.

The last is very significant, during *in vivo* conditions the corneas thickness is relatively unaffected from an increased normal force by the operator as such a force simply displaces aqueous humor in the anterior chamber resulting in deformation of the cornea. In this instance the corneas thickness will only reduce as a function of increased surface area due to deformation. However, during *ex vivo* measurement acquisition the specimen has undertaken dissection. This is required to remove media such as the ciliary body, choriod, retina and lens, which would otherwise effect readings of the stromal thickness. As the ocular vessel is no longer supported by IOP it requires mechanically supporting. It is the interaction between the Pachymeter and the mechanical support which would most adversely effect the thickness readings as increased force from the user will no longer simply displace intraocular media but locally compress the stroma under the tip of the measurement device. A new system of measurement was therefore required. A contact device was developed using a linear displacement actuator, a load-cell and synthetic ruby stylus interfaces, Figure 3.5. The actuator (RDP LTA-HS) provided positional control with an accuracy of 0.001 ± 0.00001 mm. The load-cell (RDP 060-1426-03) (of had a linear range of $0 - 2.5$ N with an accuracy of 1 ± 0.5 µm. The top and bottom synthetic ruby stylus provided diameters of 1 and 5 mm respectively (Renishaw Part No. A-5000-7808 and A-5003-0048), with an accuracy of 1 ± 0.5 µm. This device is controlled through a LabVIEW program (similar, but less complex, to inflation equipment control). Utilising feedback from the load-cell the normal contact pressure is limited to a user defined 0.001 ± 0.00001 N. The accuracy of the device was assessed through a calibration process measuring plates of known thickness ranging from $0.5 - 25$ mm. The accuracy of plates quoted by manufacturer was 4 ± 2µm. In comparison the measurements obtained from the device showed an accuracy 1 ± 0.5 µm which is less than the quoted accuracy of the plates. These results demonstrated a suitable level of accuracy and repeatability which was unaffected by user inconsistency.

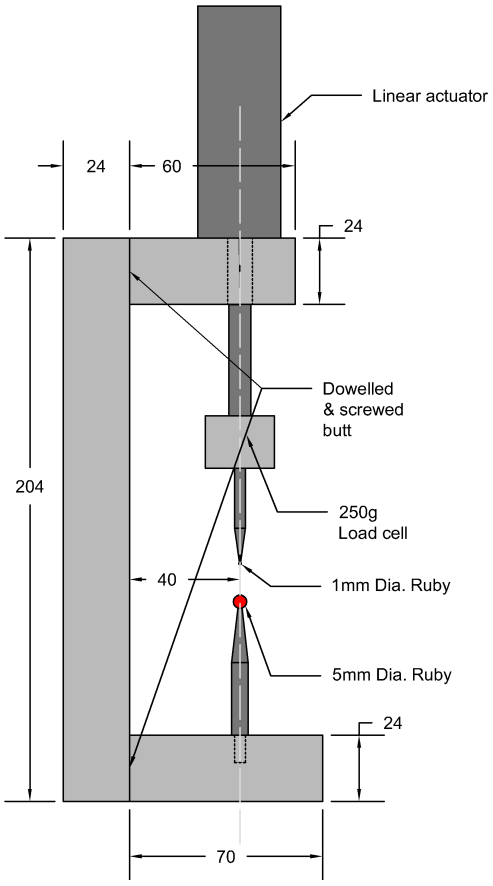

Figure 3.5: Diagram of the thickness measurement device highlighting key components.

3.2.8 Geometric modelling

Accurate measurements of deformation and loading, and accurate representation of boundary conditions are required to derive representative material properties from an inverse analysis process. Additionally, the reliability of the derived material properties is reliant on an accurate representation of the geometry of the specimen within the finite element simulation. This section describes the method used to recreate the geometry of the specimen in the form of an FEM and the method used to quantify and minimise errors.

The geometry of the models was constructed as an orphan mesh for use with Abaqus using bespoke software (further details on this software is provided in Chapter 4. The external topography was created from six individual meridian profiles from the three cameras at IOP = 2 mmHg. These profiles were calibrated and aligned with each other in the 3D space based on the common polar axis, which was defined by the needle. The internal topography was based on the external topography and eight meridian profiles of discrete thickness measurements. The thickness was measured at 2 mm intervals along each meridian from pole to pole (Elsheikh et al., 2010a). The internal and external 3D topography was interpolated based on the relative spherical coordinates between the discrete points of measurement. The resulting FEM of the eye globe was free from restrictions of rotational symmetry. The images used to construct the geometry were calibrated by camera constants: the angle, the central position of the polar axis in the image, and the mm/pixel ratio which ranged from 0.0120 to 0.0122 for the three cameras, Figure 3.1. The error in this method was determined by numerically reconstructing a Grade 100 Chromium (AISI52100) hardened ball bearing with diameter measurements of 12.5 mm $\pm$2.5 μm. The ball, which was contained within the gelatin, was numerically reconstructed with a resulting RMS error of 49 μm.

The lamina cribrosa was represented by a thinned section of the FEM. The central thickness of this section is fifty percent less than the value in surrounding tissue; in

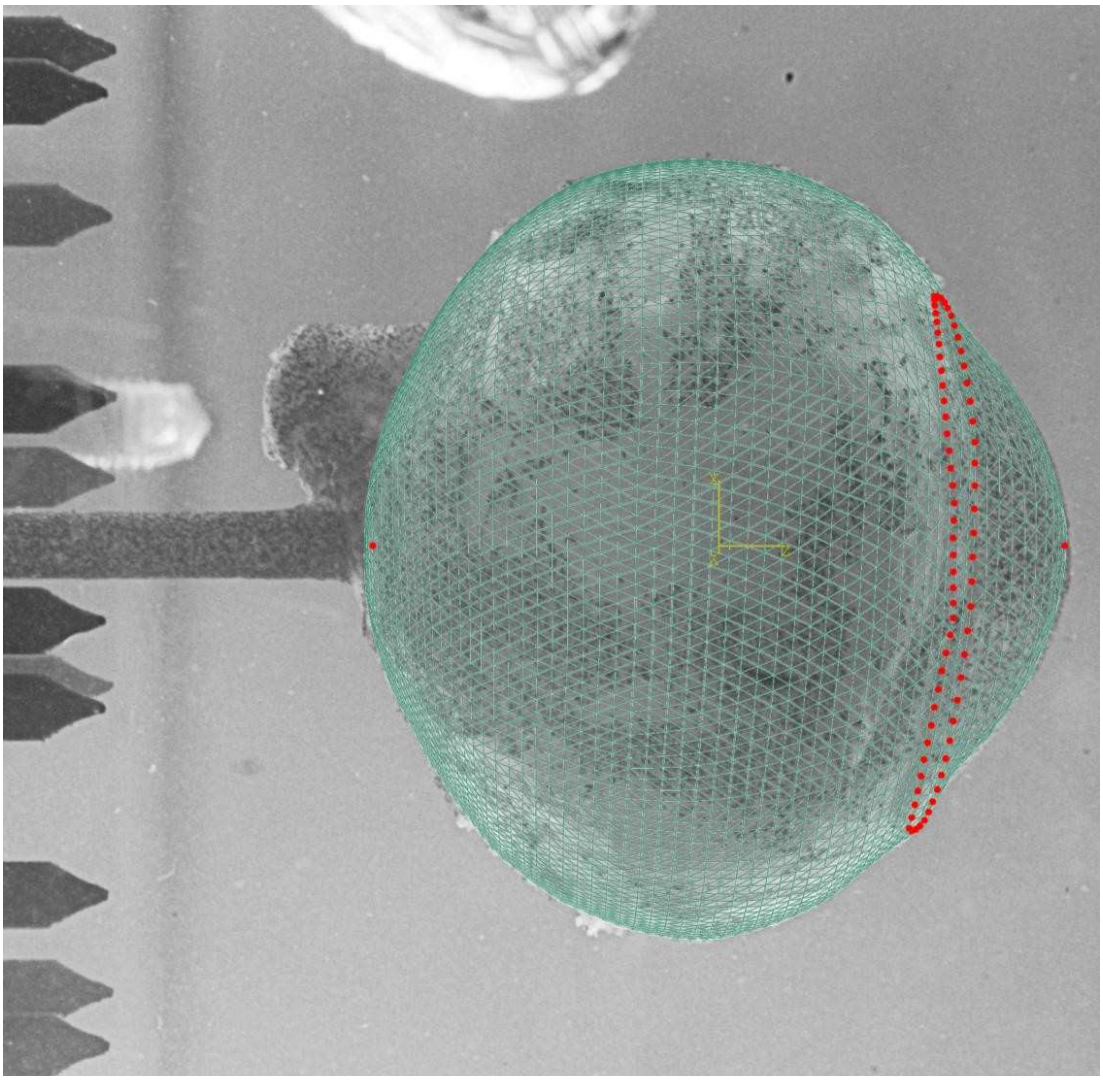

Figure 3.6: Match between modelled and imaged topography of the eye globe. The nodes representing the corneal apex, posterior pole and limbal ring are highlighted in red.

addition the material was represented with a Youngs modulus of 0.32 MPa and a Poisson's ratio of 0.49 (Sigal et al., 2005). Boundary conditions were provided to restrict the model from free body movement and provided an origin of deformation, which matches that applied to experimental data. IOP was represented by a distributed surface load (Abaqus keyword, *DSLOAD) applied to the internal surface of the model. This loading is appropriate in these cases where no external loads are applied and cavity volume output is not required. The models were constructed from seventy circumferential rings of quadratic, wedge-shaped, hybrid elements (Abaqus, C3D15H). The element type and the quantity have been chosen to create a smooth geometric representation, minimal volume locking, isotropic response to isotropic strain (see Chapter 4 for more detail) and adequate mesh refinement while keeping processing time at a reasonable level. The resulting model is shown in Figure 3.7, which also shows the nine regions (colour coded) of the FEM, which provide nine ocular regions, each assumed to have unique material properties. The arrangement of the nine regions in the anterior-posterior direction was justified by the deformation maps obtained from the DIC analysis, in which the deformation contour lines were mainly parallel to the coronal plane of the eye. The number of regions was determined to provide the greatest model refinement achievable, while remaining able to provide unique values of the material parameters for tissue in each of the nine segments within an inverse analysis process.

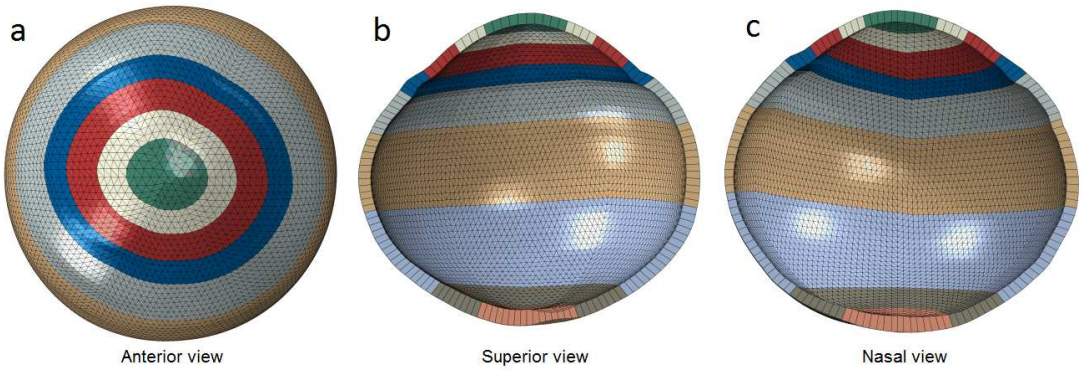

Figure 3.7: Finite element model of a tested porcine eye globe. (a) image viewed from the corneal apex. Images (b) and (c) are cross-sections viewed from the equator. Image (b) sections through the reduced thickness location representing the lamina cribrosa. All images show the regions of various material definitions in the model, with dark blue representing the limbal region.

3.2.9 Inverse analysis

Ocular material behaviour parameters were derived from the experimental data using HEEDS (v6.1, Red Cedar Inc., USA), in conjunction with Abaqus. The optimisation was based on determining material parameters that provided the best possible match between applied pressure and deformation results, as obtained experimentally and predicted numerically. The optimisation was based on the SHERPA algorithm that utilises Monte Carlo sampling to find a robustness and unique solution. The algorithms objective function was to minimise the RMS error between the sets of experimental and numerical data as percentages of the final deformation at the relevant location;

$$RMS = \frac{1}{M}\sum_{j=1}^{M}\frac{\sqrt{\frac{1}{N}\sum_{i=1}^{N}\left(\delta_{i,j}^{experimental}-\delta_{i,j}^{numerical}\right)^2}}{\delta_{max,j}^{experimental}}\times 100 \tag{3.2}$$

where N is the number of pressure levels, M = 26 is the number of measurement locations and $\delta_{i,j}$ is the deformation at each particular pressure, at each location. As the deformation was measured relative to the geometry at IOP = 2 mmHg, FEA was performed over two stages. The first stage elevated IOP to match that of the initial pressure of the experiment, and the second stage increased IOP to the final pressure. The deformation from the FEA ($\delta_i^{numerical}$) was recorded relative to the beginning of the second stage.

The numerical model used to describe the material behaviour of the ocular tissue during loading was the hyperelastic Ogden model, utilised in a number of previous studies on soft tissue (Groves et al., 2012; Moran et al., 2014; Yu et al., 2013), and presented in Equation 3.3 in terms of the strain energy per unit volume, W:

$$W = \sum_{i=1}^{N}\frac{2\mu_i}{\alpha_i^2}\left(\lambda_x^{\acute{\alpha}_1}+\lambda_y^{\acute{\alpha}_1}+\lambda_z^{\acute{\alpha}_1}-3\right)+\sum_{i=1}^{N}\frac{1}{D_i}\left(J-1\right)^{2_i} \tag{3.3}$$

where $\lambda_k^{\acute{\alpha}}$ are the deviatoric principal stretches equal to $J_k^{\frac{-1}{3}}$; $(k = x, y, z)$; $J = \lambda_x, \lambda_y, \lambda_z$ where $\lambda_x, \lambda_y, \lambda_z$ are the principal stretches in the three main Cartesian directions. The

material parameters denoting the strain hardening exponent and the shear modulus are α_i and μ_i $(i = 1 \dots N)$ respectively, where N is the function order. The product of stretch in all three directions, $J = \lambda_x, \lambda_y, \lambda_z = 1$, following the approximation that ocular tissue is an almost incompressible material (Kampmeier et al., 2000). The values of material parameters α_i and μ_i represented the output of the inverse modelling process described above. The use of a first order material model, $N = 1$, reduced computation time during the modelling procedure by reducing the number of variables requiring optimisation and was found to produce stable results.

In addition to the utilisation of Monte Carlo sampling to enhance uniqueness, uniqueness was ensured by repeating the inverse analysis twelve times. For each run, the baseline and boundaries of the solution space were altered within sensible but exploratory limits, $(0 < p < 4s)$, where p is the optimized parameter and s is the best fit parameter value.

3.2.10 Experimental procedure

To illustrate the results of the test method, one human eye and one porcine eye were tested and the results analysed to produce estimates of material parameters for different regions of the eye globes. The human eye, of a 69-year-old male with no known ocular diseases was obtained fresh from the Fondazione Banca degli Occhi del Veneto, Italy. The porcine eye was obtained within 6 hours of slaughter. Both eye globes were stored in 6% Dextran prior to the test. The aqueous and vitreous were removed through the needle and the intra-ocular void was filled with 6% Dextran. Once contained within the gelatin and connected to the test rig, the IOP was altered by the control system described above. Both the human and porcine eyes were loaded and unloaded from 2 to 60 mmHg at a rate of 40 mmHg/min, with a rest period of 1 min following each of 10 loading cycles. The peak load of 60 mmHg, which is above the normal physiological range, was chosen to reach the higher IOP ranges associated with eye rubbing and tonometry.

The preparation procedure developed for this study therefore undertook significant trialling and optimization. The detailed timing and method of preparation can be found in Appendix B

A video of the arrangement and test procedure can also be found by following the link:
https://www.youtube.com/watch?v=_LsMed7twKQ&feature=youtu.be

3.3 Results

3.3.1 Human eye

By providing a measurement of displacement from the posterior pole to the corneal apex with respect to IOP, the laser and pressure readings indicate the global response of the eyes. Figure 3.8(a) provides all displacement curves for the 10 cycles of loading applied to the human eye. This shows that up to 24 mmHg there is no overlap between the loading and unloading curves of successive cycles. Above this level there are still distinct trends within the displacement responses, which are independent of the cycle. Figure 3.8(b) highlights the first and last cycles where the difference in maximum displacement is 26 μm. Some differences can be found between the shapes in the displacement curves; between $24 - 45$ mmHg the global response of the human eye globe is more compliant in the last cycle. There is a reduced global viscoelastic effect evidenced when comparing loading and unloading curves for these cycles; this is particularly apparent at IOP > 45 mmHg where the loading and unloading curves of the last cycle coincide. However, there is no significant difference in the curves up to 20 mmHg; both the first and last cycles exhibit similar relationships of global stiffness, non-linearity and viscoelastic effects. The recovery behaviour at 2 mmHg shows that there was complete recovery. The axial displacement observed at the beginning and the end of the tenth cycle indicates that there is less deformation than observed at the

beginning of the test cycles.

As previously described, the DIC measurements of displacement have been reori-

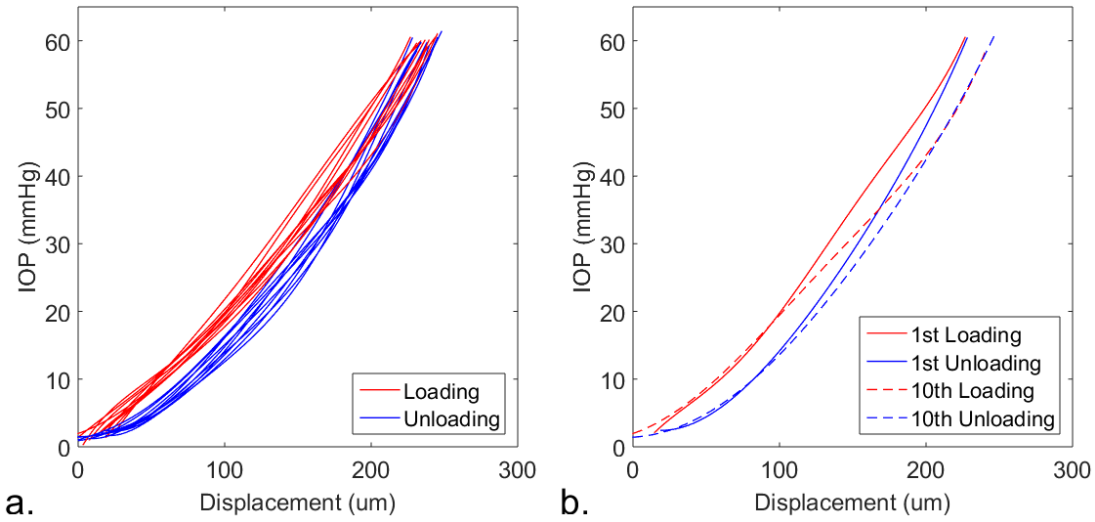

Figure 3.8: Load-displacement curves obtained for the human eye globe from the laser measurement device and pressure transducer. Displacement is measured in the coinciding axis of the laser and inflation needle. Plot (a) provides the curves for all 10 cycles including the recovery periods. Plot (b) highlights the 1st and 10th cycles.

ented. The resulting pressure-displacement curves for the human eye are provided in Figure 3.8. The displacement measurement for the human eye in the central cornea has changed from 230 µm to 45 µm due the transfer of the origin from the posterior pole to the limbal region (see Figure 3.4). The displacement of the posterior pole has increased from 0 to 185 µm in the same manner. However, the combined displacement along this axis measured by DIC remains consistent with the laser measurement, which was used for direct measurement and validation purposes. The peripheral cornea shows maximum displacement measurements from 33 to 55 µm at 60 mmHg with an average displacement of 44 µm. These measurements were obtained in different locations across the peripheral region and do not share the same polar or azimuth angles. Limbal displacement is now measured perpendicular to the axis of the laser and needle within a range of 15 to 46 µm with an average displacement of 31 µm. Similarly, displacements of 40, $30-48$ µm (mean, range) and 62, $54-85$ µm at 60 mmHg were measured in the anterior and posterior scleral regions respectively.

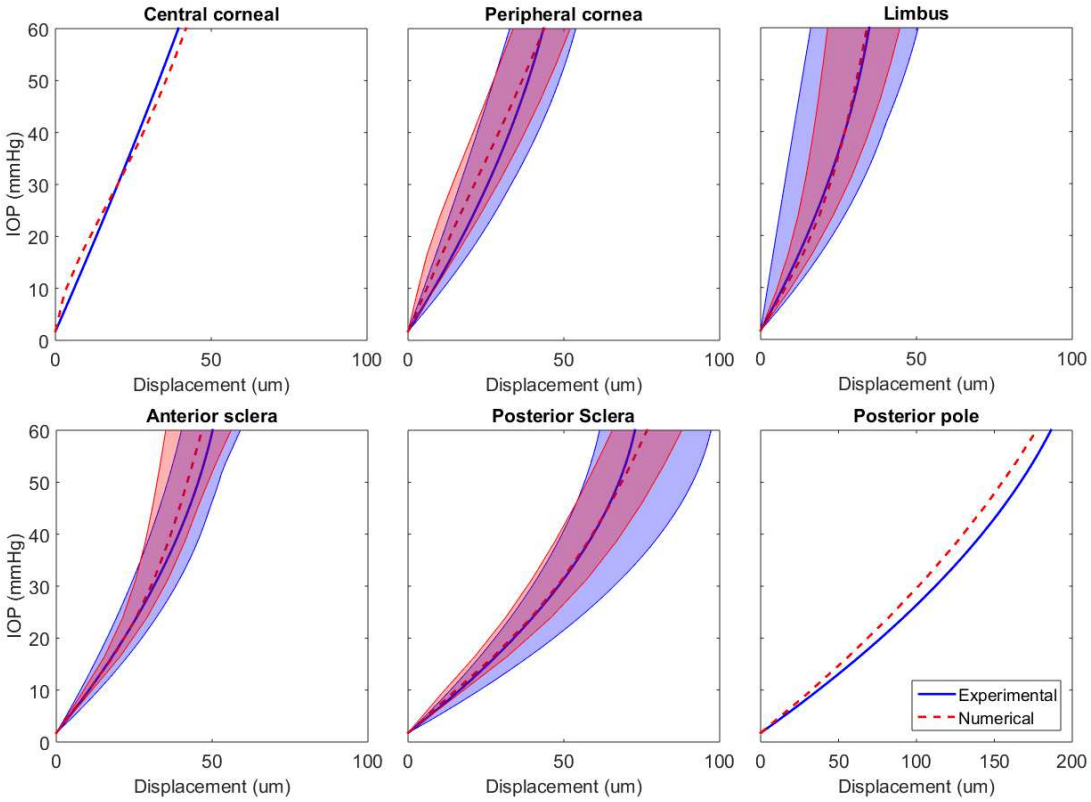

Figure 3.9: Experimental results obtained from DIC for the human eye globe with the corresponding numerical representation to 60mmHg. Mean results for regional behaviour are represented by the thick dotted (numerical) and solid (experimental) lines. The shaded areas represent the range of results within the regions.

Inverse analysis has aimed to provide a match of the displacements measured from the experiment (Figure 3.9) with those of the specimen-specific model shown in Figure 3.10. An RMS error between the displacement predictions of the model and the experimental data of $< 10\%$ was achieved. Comparing the mean curves from within the peripheral cornea, limbus and anterior and posterior sclera regions, the RMS error was $< 8\%$. The latitudinal variation in displacement response within these regions was small and has been represented most accurately in the peripheral cornea and anterior sclera. However, the latitudinal variation in displacement was larger, and hence less accurately represented, around the limbus and in the posterior sclera, which contributed to the overall error in matching the experimental load-displacement behaviour.

The resulting material representations that have been derived for regions of the human eye globe can be considered by the numerical parameters α and μ, as seen in Table 3.2. α, relating to the non-linearity and stiffness, decreases from the central to peripheral cornea; is highest at the limbus; and reduces again towards the posterior pole region. μ, relating to the initial shear modulus, is lowest at the central corneal region; increases through the peripheral corneal to the limbus where again it is highest; and once again reduces from the limbal to posterior pole region. The uniqueness test showed that for seven out of the twelve inverse analysis runs, the best fit parameters varied by less than 0.5% with similar RMS errors to the best fit of all the trials. The remaining five cases resulted in RMS errors ranging from $15 - 40\%$. In these cases, the parameter boundaries were outside the range of the best fit solutions.

Biomechanical representation can be considered by the resulting contour plots of stress and strain across the eye globe, as provided in Figure 3.10 at 60 mmHg. In the model the lamina cribrosa exhibits the greatest stress and strain due to its mechanical compliance and linear representation. Across the stroma the cornea exhibits the greatest strain in the model. Unlike the derived material behavioural properties, there is no significant trend in the strain from anterior to posterior sclera. The stress in the cornea at IOP = 60 mmHg is similar to the majority of the sclera. However, there are areas of

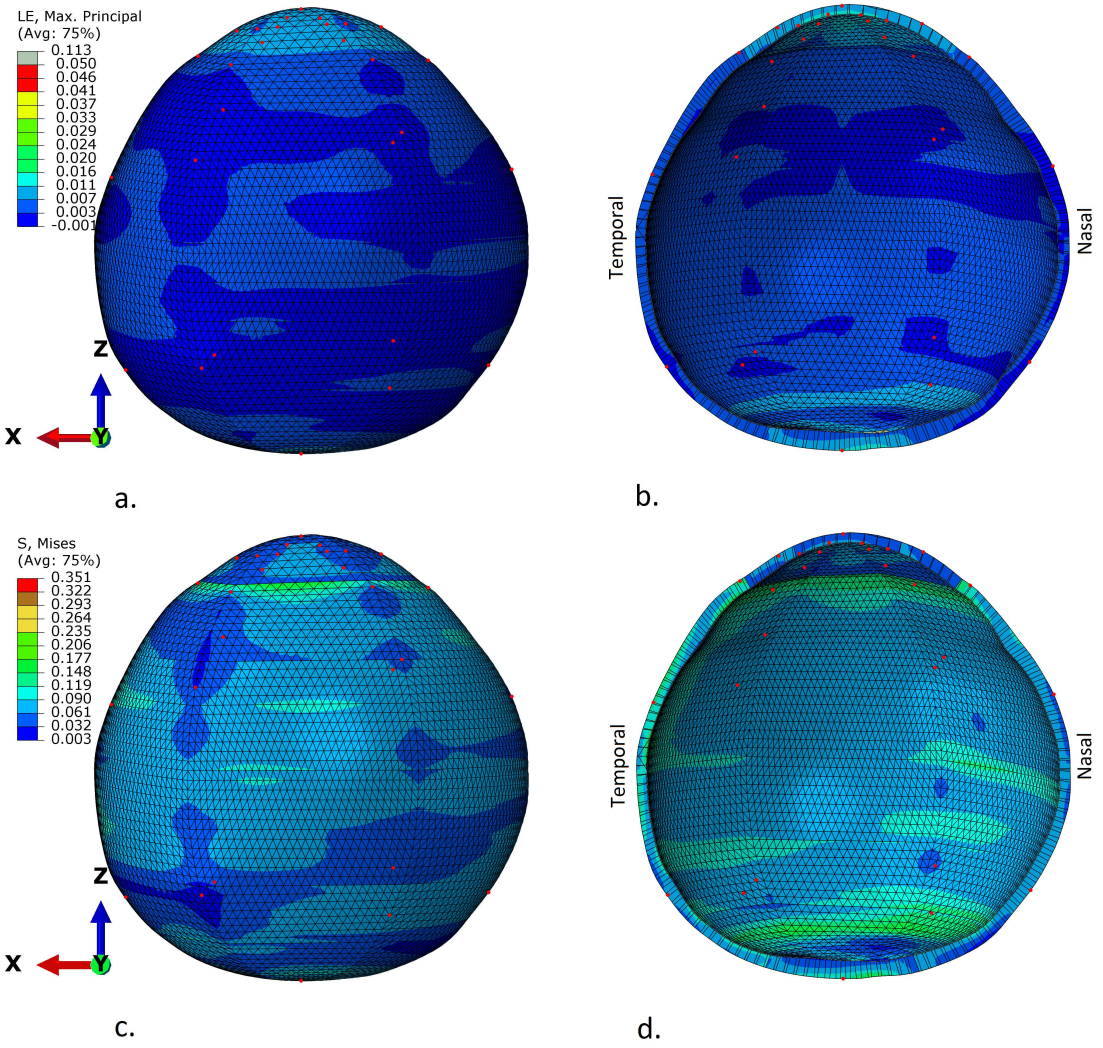

Figure 3.10: Finite element model of the human eye with stress and strain distribution plotted at 60 mmHg; as seen from the superior point-of-view. The z axis is collinear with the axis of the laser measurement and inflation needle during the test. (a) and (b) provide strain maps of the eye globe; while (c) and (d) provide the stress in MPa. (b) and (d) provide cross-sectional views that depict the variation of thickness and the lamina cribrosa. Red dots show the locations of the DIC measurements and fitting locations for the inverse analysis procedure.

Table 3.2: Numerical parameters derived to represent the regional variation in material response for the human and porcine eye globes based on the Ogden model

Region	Human eye		Porcine eye	
	α	μ	α	μ
Central cornea	157.8	0.8100	220.1	0.0181
Peripheral cornea	117.1	1.332	114.3	0.0132
			110.2	0.0092
Limbal region	472.4	4.844	127.2	0.545
Anterior sclera	370.1	4.716	162.3	0.565
Equatorial region	344.9	5.920	181.3	0.642
	228.4	4.468	164.2	0.673
Posterior sclera	169.3	3.784	134.2	0.621
	157.6	2.672	118.2	0.592
Posterior pole region	127.9	1.894	95.62	0.535

the sclera, which exhibit higher stress particularly in the temporal region. The region of highest stromal stress is in the limbus.

3.3.2 Porcine eye

DIC results (Figure 3.11) obtained from the porcine eye reveal that the eye globe was relatively compliant at low IOP with highly nonlinear displacement responses; which was particularly apparent in the cornea. Experimental and numerical results are provided to 25mmHg, above which the behaviour was essentially linear. At this IOP, the central cornea exhibits displacement of 400 μm. The peripheral cornea, limbus and anterior sclera exhibit large latitudinal variation in displacement within each region; this characteristic reduces towards the posterior pole.

The inverse analysis for the porcine eye provided material parameter estimations with a RMS error at 26% due to the significantly larger latitudinal variations in displacement within each eye region. The values of material parameters, α and μ, obtained for the tested eye are presented in Table 3.2.

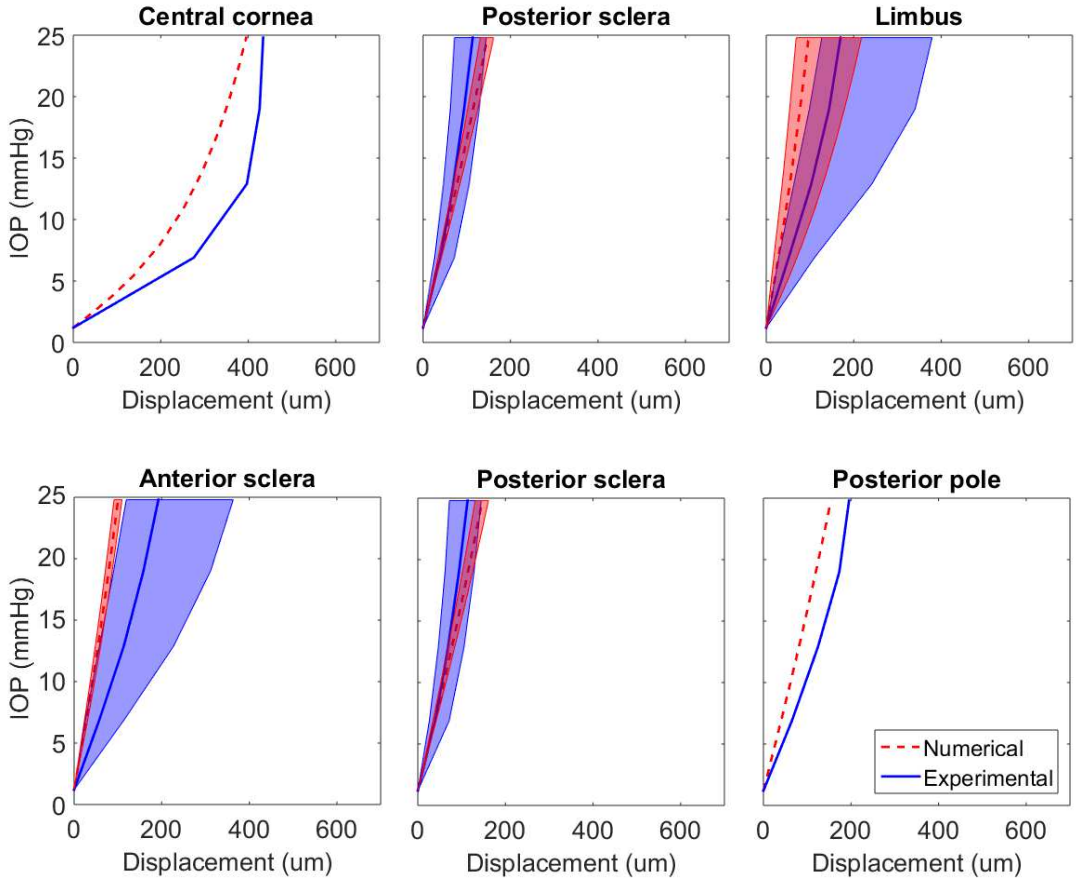

Figure 3.11: Experimental results obtained from DIC for the porcine eye globe with the corresponding numerical representation to 25 mmHg. Mean results for regional behaviour are represented by the thick dotted (numerical) and solid (experimental) lines. The shaded areas represent the range of results within the regions.

3.4 Discussion

A significant benefit of intact globe testing is the ability to estimate the regional variation of stiffness across the cornea, limbus and sclera. Previous experimental analysis of these variations has mostly been limited to separated corneas and scleras, obtained from different donors in most cases. The limbal region is commonly used for clamping the separated cornea and sclera specimens and hence is not usually characterised. Additionally, the clamps provide unrealistic boundary conditions, which are likely to affect the behaviour obtained experimentally in the adjacent areas. Therefore, the procedure described in this study is of particular benefit for obtaining material stiffness properties at the corneoscleral junction, providing the eye with physiologic loading and supporting conditions and correlating the behaviour in the cornea to that in the sclera.

The main objective of this study was to provide a method for determining the material stiffness of the eye globe, which more accurately represents *in vivo* state. The microstructural effects of tissue manipulation (as is inherent in strip uniaxial testing), and the associated deviation from *in vivo* strain distributions, have led in other test methods to the necessity for preconditioning before a consistent, cyclic stress-strain behaviour is observed (Cheng et al., 2009). The realignment of collagen fibrils during load cycles has been characterised by Quinn and Winkelstein (2011) for ligaments, which also consist mainly of collagen fibrils. Quinn and Winkelstein's study demonstrated a strong correlation between changes in collagen fibril alignment and changes in the mechanical response during preconditioning cycles as fibrils are able to change direction towards that of the principal strain. The pressure-displacement measurements of the eye globes tested suggest that no stiffening occurred between the 10 repetitive cycles, possibly as a result of no microstructural changes taking place. Subsequently, there is reduced need for pre-conditioning with the intact eye inflation procedure, which loads and supports the eye in a similar fashion to the *in vivo* conditions.

The limited experimental testing of one human and one porcine eye, included in this

study, was presented mainly to illustrate the whole-globe inflation and the results that can be obtained from it. While the results presented show interesting trends that could only be obtained through whole-globe testing, they will need confirmation in studies involving larger numbers of test specimens.

In the test conducted on a human eye, inverse analysis allowed observation of high stiffness at the limbal region and the ring of scleral tissue immediately adjacent to it, reducing gradually towards the posterior pole. At the same time, the central cornea had a higher stiffness than the peripheral cornea, and both were much more compliant than the limbus. This behaviour is compatible with trends in material properties reported in previous studies (Coudrillier et al., 2012; Elsheikh et al., 2008b, 2010a). While there was a decrease in the non-linear stiffness parameter, α, from the central to peripheral cornea, analysis revealed an increase in the initial shear modulus parameter, μ. This suggests a consistency with findings of previous studies which describe increased interweaving of collagen lamellae in the peripheral cornea (Abass et al., 2015). On the other hand, while the derived material stiffness parameters reduce from anterior to posterior sclera, observation of the stress and strain maps reveal relative consistency across these regions suggesting that these changes are compensated by the variation in thickness (geometric contribution to stiffness).

The inverse analysis included within the method description and performed in this study assumed isotropy of material behaviour. This is despite the fact that the mechanical response of ocular tissue is known to be anisotropic and that a number of studies have utilised characteristic anisotropic microstructure arrangements (Aghamohammadzadeh et al., 2004; Boote et al., 2006) in numerical representation of the cornea (Studer et al., 2010). However, since there was no data providing characteristic microstructure relationships covering the entire eye globe, it was not possible in this study to adopt an anisotropic numerical representation of the tissue.

The results obtained immediately adjacent to the posterior pole may have been com-

promised by the insertion of the inflation needle. Due to the process of reorienting the DIC measurement such that the origin was no longer located at the posterior pole, the potential inaccuracies in this area did not compound smaller errors in the derivation of material parameters elsewhere across the eye globe. The response to increases in IOP is a global response and errors in the representation of one region will always affect another region. However, it is suggested that this transfer of the origin to the limbal region has improved the reliability in the derivation of properties particularly at the limbus and across the cornea as this effect has been limited.

For the porcine eye, while the experimental procedure was applied successfully, the inverse analysis produced larger errors due to considerable latitudinal variation in behaviour within each of the model's nine regions. This is most prominent in the mid cornea, limbal and equatorial regions. While the non-rotational representation of the specimen specific geometry was considered, the FEM was limited to rotationally symmetric material representation, which meant that the variation in stiffness could only arise due to the slightly irregular geometry around latitudinal regions. However, it is clear from the fitting of numerical to experimental data in the porcine eye that variations in geometry alone did not entirely represent the variation in stiffness, suggesting the need to consider possibly significant variations in material stiffness around these latitudinal regions when modelling porcine eye globes. This makes it more important to consider the anisotropic fibril distribution across the ocular surface once this information becomes available.

The study demonstrated that preconditioning cycles may not be required to obtain consistent load-deformation behaviour in globe inflation testing. This is a result of the test procedure providing a strain distribution that closely represents that of the *in vivo* eye and does not involve significant surgical manipulation as those factors would otherwise result in fibre re-orientation, and hence tissue stiffening, between successive preconditioning cycles. These findings are consistent with an earlier study on sections of non-human ocular tissue (Tonge et al., 2013).

While the test procedure presented in this study represents a significant improvement in the ability to derive regional stiffness variations consistent with the *in vivo* eye, the method including the experimental testing and associated data analysis is substantially more demanding and more complex than uniaxial strip extensometry and inflation of separated corneas and scleras. However, despite these challenges and the difficulties in acquiring whole eye globes for research, the novelty of the technique and the more comprehensive data it offers make the method invaluable in ocular material characterisation, especially as microstructure data covering the whole ocular surface becomes available.

Chapter 4

Numerical Analysis

The following chapter presents various aspects of numerical analysis which form part of this present study. Accurate finite element analysis can lead to improvements in heathcare which is the ultimate goal of biomechanics. The development of more accurate and representative numerical models are presented in this chapter. To achieve this a number of facets required consideration:

1. development of finite element models representing both characteristic and specimen specific ocular geometry;
2. defining boundary conditions which represent the interactions at boundaries of the stroma, such as IOP, limbal support and tonometry loading;
3. obtaining the stress-free configuration, such that required topography can be provided with IOP greater than zero;
4. providing material definition.

4.1 Finite Element Mesh Generation

Traditional methods of generating finite element models utilise computer added design (CAD) techniques. These techniques involve the construction of geometry which is then converted to a mesh geometry often within a FEA package. During this stage-by-stage process geometry is developed, seeded and then meshed (Abaqus, 2013b). It is typical within such a procedure to allow the FEA preprocessing software to select the appropriate type of element. In practical terms, this technique is not suitable for modelling the ocular vessel due to the ranges and complexities in the geometry. To overcome this, bespoke software was created to model both characteristic and specimen specific geometries.

The software generates geometry as a system of finite elements. These elements are defined by nodal coordinates in a Cartesian configuration and written to the *.inp file. This geometry is used directly by the finite element solver. This method of directly providing the mesh geometry to the solver is defined as *orphan mesh* as it has no parent geometric information. In addition to geometry, the bespoke software also enables the user to define basic material and boundary conditions which are written to the *.inp by an automated procedure. Where less standard definitions were required, these were coded directly to the *.inp. The combination of the orphan mesh and direct, or bespoke automation of model parameters negates the requirement of a FEA pre-processor.

4.1.1 Element Selection

Due to the adoption of orphan mesh development, the FEA package cannot be relied upon to provide appropriate mesh/element arrangement and construction. A procedure to assess appropriate element selection and arrangement was therefore adopted and is described in this section.

Elsheikh and Wang (2007) had previously utilised 6-node, linear, prismatic elements

to describe the geometry of the eye. To contextualise this selection, these models were used in conjunction with material models such as Ogden (1984). Subsequently in this thesis, new constitutive material models are presented. Abaqus (2013a) and Abaqus (2013c) warn the user against the usage of linear prismatic elements particularly during the utilisation of user defined material models. This warning is due to the phenomenon known as volume- or shear-locking where elements behave in a stiffer manner than intended due to geometric numerical restrictions.

Element types were assessed to determine their suitability. A simple slab was generated as an orphan mesh. This slab geometry was generated with five different arrangements and types of elements: 1, 2 and 3 layers of 6-node linear prismatic elements; 1 layer of 15-node, non-linear prismatic elements; and 1 layer of 8-node cubic elements, as seen in Figure 4.1. During a procedure where Abaqus is free to generate the optimum mesh arrangement, 8-node elements are selected where possible and this arrangement is considered to provide a reliable datum with which to select an appropriate element type (Abaqus, 2013b).

It was desirable that prismatic elements would be deemed appropriate as it had been found in a previous study that such elements provided a suitable geometric approximation of the surface topography of the cornea (Elsheikh and Wang, 2007). Each model was subject to multiple loading conditions: bending, shear, axial tension and compression. Potential anisotropic response of the elements was tested using the isotropic, hyperelastic Ogden and linear elastic material models. For further details on the Ogden material model please refer to Chapter.2.

From the contour plots of stress distributions provided in Figure 4.1, and the further results in Appendix C, it is clear that the use of linear prismatic elements result in non-symmetric stress distributions and deformations when all other aspects (geometry, loading and boundary conditions) are symmetrical. This suggests that the response of the elements are anisotropic to isotropic loading. As expected, the cubic elements

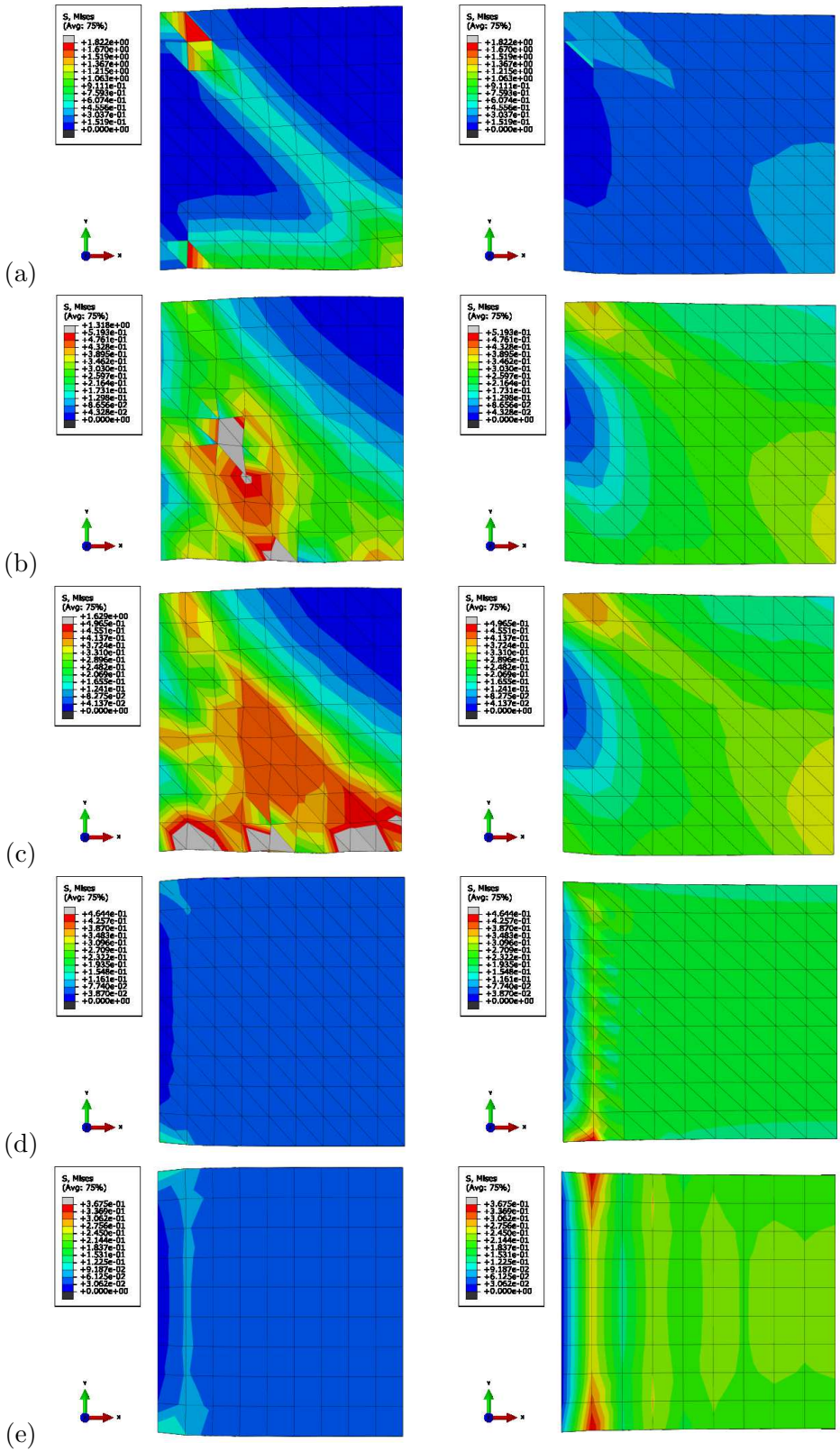

Figure 4.1: Stress contour plots on the finite element models under axial compression (left-hand-side images) and tension (right-hand-side images) with hyperelastic material properties. 1 (a), 2 (b) and 3 (c) layers of 6-node linear prismatic elements, 1 layer of 15-node (d), non-linear prismatic elements, and 1 layer of 8-node cubic elements (e). Further results can be found in Appendix C

provide a symmetric response to all loading conditions and this behaviour is reasonably matched by the quadratic/non-linear prismatic elements.

The full set of results from all four loading conditions can be found in Appendix C. The load-displacement responses of the four loading conditions follow similar collective trends (Figure 4.2). In Figure 4.2 the tensile loading condition of the hyperelastic models have been provided. This scenario was selected for closer examination as the ocular vessel, being of non-linear behaviour, will exhibit predominantly axial tensile forces under IOP. The linear prismatic elements behave in a stiffer manner to both the non-linear prismatic and cubic elements no matter how many layers are provided. The non-linear prismatic elements and cubic elements exhibit almost identical load-displacement responses. Referring back to Figure 4.1, these element types also present very similar stress distribution responses. The stiffer behaviour of the linear prismatic elements is in agreement with the literature which was discussed above.

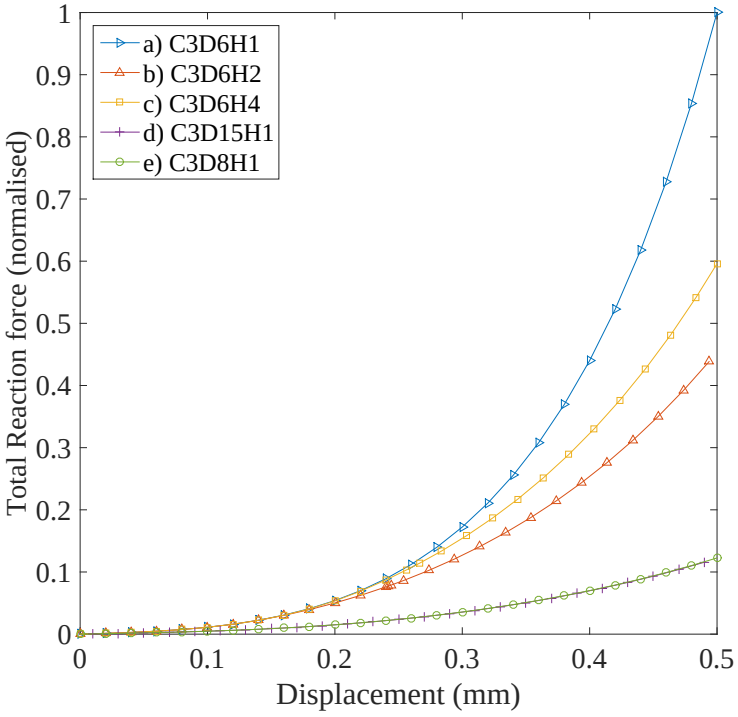

Figure 4.2: Load-displacement curves for the axial tension analysis of element types and configurations. The last last number in the legend plot references refers to the number of layers of elements, (a-e) relating to (a-e) in Figure 4.1

Based on this information non-linear prismatic elements were chosen for the modelling.

4.1.2 Characteristic Modelling

The topography, thickness and size of the human eye is tremendously varied. When numerical models are utilised to assess potential treatment options for degenerative ocular conditions, a broad spectrum of geometric characteristics can be utilised to represent population variations. This is in contrast to modelling an individual's ocular geometry, or geometry obtained from an *ex vivo* eye globe. A method is therefore required to generate characteristic models with suitable broad-spectrum variable controls.

When modelling human ocular globe characteristics a number for different variables are considered. These variables relate to characteristic descriptions of the ocular globe from previous studies such as (Aghaian et al., 2004; Chen et al., 2009; Doughty and Jonuscheit, 2007; Dubbelman et al., 2002; Hjortdal and Jensen, 1995; Jonuscheit et al., 2007), for further information see Chapter 1.

As previously discussed, bespoke software was developed for the task of generating characteristic models. With this software, the ocular characteristics of the model can be controlled by the:

1. central cornea thickness (CCT);
2. peripheral corneal thickness (PCT), therefore variation of corneal thickness across the surface;
3. central corneal radius;
4. corneal asphericity shape factor (p);
5. corneal diameter;
6. scleral radius;

7. variation of scleral thickness;

8. inclusion/exclusion, and geometry, of the:

   (a) ciliary muscle;

   (b) epithelium;

   (c) endothelium;

   (d) lamina cribrosa;

   (e) corneal layer separation.

9. and internal fluid cavity pressure.

The corneal asphericity was controlled by:

$$y^2 = 2rx - px^2 \tag{4.1}$$

where y is the semi-chord diameter and x is the sagittal depth. The apical radius (r) indicates the curvature with the shape factor (p) describing the asphericity of the profile (Baker, 1943). Cheung et al. (2000) summarised a number of earlier studies and reported mean shape factors which approximated the asphericity of the cornea. These ranged from $0.78 - 0.87$.

In addition to controlling the model geometry and the inclusion/exclusion of components of the ocular globe, the software was also developed to control the refinement and arrangement of mesh with the following variables:

1. number of corneal and scleral element rings;

2. and the number of element layers assigned to model the stroma.

An example of a characteristic model developed by this software is provided in Figure 4.3.

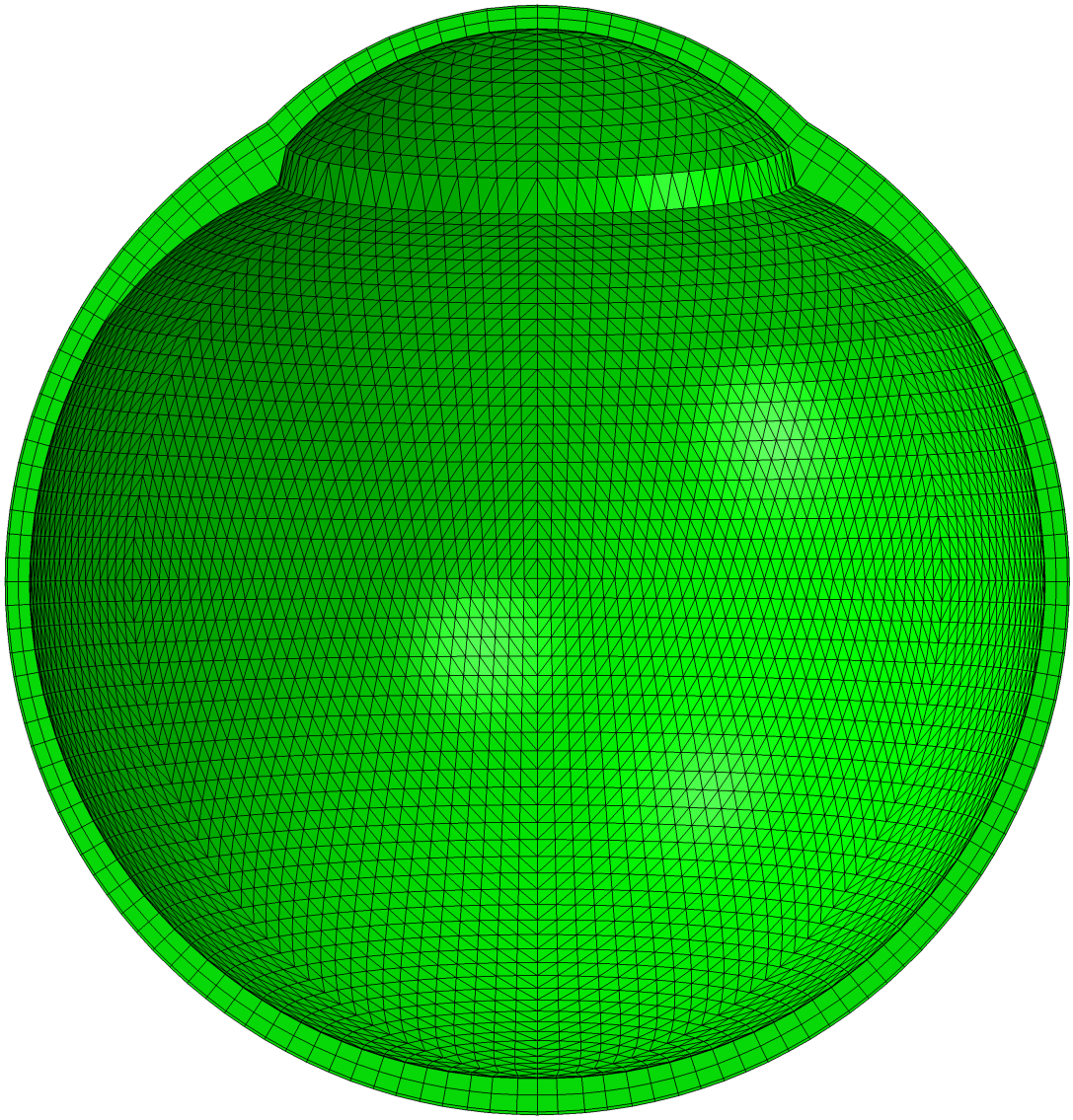

Figure 4.3: Example of a characteristic finite element of the human eye globe. The model has been sectioned to visualise the internal ocular space, the layer construction and the variation in thickness of the model. The model includes: variation in thickness of the cornea and sclera, non-spherical cornea, epithelium and endothelium layers, two stroma layers and the ciliary muscle.

The software was written in Visual Basic (Microsoft Corporation). A graphical user interface (GUI) was constructed to allow the use of the program without the need to understand or operate the underlining code. This was beneficial for future novice users of the program. It also provides speed, convenience of use, and secures the source code against corruption. The GUI is designed to be intuitive while also controlling the input to within acceptable bounds.
Figure 4.4 provides images of the GUI.

4.1.3 Specimen Specific Modelling

Specimen specific model geometry was achieved by stretching characteristic models to fit experimentally measured topographies. This was achieved by developing and testing bespoke software as part of this present study as described in Section 3.2.8.

4.1.4 Stress-Free Configuration

The following section has been published in an alternate form:
Elsheikh, A., **Whitford, C.**, Hamarashid, R., Kassem, W., Joda, A., Büchler, P., Feb. 2013. **Stress free configuration of the human eye**. Medical Engineering & Physics 35(2), 211-6

The 3D topography of the human eye can be measured *in vivo* with several devices such as the Pentacam® (Oculus Optikgeräte GmbH, Wetzlar, Germany), Gallilei® (Ziemer Ophthalmic Systems AG, Port, Switzerland) or Optical Coherence Tomography. *Ex vivo*, the topography can be measured by a number of additional methods including DIC as described in Section 3.2.6. In all cases topography is measured while the ocular vessel supports IOP. Therefore, the shape measured experimentally, or clinically, corresponds to a deformed configuration. This deformed configuration cannot be directly implemented into patient- or specimen-specific models as the application of IOP to this initial model geometry would alter the topography such that it no longer

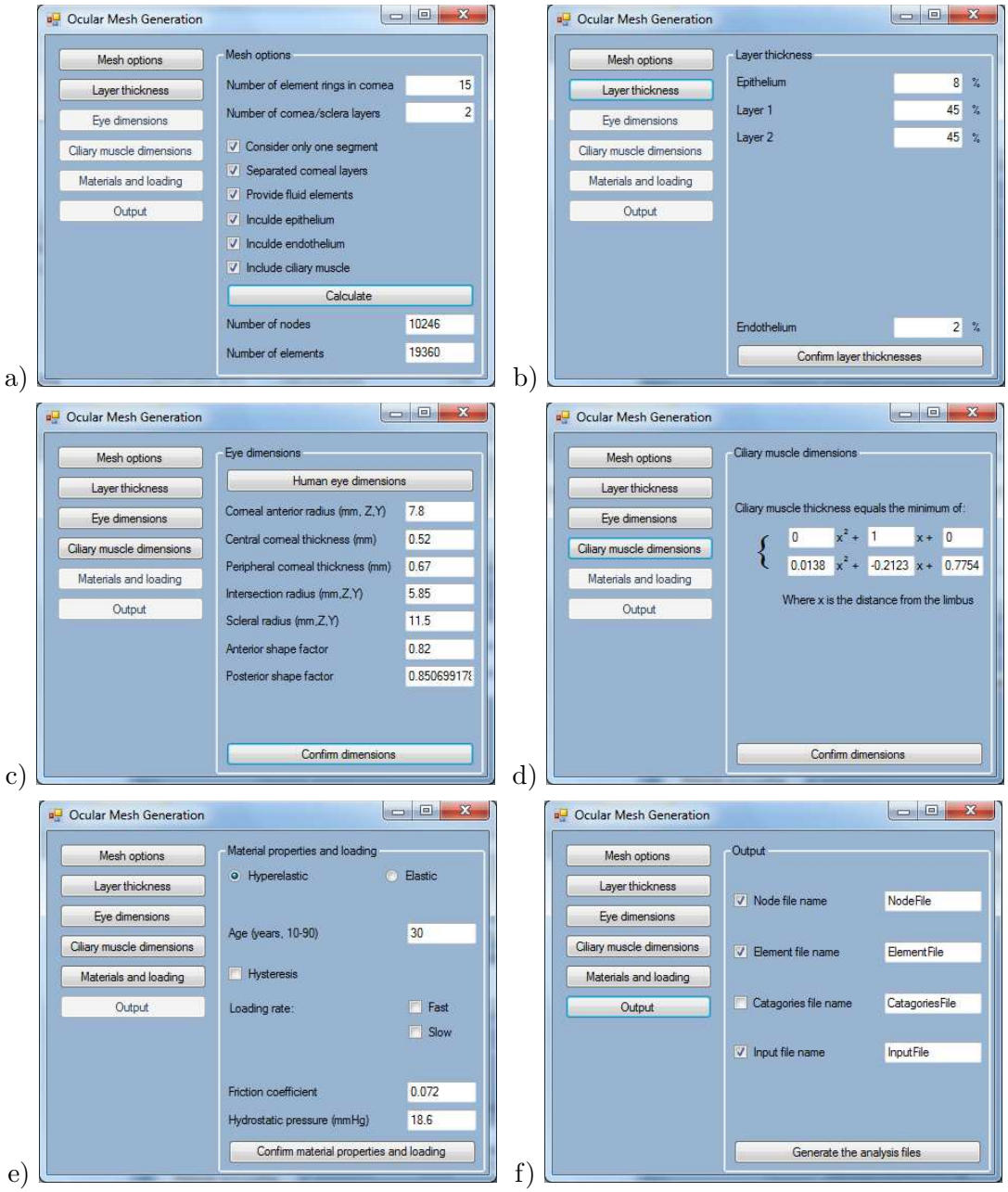

Figure 4.4: Graphical user interface developed to generate geometrically characteristic models of the human eye globe. The GUI pages include: (a) mesh options, (b) relative layer thickness control, (c) eye geometry, (d) ciliary muscle geometry, (e) simple material definitions and loading, and (f) output files for Abaqus solver.

matched the originally obtained topography. If, on the other hand, IOP was not applied the associated stresses and strains would not be generated in the model. Due to the hyperelastic and viscoelastic properties of the tissue the stress/strain-related stiffness of the model would not be representative of the eye in the configuration from which the topography was obtained. For these reasons it is necessary for accurate numerical modelling to determine the stress-free configuration of the eye, such that the initial configuration of the model represents the geometry of the eye, the IOP having been removed.

Two main techniques have been investigated to solve this problem: (1) *inverse elastostatic* approach, (2) a modified updated Lagrangian formulation. Govindjee and Mihalic (1998); Lu et al. (2007) utilised the inverse elastostatic approach by the negative application of IOP to explicitly estimate the stress-free configuration. This was followed by the positive application of IOP on the estimated stress-free form to determine the resulting stresses in the deformed configuration. Grytz and Downs (2012) identified a major limitation of this approach, that the thin-walled flexible ocular structure may exhibit bifurcation during the backward calculation of the zero pressure geometry. To solve this problem Gee et al. (2010) proposed a modified updated Lagrangian formulation to estimate the stress in aorta tissue by forward calculation. This approach attempts to avoid the need to determine the stress-free configuration. Lanchares et al. (2008) adopted a similar technique to pre-stress a cornea model. This approach was latter refined by Grytz and Downs (2012).

Although these methods have been shown to provide accurate results, their implementations remain complicated. Pandolfi and Holzapfel (2008) proposed an alternative approach where general-purpose finite element software packages are combined with simple mathematical calculations to obtain stress-free configurations. This method was implemented into this present study and assessed to determine if it provided a sufficient level of accuracy.

Methods

The method used in this study is based on the simulation of ocular deformation with finite element techniques. An iterative approach is used to gradually move the nodes of the finite element mesh to their stress-free configuration. This is graphically represented in Figure 4.5.

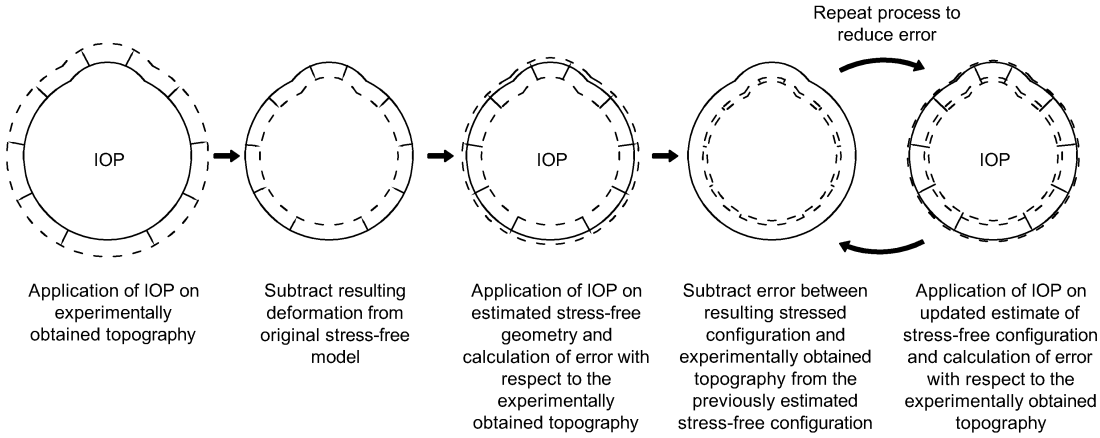

Figure 4.5: Diagram illustrating the flow of the method used to determine the stress-free configuration of models.

The iterative approach begins with the clinically, or experimentally, measured stressed topography X_0. The first stage applies IOP in a non-linear finite element analysis which generates displacements u_1 and a deformed topography x_0, Figure 4.5.(a).

$$u_1 = X_0 - x_0 \tag{4.2}$$

These displacements vectors were then subtracted from the original geometry X_0 to determine a first estimate of the stress-free configuration X_1, Figure 4.5.(b).

$$X_1 = X_0 - u_1 \tag{4.3}$$

In the next phase of the process, the model first estimate of stress-free configuration was again stressed under IOP to generate deformed topography x_1, Figure 4.5.(c). The error vector u_2 between x_1 and X_0 is calculated.

$$u_2 = X_0 - x_1 \tag{4.4}$$

The error vector u_2 was then subtracted from the nodal geometry of the previous estimate of the stress-free configuration x_1 to define an updated estimate of the stress-free configuration X_2, Figure 4.5.(d)

$$X_2 = X_1 - u_2 \tag{4.5}$$

This iteration was again stressed under IOP, Figure 4.5.(e) and a new error vector u_k was obtained.

$$u_k = X_0 - x_{k-1} \tag{4.6}$$

$$X_k = X_{k-1} - u_k \tag{4.7}$$

Stages (d & e) were repeated in an iterative procedure as per Equations 4.6 & 4.7 and Figure 4.5.(d & e). The absolute nodal distance and the RMS distance ($L^2 - norm$) were used to quantify the maximum and average error and the monitor the convergence of the iterative procedure toward the stress-free configuration. The error estimate of the k^{th} increment was given by:

$$e_k = ||X_0 - x_k|| \tag{4.8}$$

Trials were initially conducted on the same ocular model used to assess the effect of gelatin support conditions in Section 3.2.4. In this study the mean error was calculated to be $< 10^{-7}$ mm and the maximum error was $< 10^{-6}$ mm after 6 iterations.

This section of the present study was extended by other members of the research group where a parametric study was conducted and demonstrated reliance of the error level

on the level of flexibility of the eye model, especially in the cornea region. However, in all cases, $3-4$ analysis iterations were considered sufficient to produce a stress-free form with average errors in node location $< 10^{-6}$ mm and a maximal error $< 10^{-4}$ mm. This error level was similar to what has been achieved with other methods and orders of magnitude lower than the accuracy of current clinical topography systems. This therefore justified the use of the technique as a pre-processing step in ocular numerical simulations (Elsheikh et al., 2013).

4.1.5 Integration Point Descriptors

Sections 4.3.3 and 4.3.4 present two new constitutive models representing different material behaviours of interest. Both models provide anisotropic representation which is based on both local and global coordinate systems (further details are provided in Section 4.3.3).

The orientation of the local coordinate system is provided, in part, in the form of a vector normal to the tangential plane of each integration point within the model. The section of the numerical model which utilises this information runs once for every integration point within the model ($10^4 - 10^6$ times during a typical finite element analysis procedure). It is therefore vital that this transfer of information to the numerical model is extremely efficient. For this reason the normal vector is written into binary form which is read by the numerical model (see Section 4.1.6 for further details). To provide this binary file, bespoke software has been developed as part of this study, which is able to analyse any ocular model (part or whole, characteristic or specimen specific) and compute and write a binary file containing the correct data.

Additionally, it has been determined that through-thickness depth dependant variation of material behaviour will be investigated in future research[1]. Therefore, the bespoke software introduced above was expanded to analyse these finite element models and

[1] At the stage of development of the two constitutive models within this study appropriate depth dependant microstructure was not available.

write the through-thickness depth of each integration point in binary format.

4.1.6 FORTRAN Subroutines within Finite Element Analysis

The Abaqus finite element solver includes numerous precoded subroutines which allow the user to include model definitions such as: geometry, loading, material definitions and boundary conditions. Typically the user is detached from the subroutines. If models are developed through CAE then the required subroutines are selected by the detached implementation of model definitions either graphically or by parameter selection. Variables supplied to the relevant subroutines are provided in similar fashions. If models are generated by directly coded input files (*.inp) then subroutines are selected by *keywords* and the relevant variables are defined numerically (Abaqus, 2013a). Abaqus also permits the user to define additional subroutines. Within Abaqus Standard there are 55 available blank subroutines. These are defined by their input/output (I/O) and the position within the FEA at which they are called. This research has utilised 3 of these available subroutines: SDVINI, UMAT and DLOAD.

SDVINI

SDVINI, which refers to *state variable initial conditions*, is a subroutine applied to each integration point of the model (nine per C3D15H element) prior to the first iteration of the first step in the finite element method calculation. During this subroutine it is possible to define initial variables for each point (STATEV, *solution-dependent state variables*). These variables are subsequently accessible from a selection of other subroutines (including UMAT). This subroutine was used in this study to define the initial location based parameters within the model.

UMAT

UMAT, which refers to *user defined material*, is used in this present study:

1. to define the mechanical constitutive behaviour of the stromal tissue;
2. where it was called at all material integration points of elements;
3. utilising solution-dependent state variables defined in SDVINI;
4. to update the stresses and solution-dependent state variables to their values at the end of each increment;
5. to provide the material Jacobian matrix, $\partial\Delta\sigma/\partial\Delta\epsilon$, for the mechanical constitutive model.

Abaqus (2013c) warns the user that this subroutine *'generally requires considerable expertise. You are cautioned that the implementation of any realistic constitutive model requires extensive development and testing'.*

DLOAD

DLOAD, *distributed surface load* is used to define the pressure distribution profile of the Corvis® ST non-contact tonometer (Oculus Optikgeräte GmbH, Wetzlar, Germany) used in Section 4.3.3. Without utilising this subroutine, surfaces would be defined on the model and typically the load profile would be symmetrical, and discretely, distributed across rings of element groups. The adoption of this subroutine allowed the non-symmetrical distribution of the pressure profile, P, which was discretised across the surface by individual integration points by:

$$P = 0.5\cos(0.955r) + 0.5 \tag{4.9}$$

which was provided by OCULAS®, where the radius, r, was off-centred by:

$$r = \sqrt{(x - 0.2)^2 + y^2} \tag{4.10}$$

to match clinically obtained data (see Section 4.3.3 for further details), where (x, y) are the coordinates of individual integration points.

4.2 Inverse Analysis

Inverse analysis[2] is based on the commonly used finite element analysis but with a significant difference. Traditionally, finite element analysis utilises known inputs of geometry, loading, boundary conditions and material properties to output structural deformations and stresses. In contrast, inverse analysis has input values which include the geometry, loading, boundary conditions and deformations with the output being the material properties. The method is essentially a sophisticated trial-and-error process that requires testing material defining parameters within predefined boundaries and assessing the match between the predicted and measured deformations. This assessment is performed through an objective function which can be: linear, quadratic, sum-of-squares (least squares), smooth non-linear, or non-smooth.

Methods described in this section were utilised for a separate study:
Yu J., Bao F., Feng Y., **Whitford C.**, Ye T., Huang Y., Wang Q., Elsheikh A., **Assessment of Corneal Biomechanical Behavior Under Posterior and Anterior Pressure**., January 2013, Journal of Refractive Surgery

Inverse analysis utilises optimisation software which is either available commercially or programmed for purpose. Within this software the direction of the trial-and-error is controlled by any number of various algorithms such as: Particle Swarm Optimisation (PSO); Genetic Algorithm (GA), which is used, for example, in Excel Solver (Microsoft Office 2014, Microsoft Corporation); Simulated Annealing (SA), also stochastic, is an algorithm unlikely to find the global optimum but is useful with large and noisy solution spaces; Non-Linear Sequential Quadratic Programming (NLSQP); Levenberg-Marquardt (LM); Response Surface Method (RSM) and many others. All algorithms are limited by two significant factors: (1) the given solution space; (2) their ability to find a unique solution within the solution space. The latter is often referred to as the robustness of the solution and is a significant problem with basic algorithms. A common

[2]Inverse analysis is also referred to as inverse modelling or reverse analysis.

technique to overcome this problem is to utilise stochastic optimisation which provides random sampling throughout the solution space such as Monto Carlo sampling (Kroese et al., 2014). However, this will still not always achieve a unique solution. Considering, for example, a problem with ten variables, each variable requires simultaneous fitting to achieve a target, where the boundaries are large and a reasonably high resolution is required; each variable may require 1001 potential values; resulting in a solution space with a size $1001^{10} \approx 10^{30}$. Without trialling every possible solution, the uniqueness of the solution is reliant on the algorithms. If solution spaces are this large it is simply not possible to achieve complete uniqueness with any algorithm. In addition, the optimisation is based on a numerical objective function which is a purely quantitative assessment. It is therefore required that the output of inverse analysis is assessed for quality and its suitability to the problem. It should also be considered that the fields of both physics and engineering adopt mathematical techniques to describe the enormous complexity of the world around us. Unlike the field of pure mathematics, the question is not whether the model is as accurate as could possibly be achieved, the question is whether the model is accurate enough to represent that aspect of the world around us for the purpose the model was designed. With this consideration in mind, and the knowledge of the natural variation in tissue response, we consider an quantitative error $< 5\%$ (Yu et al., 2013) to be acceptable and the qualitative assessment of the fit is usually a consideration of the models ability to represent the non-linear behaviour of the tissue.

The adoption of inverse analysis for complex problems, such as those presented in this study, requires the development of skill. Great care was required to understand the effects of choices in boundaries, and initial estimates, of variables and the abilities of the tools adopted for the procedures.

4.3 Material Representation

4.3.1 Continuum Mechanics

Continuum mechanics is the basis for non-linear continuum mechanics theory which is adopted in this present study. Continuum mechanics is based on the hypothesis that matter is continuously, but not necessarily homogeneously, distributed throughout the volume occupied by the matter. Irgens (2008) describes the hypothesis as how we directly experience matter and its macroscopic properties. However, we divert from that philosophy by modelling microscopic effects. Further details on the continuum mechanics theory can be found in Irgens (2008) amongst many other texts.

In relation to the present study the adoption of the continuum mechanics theory leads to two important approximations: (1) the fibrils, other biomolecules and the voids between them, which contribute to the mechanical response of the stroma are not discretely modelled, and (2) the form of the material does not alter. The effects of approximation (1) was investigated by Studer (2011) where a close match between discrete and continuum fibril modelling results where found. Given the large complexities with discrete modelling, the continuum approach is adopted in this present study. The approximation of (2) has implications where non-physiological loading is applied to the simulation. This was discussed further in Chapter 1.

4.3.2 Procedure for Formulating a New Constitutive Model

There are five basic steps required to formulate a new constitutive relation within continuum mechanics (as described by Humphrey (2003)):

1. delineation of general characteristics;

2. establishing an appropriate theoretical framework for quantification;

3. identification of specific functional forms of the constitutive relations;

4. calculation of the values of the associated material parameters;

5. evaluation of the predictive capability of the final relation.

. These steps are followed in the development of these two constitutive models.

4.3.3 Biomechanical Model of the Human Cornea: Considering Shear Stiffness and Regional Variation of Collagen Anisotropy and Density

The transparent cornea is a most important component of the outer ocular tunic. It provides a tough protective envelope for the ocular contents and helps give the eye its general shape. The shape of the cornea accounts for more than two-thirds of the optical power of the eye (Fatt, 1978). This important role is a function of the corneal curvature, regularity, clarity and refractive index. The corneas contribution to ocular image formation can be degraded by anomalies in shape produced by disease, injury or surgery, and therefore the ability to understand and predict corneal response to such conditions is of great clinical importance (Roberts, 2000; Ethier et al., 2004).

There is also significantly more data describing the micro-structural arrangement in the cornea. For these reasons, the following two sections concentrates on the advance in numerical representation of the cornea.

The following section has been published in a similar form in:

Whitford C., Studer H., Boote K., Meek K.M. & Elsheikh A., **Biomechanical Model of the Human Cornea: Considering Shear Stiffness and Regional Variation of Collagen Anisotropy and Density**, Feb 2015, Journal of the Mechanical Behavior of Biomedical Materials, 42, 76-87

Presented in this thesis is a continuum based finite element model of the 3D corneal

structure. Characteristic biomechanical properties are provided as a function of age to reflect the age-related stiffening from $30-100$ years-of-age. Numerical simulations represent an experimental data set of 12 donor corneas tested in shear (Elsheikh et al., 2009); 109 corneas tested under inflation conditions (Elsheikh et al., 2007a, 2010b); while adopting the anisotropic and density variation obtained through WAXS analysis of 3 corneas. Simulation of corneal deformation resulting from the Corvis® ST highlights shear strain above 0.25. Numerical representation of experimentally defined shear stiffness is provided beyond this value. By adopting the methods introduced in this thesis the aim was to further advance the accurate representation the corneal stromas biomechanical response to internal and external forces.

The model presented introduces a function that describes the regional stiffness variation relating to the known variation of total collagen fibril density. The addition of this function provides increased representation which is particularly apparent in the limbal area, where the known increase in fibril density contributes to the annular stiffness.

Methods and Materials

The non-linear, anisotropic and incompressible material behaviour of the corneal stroma can be numerically represented using a strain energy density function:

$$\psi = \psi\left[\mathbf{C}, \mathbf{A}, \mathbf{B}\right], \tag{4.11}$$

where $\mathbf{C}$ is the right Cauchy-Green deformation tensor calculated from the deformation gradient, $\mathbf{F}$ as $\mathbf{C} = \mathbf{F}^T\mathbf{F}$ is a second order tensor representing the gradient of the mapping function which relates the current configuration of a continuum to its reference configuration. $\mathbf{A} = \mathbf{a} \otimes \mathbf{a}$ and $\mathbf{B} = \mathbf{b} \otimes \mathbf{b}$ are anisotropic tensors, based on vectors and which define single discretised directions of anisotropy. Similar to a procedure presented earlier (Studer et al., 2010)), an isochoric split is performed on the energy density function to separate the responses to a volume-changing dilation and a volume-

preserving distortion:

$$\psi = U\left[J\right] + \bar{\psi}\left[\bar{\mathbf{C}}, \mathbf{A}, \mathbf{B}\right], \tag{4.12}$$

where $\bar{\mathbf{C}}$ is the distortion component of the right Cauchy-Green deformation tensor defined from $\mathbf{C} = \left(J^{2/3}\mathbf{I}\right)\bar{\mathbf{C}} = J^{2/3}\bar{\mathbf{C}}$ where $\mathbf{I}$ represents the unit tensor, $J = \det\left(\bar{\mathbf{F}}\right)$, $\mathbf{F} = \left(J^{1/3}\mathbf{I}\right)\bar{\mathbf{F}}$ and $\bar{\mathbf{F}}$ defines the deformation gradient associated with distortion. Further explanation of these concepts is provided by Holzapfel (2000) and others. In order to provide a separate representation of the matrix and fibrils contributions to mechanical behaviour, a second split of the strain energy function is performed:

$$\psi = U\left[J\right] + \bar{\psi}_m\left[\bar{\mathbf{C}}\right] + \bar{\psi}_f\left[\bar{\mathbf{C}}, \mathbf{A}, \mathbf{B}\right], \tag{4.13}$$

As in Studer et al. (2010), the dilation constituent, $U[J]$, from Equation 4.13 is given by:

$$U\left[J\right] = \frac{1}{D}\left(J-1\right)^2, \tag{4.14}$$

where D is the material coefficient describing volume change. Also in the neo-Hookean formulation, the constituent equation to represent the matrix stiffness is given by:

$$\bar{\psi}_m\left[\bar{I}_1\right] = C_{10}\left(\bar{I}_1 - 3\right), \tag{4.15}$$

where the distortion component of the right Cauchy-Green deformation tensor, $\bar{\mathbf{C}}$, was replaced by its first strain invariant; $\bar{I}_1 = tr\bar{\mathbf{C}}$, and C_{10} is a material constant.

Since in this equation $\mathbf{A}$ and $\mathbf{B}$ are a second order tensors and each can only represent a single direction of anisotropy, an adaptation is required to enable consideration of a multi-directional fibril orientation. Pinsky et al. (2005) presented a numerical method to describe the angular distribution of collagen fibrils in the corneal and limbal stroma obtained from WAXS studies (Aghamohammadzadeh et al., 2004). This method was later modified by Studer et al. (2010). The coordinate system adopted is presented in Figure 4.6. To accurately translate 2D data to the 3D model a polar coordinate system is adopted. In this system a relationship between the normalised distance to

the limbus (2D WAXS data) and the radius normalised to the limbus, $R_{G,norm}$, (3D model) has been developed. Here $R_{G,norm} = R_G / \ R_{limbus}$, where subscript G denotes global coordinates with reference to the global system. Normalising the system allows comparative analysis between corneas of different sizes.

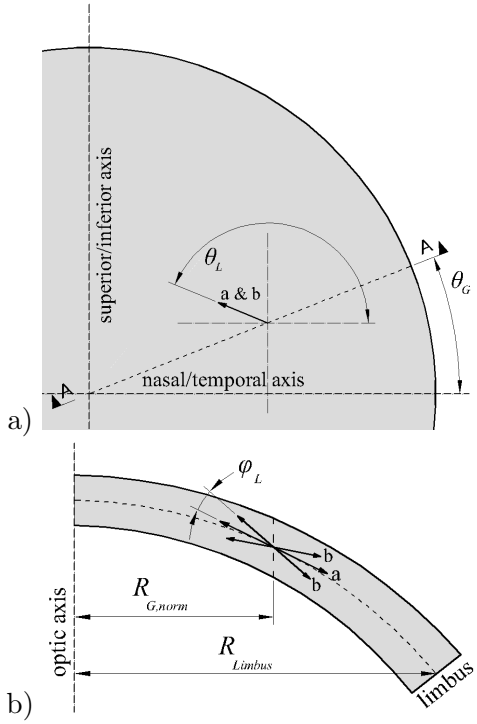

Figure 4.6: Coordinate systems used to describe a discrete location within the stroma model: (a) anterior view of the cornea. Global and local azimuthal angles of the systems are based on an orthogonal system. Note, the vectors **a** and **b** share values in this orientation; (b) section view A-A. Radius and local polar angle of the polar and spherical systems respectively. Note, vector **a** in aligned to the tangent plan, while vector **b** is both inclined and declined from the tangent plane by φ_L.

To accommodate the known regional variation of fibril arrangement the fibril constituent of Equation 4.13 was modified to enable representation of multiple directions within this system. The second order tensor **A** was utilised to describe the lamellae fibrils aligned to the tangent plane, while tensor **B** is utilised to represent the ILC fibrils. This was written in the term:

$$\bar{\psi}_f = \ \zeta \frac{1}{\pi} \int_0^{\pi} \chi \Big(\bar{\psi}_{f,lamellae} \left[\overline{\mathbf{C}}, \mathbf{A} \right] + \bar{\psi}_{f,ILC} \left[\overline{\mathbf{C}}, \mathbf{B} \right] \Big) d\theta_L, \tag{4.16}$$

where $\theta_L \in [0, \pi]$ is the azimuthal angle of the spherical system; and subscript L denotes the local attributes defined on the tangent plane for each discrete location in the local coordinate system, as represented in Figure 4.6. ILC fibrils were represented by tensors arranged at 15° anterior and posterior to the tangent plane. This inclination/declination follows Studer et al. (2010) where the angle of the ILC was derived from experimental observations. The local density function, χ, defines the anisotropic distribution of the fibrils. This is defined as a linear combination of χ_1, depicting central, orthogonal fibrils and χ_2, denoting peripheral, circumferential fibrils as:

$$\chi\left(R_{G,norm}, \theta_G; \theta_L\right) = w_1 \chi_1 + \left(1 - w_1\right) \chi_2, \tag{4.17}$$

where

$$\begin{aligned} \chi_1\left(\theta_G; \theta_L\right) &= \cos\left(\theta_L\right)^{2n} + \sin\left(\theta_L\right)^{2n} + c_1, \\ \chi_2\left(\theta_G; \theta_L\right) &= \sin\left(\theta_L + \theta_G\right)^{2n} + c_2, \end{aligned} \tag{4.18}$$

and

$$w_1\left(R_{G,norm}\right) = \begin{cases} 1 & \text{if } R_{G,norm} < 0.638 \\ b & \text{if } R_{G,norm} < 0.940 \\ 0 & \text{else} \end{cases}, \tag{4.19}$$

where

$$b = 0.5\left(\cos\left(3.5\pi\left(R_{G,norm} + 0.51\right)\right) + 1\right), \tag{4.20}$$

where the boundary values are obtained from Studer et al. (2010) and Pinsky et al. (2005) as absolute measurements (4mm and 5.5 mm). These were normalised by the assumed corneal diameter of 5.85 mm. Values $n = 4$, $c_1 = 0.45$ and $c_2 = 0.72$ were also obtained from these two articles. The global density function, ζ was introduced in Equation 4.16 to represent rotational variation of collagen density. ζ was based on the full-thickness, fibril density measurements obtained using WAXS for three specimens (Figure 4.7). Consideration of thickness values allowed conversion of the density maps to distributions of fibril content per unit thickness, which allowed the derivation of ζ. Thickness values where assumed to be rotationally symmetric; central corneal thickness

(CCT) of 545 μm was used as the average value reported from a number of previous studies (Francis et al., 2007). Peripheral corneal thickness (PCT) was 150 μm greater than the CCT, consistent with Gullstrands No1 schematic eye (Bennet and Rabbetts, 1989). PCT was modified to obtain the thickness parallel to the optic axis (809 μm) by obtaining the stress free configuration 4.1.4 of the characteristic cornea, as WAXS was obtained from unloaded, curved cornea in this axis. This data was provided in the form

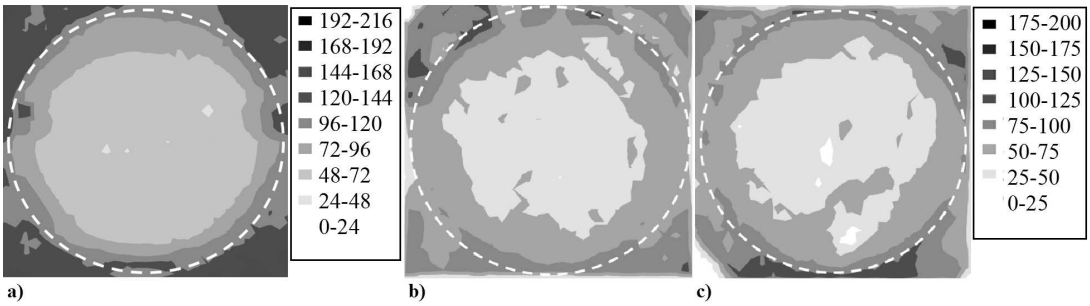

Figure 4.7: Total WAXS from collagen fibril content obtained from three specimens (reproduced with permission the publisher of Inv. Ophth. & Vis. Sci.). Specimens (a) and (b) are RE, while c) is a LE. (b) and (c) share the same scale and are from the same donor. All scales are in arbitrary units, and therefore the density values should only be used for comparative purposes. The limbus is defined in all specimens by a dashed white line.

of discrete data point on a Cartesian grid. The discrete data points from experimental analysis and the proposed numerical relationships are presented in Figure 4.8 & 4.9.

Data from specimen (c), Figure 4.7, was obtained from a left-eye (LE). To compare this specimen with the remaining two corneas, the data was flipped about the superior-inferior axis, thus presenting nasal LE with nasal right-eye (RE) and preserving the potential of asymmetry of density about the body's S-I axis, Figure 4.9. An analytical relationship was derived to represent the fibril density based on this examination of the data. ζ is defined as a non-linear combination of ζ_1 the central, distribution, and ζ_2 the peripheral distribution as:

$$\zeta\left(R_{G,norm};\theta_G\right) = w_1\zeta_1 + \left(1 - w_1\right)\zeta_2; \tag{4.21}$$

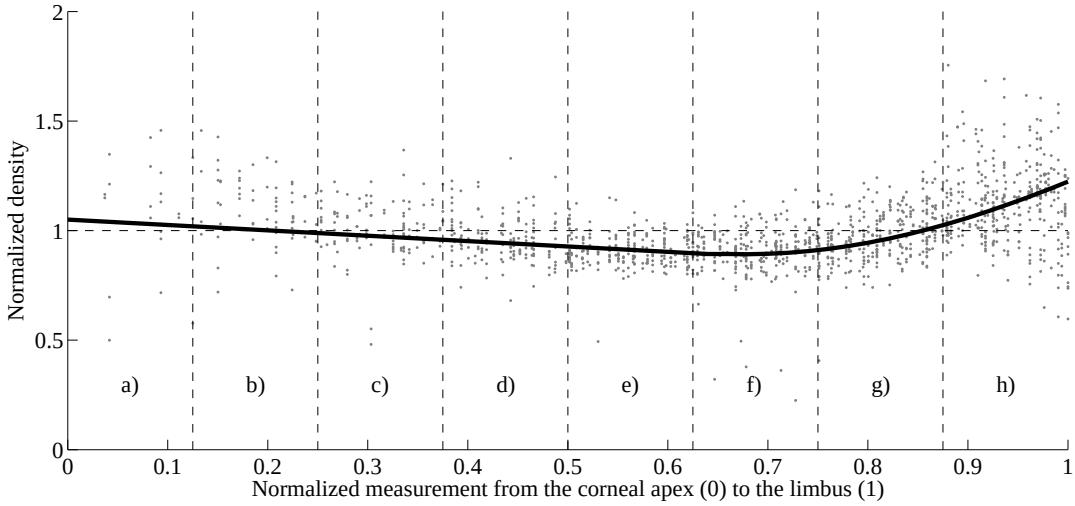

Figure 4.8: Normalised distribution of fibril density in the human cornea. Values have been normalised such that the average density value is 1 for all 3 specimens considered. Grey dots depict discrete experimental data points for all three specimens and the black line is the numerical representation of the rotationally averaged experimental data, η.

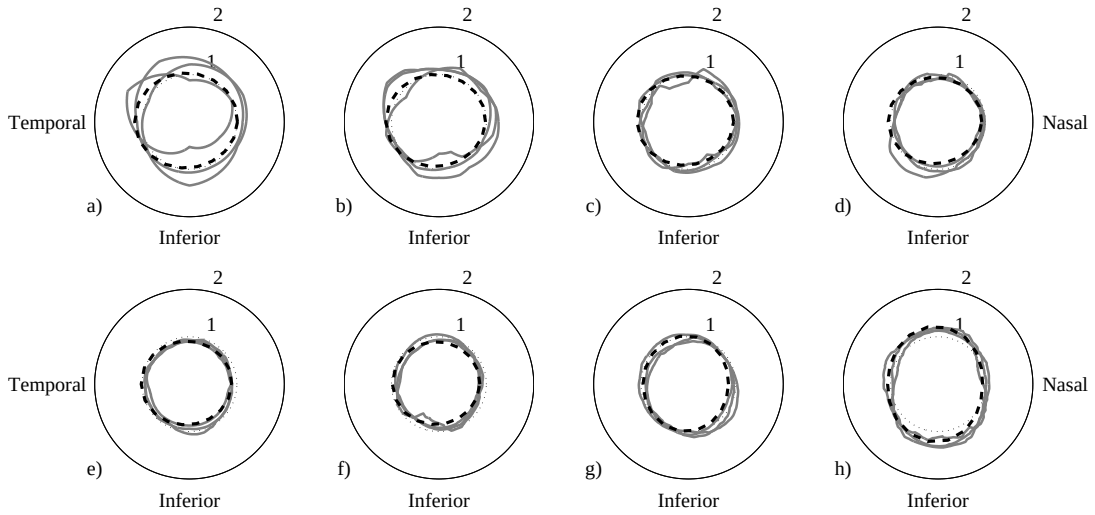

Figure 4.9: Total fibril density separated into eight circumferential banded regions from the corneal apex (a) to the corneal limbus (h). The polar plots present the normalized density measurements against their angular location. The scale of the polar plots range 0-2 where 1 equals the mean density. Grey lines are the circumferentially moving average for the each of the three specimens and the dashed black line is the non-rotationally symmetric numerical representation, ζ.

where ζ_1 and ζ_2 are

$$\begin{aligned}\zeta_1\left(R_{G,norm};\theta_G\right) =& p_1\sin^2\left(\theta_G+p_2\right)\eta+p_3\sin^2\left(\theta_G/2+p_4\right)\eta+p_5\eta,\\ \zeta_2\left(R_{G,norm};\theta_G\right) =& p_6\sin^2\left(\theta_G+p_7\right)\eta+p_8\sin^2\left(\theta_G/2+p_9\right)\eta+p_{10}\eta;\end{aligned} \tag{4.22}$$

and the rotationally symmetric density, η, is defined by

$$\eta\left(R_{G,norm};\theta_G\right)=\begin{cases}c & \text{if } R_{G,norm}<0.65\\ d & \text{else}\end{cases}, \tag{4.23}$$

where

$$\begin{aligned}c &= p_{11}-R_{G,norm}p_{12}\\ d &= -p_{13}\sin\left(p_{14}R_{G,norm}+p_{15}\right)+p_{16}\end{aligned}. \tag{4.24}$$

These initial, analytical, descriptions of the data were derived to provide sufficient flexibility within them to represent observed variation in the density between the central cornea and the limbus, and the non-rotationally symmetric distribution of density. Numerical constants $p_{1,2....16}$ were obtained through an optimisation process to reduce the RMS error between all, discrete, experimental data points and their numerical representation, such that $\mathrm{RMS}(Exp,\zeta)=0.130$. This optimisation process was performed using bespoke software to compare the numerical and experiment, and the SHERPA algorithm within the design optimisation software package HEEDS (Red Cedar Technology, Michigan, USA). This algorithm incorporates Monte Carlo sampling which ensured the analysis did not stop at local minima and that the resulting values of $p_{1,2....16}$ were unique and robust. In addition to the minimisation of the RMS error the condition was set that the mean of the numerical representation of density equals 1. The resulting parameters of this process are presented in Table 4.1.

Figure 4.10 provides the errors calculated for each discrete measurement of the experimental data.

The lamellae and ILC fibril contributions to the constituent equation where based on

Table 4.1: Numerical parameters derived for the density function (Equation 4.21)

Parameter	p_1	p_2	p_3	p_4	p_5	p_6	p_7	p_8
Value	0.08	4.68	0.15	0.21	0.89	0.20	0.02	0.11
Parameter	p_9	p_{10}	p_{11}	p_{12}	p_{13}	p_{14}	p_{15}	p_{16}
Value	3.16	0.84	1.05	0.25	0.65	3.26	5.65	1.55

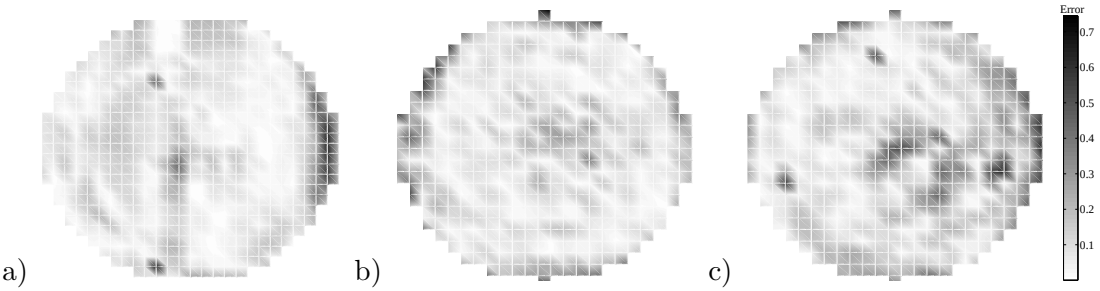

Figure 4.10: Errors between the normalized experimentally obtained fibril density and the numerical representation of density, η. Errors are presented for each of the 3 cornea as per Figure 4.7

the polynomial Ogden law, modified by Markert et al. (2005) to include one direction of anisotropy. They were therefore rewritten as:

$$\begin{aligned} \bar{\psi}_{f,lamellae}\left[\bar{I}_4\right] &= \frac{\mu_1}{\gamma_1}\left(\bar{I}_4^{\frac{\gamma_1}{2}} - 1\right) - \mu_1 \ln \bar{I}_4^{\frac{1}{2}}, \\ \bar{\psi}_{f,ILC}\left[\bar{I}_6\right] &= \frac{\mu_2}{\gamma_2}\left(\bar{I}_6^{\frac{\gamma_2}{2}} - 1\right) - \mu_2 \ln \bar{I}_6^{\frac{1}{2}}, \end{aligned} \tag{4.25}$$

where $\bar{\mathbf{C}}$, $\mathbf{A}$ and $\mathbf{B}$ in Equation 4.13 are replaced by the invariants $\bar{I}_4 = \bar{\mathbf{C}} : (\mathbf{a} \otimes \mathbf{a})$, $\bar{I}_6 = \bar{\mathbf{C}} : (\mathbf{b} \otimes \mathbf{b})$ and material parameters μ (polynomial coefficient relating to stiffness) and γ (governing non-linearity relating to hyperelasticity).

The condition where the fibril constituent of Equation 4.13 is only activated where stretch, $\lambda_{4,6} = I_{4,6}^{\frac{1}{2}} > 1$, is applied as it is considered that only the matrix carries compressive forces.

The strain energy density function is therefore written from Equation 4.11 in the form:

$$\begin{aligned}\psi =& \frac{1}{D}\left(J-1\right)^2 \\ &+ C_{10}\left(\bar{I}_1 - 3\right) \\ &+ \zeta \frac{1}{\pi}\int_0^{\pi} \chi\Bigg(\left(\frac{\mu_1}{\gamma_1}\left(\bar{I}_4^{\frac{\gamma_1}{2}} - 1\right) - \mu_1 \ln \bar{I}_4^{\frac{1}{2}}\right) \\ &\qquad + \left(\frac{\mu_2}{\gamma_2}\left(\bar{I}_6^{\frac{\gamma_2}{2}} - 1\right) - \mu_2 \ln \bar{I}_6^{\frac{1}{2}}\right)\Bigg) d\theta_L\end{aligned} \tag{4.26}$$

Implementation of Numerical Simulation

Numerical simulations have been conducted using finite element analysis (FEA). Geometric modelling was performed using bespoke software that provides geometry, which can be imported into finite element solvers as an orphan mesh. Finite element solver Abaqus/Standard 6.13 (Dassault Systmes Simulia Corp., Rhode Island, USA) was used. Abaqus is well known for its ability to analyse non-linear problems. However, its ability to provide state-of-the-art representation of biological material properties, and both regional and local variation of these properties, is limited. Thus, Abaqus was used in conjunction with bespoke subroutines (SDVINI & UMAT) written in FORTRAN to implement the constitutive model described above.

The integral of Equation 4.26 was discretised into steps of one degree by $\frac{1}{\pi}\int_0^{\pi} d\theta_L \rightarrow \frac{1}{180}\sum_{i=1}^{180}\theta_{L,i}$, where $\theta_{L,i}$ defines the orientation of the one hundred and eighty directions of anisotropy per integration point within the model. The fibril constituent of the model only provided tensile stiffness and was applied for each element in each discretised direction of anisotropy.

Subroutine SDVINI was used to provide initial, reference-configuration and location-based conditions such as fibril density representation. These location-based properties are defined individually for each integration point.

The approach described by Weiss et al. (Weiss et al. 1996) is used to define these material law definitions in terms of the 2nd Piola-Kirchhoff stress, **S** and stiffness, **D**

tensors :

$$\mathbf{S} = \quad 2\frac{\partial \psi}{\partial \mathbf{C}} = 2\sum_{a=1}^{4} \frac{\partial \psi}{\partial I_a}\frac{\partial I_a}{\partial \mathbf{C}}, \tag{4.27}$$

$$\mathbf{D} = \quad 2\frac{\partial \mathbf{S}}{\partial \mathbf{C}} = 2\sum_{a=1}^{4} \frac{\partial \mathbf{S}}{\partial I_a}\frac{\partial I_a}{\partial \mathbf{C}}. \tag{4.28}$$

These are implemented into the numerical simulation using the UMAT subroutine with stiffness represented as the components of the Jacobian as demonstrated in the Abaqus User Subroutines Reference Guide (Abaqus, 2013c). UMAT is also used to define current-configuration properties such as anisotropy.

Models were generated using fifteen-node, solid, hybrid, quadratic, elements (Abaqus, C3D15H). Elements were arranged in three layers and in twenty six rings. The shape of element, and their arrangement, was chosen to provide uniform element sizes and consistent approximation of geometry. The near-incompressibility of the corneal stroma is represented by hybrid elements which provide volume controls within the solver (Abaqus Theory Manual), and the constant D (Equation 4.14) was set to the low value of 10^{-5}, indicating close to incompressible behaviour. Similar to Pandolfi and Holzapfel (2008) the remaining dilation term of Equation 4.26 becomes purely mathematically motivated. Quadratic elements were used for two reasons. Firstly, it was found that quadratic elements exhibit isotropic deformation when defined by isotropic material properties. Secondly, the phenomenon commonly known as volume locking or shear locking is of particular concern when using linear wedge elements and is exacerbated when the subroutine UMAT (Abaqus, 2013c) is utilised. This is no longer of serious concern when quadratic wedge elements are utilised. The arrangement of elements, three layers and twenty four rings, was chosen by increasing the number of element layers and rings until the corresponding change in the solution became less than 0.1% in terms of apical deformation. C3D15H elements contain nine integration points. It was judged that the number of elements provided good refinement regarding the regional variation of material properties, which were individually characterised for each integration point.

Graphical representations from the output of the numerical law are presented in Figure 4.11. The graphical representations show the regional variation of both anisotropic distribution and density.

As in Equation 4.26, the anisotropic and density weighting visualised in Figure 4.11 is applied to the representation of both the lamellae fibrils distributed on the tangent plane and the ILC fibrils distributed above and below the tangent plane at an inclination of 15°.

Derivation of Material Properties

Characteristic experimental data derived from a total of 121 fresh human donor corneas (Elsheikh et al., 2007a, 2009, 2010b) has been used to derive material parameters. Data includes shear test results which do not generate tangential tensile strain, thus allowing isolation of out-of-tangential behaviour during numerical analysis; and inflation data which generates multi-axis strain, including relatively large tangential strains.

Material law parameters were derived using multi-objective, multistage, inverse analysis. The first stage was to derive the material parameters representing the matrix and the ILC fibrils, while the second stage was to derive the material parameters representing the lamellae fibrils. This multistage approach can only be utilised in special cases such as this, where the outcome of subsequent stages cannot affect the outcome of prerequisite stages. Shear loading a specimen will not result in tensile forces on the tangent plane. This engineering observation leads to the understanding that numerical representation of the lamellae fibrils will have no effect on the simulation of shear behaviour. Therefore, the material properties representing the matrix and ILC fibrils can be derived in isolation prior to the derivation of lamellae fibril parameters.

The out-of-tangential stiffness is orders of magnitude lower than the tensile stiffness acting on the tangent plane (Elsheikh et al., 2009; Petsche et al., 2012). Further, the

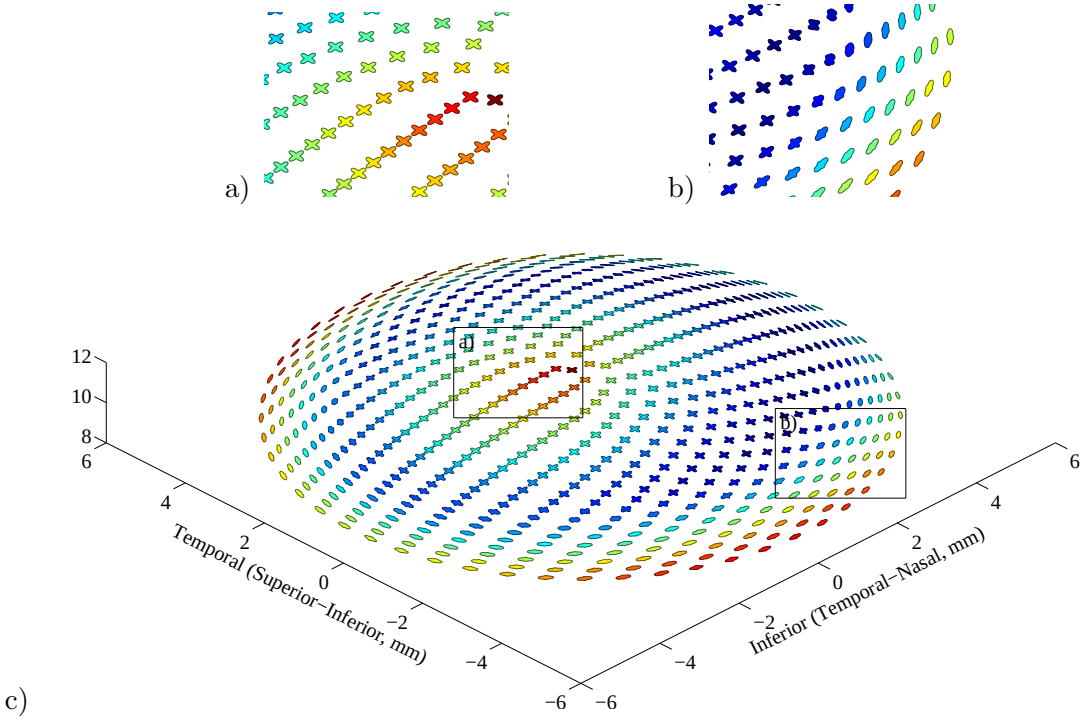

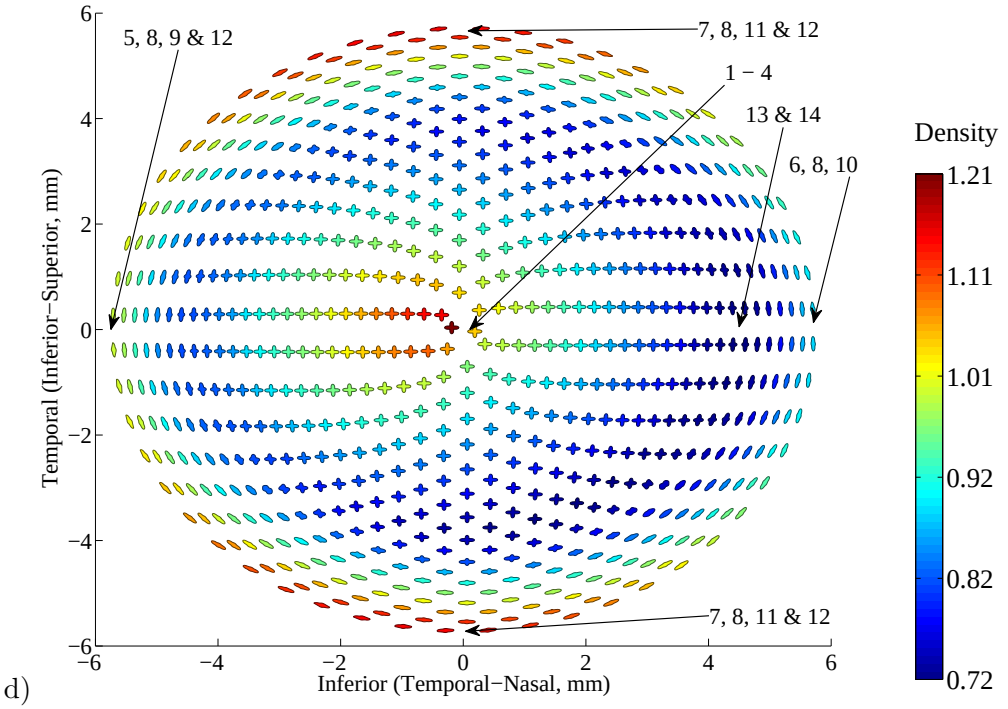

Figure 4.11: Output from numerical simulation representing the regional variation of fibrils. The anisotropic weighting is presented as individual polar plots at discrete locations. Density is represented by the colour map. Directional related stiffness is a combination of the local anisotropic distribution and the density function. Figures (a) and (b) provide close-up images of the central cornea and limbal regions, figure (c) highlights the 3D alignment of fibril anisotropic representation to the tangent plane of the cornea and figure (d) provides the regional distribution from an anterior view. Numbered arrows are used for reference in Fig. 4.13.

experimental data representing the out-of-tangential behaviour is limited to 12 donor aged $61-74$ in the study by Elsheikh et al. (2009) and 4 donor aged $82-86$ in the study by Petsche et al. (2012). For these reasons parameters representing the ILC fibrils and the matrix were derived independently of potential age related variations.

Shear and tangential tensile stiffness have been calculated to describe the characteristic human corneal behaviour from $30-100$ years old over a range of strain levels representative of *in vivo* conditions. Identical material parameters, including definitions of anisotropy were applied to shear and inflation models for each age group.

An inverse analysis approach was implemented to derive the influencing parameters in the simulation of shear testing; C_{10}, γ_2 and μ_2. The root mean square error between experimental data and numerical simulations is reduced to its minimum. With these values derived and fixed, attention was shifted to simulations of characteristic corneal inflation data. During this analysis all edge nodes were pinned to simulate the boundary conditions of the experimental programme (Elsheikh et al., 2007a). The two parameters, γ_1 and μ_1 of the fibril representing constituent of Equation 4.13 were determined using inverse analysis while reducing the root mean square error between experimental and numerical data. In both stages, the SHERPA algorithm was utilised within the design optimisation software package.

Simulation of Corvis® ST Non-contact Tonometry

The maximum deformation profile was obtained from 84 patients during Corvis® ST non-contact topography. The mean maximum deformation was computed from this clinical data-set. The tomometry loading was simulated on the numerical model. The initial curvature of the corneal model was achieved using the stress-free configuration method as described in Section 4.1.4 with an IOP of 16 mmHg. In this modelling case, a rolling pin support inclined at 23° was provided as the boundary condition around the limbus. This was found in an earlier study to provide a support condition which

most accurately represented the limbal support condition of the intact eye (Elsheikh et al., 2007b).

Results

Parameters for the presented model have been derived to simultaneously represent characteristic shear and inflation responses, Table 4.2. The error (RMS) for all simulation was less than 1.5% of the total deformation simulated ($200 - 300$ μm). Figure 4.12 provides comparisons between characteristic experimental data and numerical simulations. The experimentally obtained, characteristic age-related stiffening is presented with the respective numerical representation. Both exhibit approximately 60μm less deformation from an increase of 45 mmHg across the $30 - 100$ year old age range.

Table 4.2: **Numerical parameters derived for the constitutive model describing both tangential and out-of-tangential characteristic corneal behaviour from 30 to 100 years-of-age.**

Parameter	Value
D	10^{-5}
C_{10}	0.009
γ_1	$(0.121\text{age} + 165)$
μ_1	$\left(5.8 \times 10^{-6}\text{age} + 110 \times 10^{-6}\right)$
γ_2	2
μ_2	0.319

Due to the anisotropic description and the regional variation of collagen-related stiffness the model contains different stress-strain relationships on both the global scale (between discrete integration points) and on the local scale (in different directions at each particular integration point). Equation 4.17 and 4.21 describe the regional variations of local-anisotropic distribution and density respectively. To examine the effect of these functions a selection of stress-strain relationships are presented in Figure 4.13.

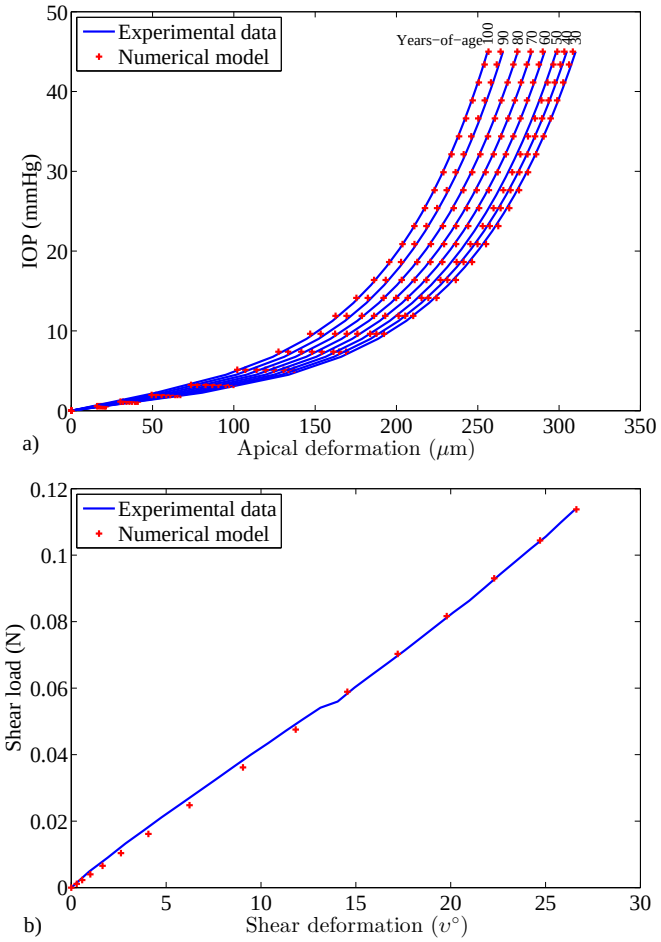

Figure 4.12: Characteristic experimental data and results of numerical simulation: (a) corneal inflation; (b) corneal shear

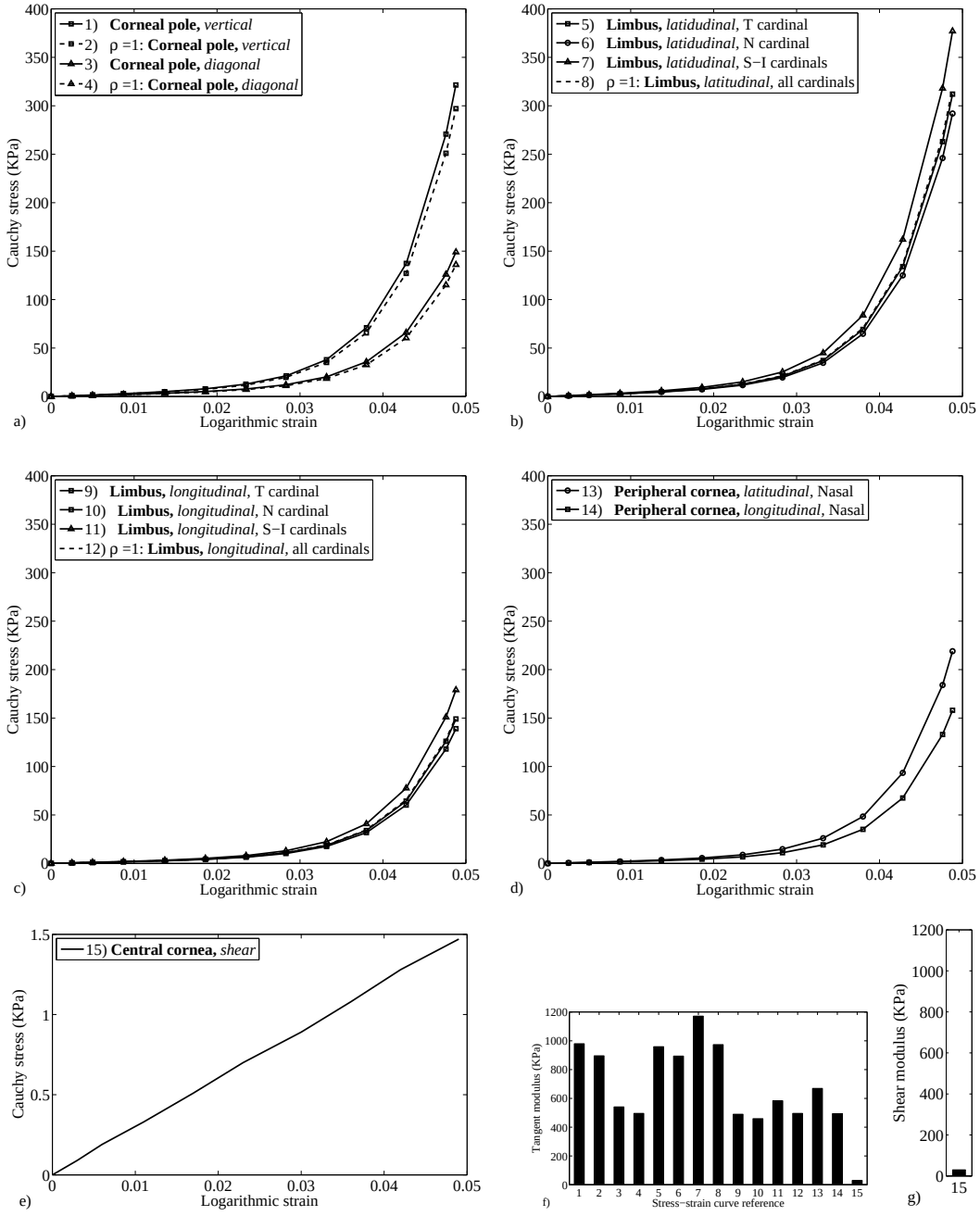

Figure 4.13: Material stiffness relationships representing characteristic behaviour of a 50 year old: (a-d) regional and directional specific stress-strain behaviour obtained parallel to the tangent plane. The location of each specific relationship is obtained from the numerical reference Figure 4.11. Dashed lines denote hypothetical relationships where the regional variation of fibril density is removed such that $\zeta = 1$; (e) stress-strain relationship representing shear behaviour (note the different scale on the stress axis compared with plots (a-d)); (f) tangent modulus for the 14 stress-strain relationships presented in (a-d); (g) shear modulus. Values represent the stiffness at 0.02 logarithmic strain.

Clinical, non-contact tonometry was modelled. The comparison between the clinical data and the numerical simulation in terms of before maximum deformation and the deformed profile are presented in Figure 4.14.

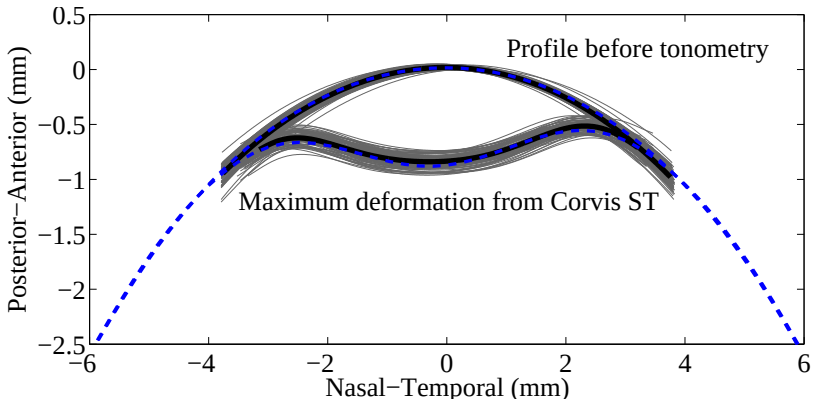

Figure 4.14: Simulation of Corvis® ST non-contact tonometry. Grey lines show the deformed and undeformed corneal profiles from 84 patient and the black lines provide the mean of these, while the blue lines provide the respective profiles obtained through numerical simulation.

This simulation was also used to quantify the magnitude of shear strain observed during this type of clinical practice. The results in Figure 4.15 show resultant shear strains over 0.25 in the mid-stroma circumferential to the corneal pole.

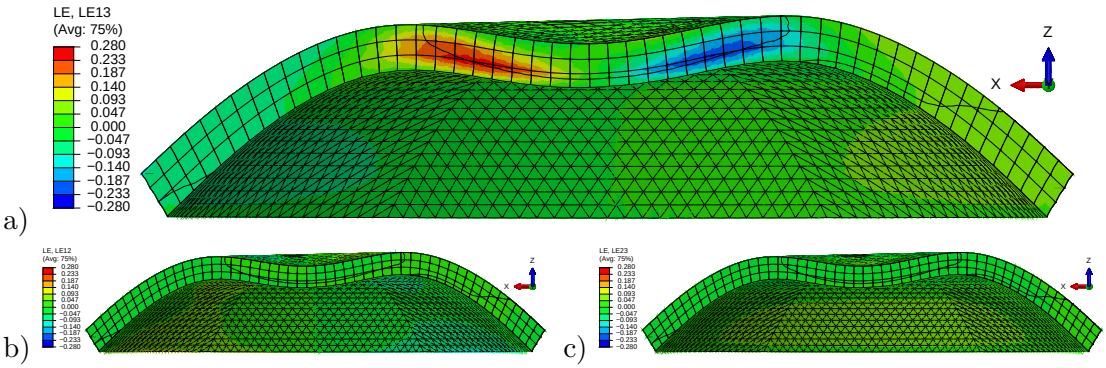

Figure 4.15: Simulation of Corvis® ST non-contact tonometry. Figures (a), (b) and (c) present the x-z, x-y and y-z components of the logarithmic shear strains at the maximum deformation respectively. Image provides a cross-sectional view of the model.

As this model is anisotropic, each direction, at each integration point, was defined

with its own stress-strain relationship. Equation 4.17 and 4.21 describe the regional variations of local-anisotropic distribution and density respectively. To examine the affect of these functions a selection of stress-strain relationships are presented in Figure 4.13

Average maximum deformation observed from 84 patients during Corvis® ST non-contact topography is simulated to quantify the magnitude of shear strain observed during this type of clinical practice, Figure 4.14. The results in Figure 4.15 show resultant shear strains over 0.25.

Discussion

Within this study the numerical representation of corneal microstructure has been developed within a continuum framework and applied to FEA. The model was applied to an extensive experimental database to obtain numerical relationships which describe: regional variation of collagen density and anisotropy; the lamellae and ILC stiffness; and the stiffness variation with age.

The stress-strain relationships for this model cannot be derived algebraically due to the anisotropy, inhomogeneity and the fact that the fibril component of the constitutive model is only activated locally during tensile strains. To present stress-strain relationships the model was applied to a single element and relationships where extracted describing the directional response of the element.

Analysis of fibril distribution in Figure 4.7 showed no symmetry about either the T-N or S-I axes, while the regions surrounding the S-I axis exhibited higher concentrations of collagen fibrils than the T-N axis. In the central corneal region the peak density is off-centre towards T-S. In the limbal region the nasal area had a lower density than the temporal area, while the superior and inferior areas contain lower densities. The region with the lowest concentration of collagen fibrils was found to be the transition zone

between the central region (with orthogonal fibrils) and the peripheral/limbal region with predominantly circumferential fibrils (region (e) Figures 4.8 and 4.9).

Examination of the relative stiffness showed an almost linear relationship between the stiffness and density function, for example: the same anisotropic distribution was found circumferentially at all locations on the limbus, while the density function ranges from 0.92 to 1.21 (ratio 1/1.315), the respective stiffness at 0.02 logarithmic strain ranged from 894 KPa to 1171 KPa (ratio 1/1.309) (Figure 4.13). This almost linear relationship is due to the relatively low stiffness of the matrix component. The concept relating density of fibrils to stiffness is not new. Pinsky et al. (2005) for example, related local (anisotropic) distribution of fibrils to anisotropic stiffness. Here, this concept has been extended to regional variation of total density to stiffness.

The findings of relative stiffness are in line with previous studies. For example, the transition zone of the cornea characteristically exhibits the lowest stiffness for the cornea (Boyce et al., 2008). Stress-stain relationships are shown in Figure 4.13 for: the cardinal points on the tangent plane in both the longitudinal and latitudinal directions; the central cornea in both S-I and T-N directions parallel to the tangent plane; and the shear stress-strain relationship at the corneal apex in the S-I direction. Previous studies discussed in this study have considered the regional variation of anisotropic fibril distribution obtained from WAXS, while omitting the experimental data pertaining to the total fibril density. To demonstrate the biomechanical result of the inclusion of this characteristic Figure 4.13 includes hypothetical stress-strain relationships where the density function is omitted such that $\rho = 1$ (Equation 4.26) for all areas. The inclusion of the density function results in a 21% increase in the stiffness at the S-I limbal cardinal points (Figure 4.13(c). This can be directly correlated to the density function (Figure 4.9) and the output of the density function from the simulation (Figure 4.11). Therefore, the increased stiffness highlighted above is globally balanced by decreases in stiffness elsewhere. It is acknowledged that collagen fibrils are the primary contributor to material stiffness and the effect of including total fibril density within the model is ev-

ident. Therefore, it is expected that the accuracy of microstructural modelling relies on the inclusion of experimental data demonstrating the regional variation in fibril content.

The experimental behaviour of corneal tissue under shear and inflation conditions, together with the numerical analysis presented here, provides evidence that the out-of-tangential stiffness is $2-3$ orders of magnitude lower than the tangential tensile stiffness. For example, tangential stiffness for a characteristic 50 year-old was calculated to be 459 KPa to 1171 KPa and shear stiffness was calculated as 30 KPa. These values relate to 0.02 logarithmic strain for tangential stiffness. Shear stiffness followed linear behaviour up to the experimentally assessed strain limit of 0.5. Petsche et al. (2012) reported similar but not identical measurements of shear stiffness upto 0.01 strain in which they found a mean full thickness shear modulus of 95 KPa. The variation in experimental results could be explained by a number of factors including, for example, the known variation in biomechanical properties (Elsheikh et al., 2010a,b) and/or variations in the testing procedures (lateral and torsional shear) which, considering the very low stiffness observed in both studies, could have factored considerably in the results. The accurate numerical representation of these characteristics is of particular importance when simulating bending and/or surgical intervention as the ratio of shear to tangential strain will increase in these situations. Both shear and direct isotropic stiffness parameters were derived independently of age-related stiffness variation, both are limitations of this study which are currently unavoidable due to the limitations of experimental data in this area.

There are a number of limitations to this study:

1. the numerical parameters defining ILC and matrix stiffness were derived independently of age related variations in stiffness, this limitation is due to restrictions in the experimental database of shear testing;

2. the model retains the capacity to absorb potential variations upon their experimental measurement, despite this limitation, it would not be expected that ex-

perimentally obtained shear behaviour would have a considerable affect on the outcome of inflation simulations due to the relatively low stiffness.

4.3.4 A Viscoelastic, Anisotropic, Hyperelastic Constitutive Model of the Human Cornea

The following section has been prepared for publication in a similar form:
Whitford C., Movchan N., & Elsheikh A., **A Viscoelastic, Anisotropic, Hyperelastic Constitutive Model of the Human Cornea**.

A constitutive numerical model based on the continuum mechanics theory has been developed which represents interlamellar cohesion, regional variation of collagen fibril density, 3D anisotropy and both age-related viscoelastic and hyperelastic stiffening behaviour of the human cornea. Experimental data gathered from a number of previous studies on 48 *ex vivo* human cornea (inflation and shear tests) enabled numerical model calibration. Wide angle X-ray scattering and electron microscopy provided measured data which quantifies microstructural arrangements associated with stiffness. This present study suggests that stiffness parallel to the lamellae of the cornea approximately doubles with an increase in strain-rate from 0.5 to 5%/min. While the underlying stromal matrix provides a stiffness $2-3$ orders of magnitude lower than the lamellae. The model has been simultaneously calibrated to within 5% error across three age groups ranging from $50-95$ years, three strain-rates and two loading scenarios. Age and strain-rate dependent material coefficients allow finite element modelling for an individual patient with material stiffness approximated by their age under varying loading scenarios. This present study addresses a significant gap in numerical representation of the cornea and has great potential in both daily clinical practice for the planning and optimisation of corrective procedures and in pre-clinical optimisation of diagnostic procedures.

Introduction

This present study attempts to rectify the shortfall in knowledge described in Section 2.4 and calibrates the proposed model with existing *ex vivo* human data. In addition, the constitutive framework has the potentially be calibrated to appropriate *in vivo* experimental data as it becomes available. The previous section introduced the representation of the regional variation of collagen fibril density. This previous model is included, and expanded upon, within the present study. The proposed constitutive model decomposes stress-strain behaviour into four contributions motivated by the micromechanics of the stroma: (1) to (3) representing the equilibrium response of the network and (4) a time-dependent constituent of the network which represents the relaxing and stiffening of the collagen fibrils, with time as a non-linear rate-dependent departure from the equilibrium responses. Where (1) represents dilation, (2) describes the isotropic matrix distortion response in both tension and compression stiffness, (3) activated only under tensile strain, represents the anisotropic and regional variation of collagen fibrils.

The topography of the cornea is determined by the balanced state between the forces acting upon it and its mechanical stiffness which is defined by cornea's stress-free form and material stiffness. The term *balanced state* is often referred to as the *equilibrium state*. However, *equilibrium* refers specifically to static behaviour and this term is no longer appropriate while describing this relationship in the context of viscoelastic behaviour. This is due to the dynamic state of the system, including the forces acting within the material and mass inertia of the system where *equilibrium state* is only achieved as time tends to infinity and both internal forces and inertia tend to zero.

Following from the model presented in Section 4.3.3, which was calibrated based on static theory, a second constitutive model is presented. Equation 4.26 can be written in the form:

$$\psi = U^{\infty}\left[J\right] + \bar{\psi}_{m}^{\infty}\left[\bar{I}_{1}\right] + \bar{\psi}_{f}^{\infty}\left[\bar{I}_{4,6}\right] \tag{4.29}$$

where ∞ defines the system at equilibrium in the time domain.

To accommodate rate-dependency within the model the response of the material becomes a function of time, $t \in [0, T]$, where reference time, $t = 0$, relates to the reference configuration, Ω_0.

Viscoelastic effects are described using the concept of internal variables. These variables are not accessible to direct observation Holzapfel et al. (2000). Viscoelastic behaviour is modelled by $m \geq 1$ relaxation processes with corresponding relaxation times, $\tau_\alpha \in [0, \infty]$, $\alpha = 1, \cdots, m$ $(m \geq 1)$, describing the rate of decay of the stress. These material variables vanish at the equilibrium state; which does not depend on time. The internal variables are denoted by Γ_α, $\alpha = 1, \cdots, m$.

Mathematically the adaptation of the model to represent viscoelastic response could be performed prior to the isochoric split, or the split between matrix and fibril definitions, therefore accommodating viscoelastic behaviour of the dilation and/or the matrix within the model. However, the matrix and dilation contributions to stiffness have been shown to have relatively less contribution to stiffness than fibril behaviour (Section 4.3.3). Holzapfel and Gasser (2001) presented a model where the viscoelastic behaviour was a function of the distortion component of the strain-energy after the isochoric split had been performed. That model is modified here and the dissipative potentials are introduced providing: the viscoelastic constituent as a function of the fibril constituent, $\sum_{\alpha=1}^{m} \bar{\psi}_{f\,\alpha}^{\infty} \left[\bar{\mathbf{C}}, \mathbf{A}, \mathbf{B}, \bar{\Gamma}_\alpha\right]$. The tangential and out-of-tangential fibril constituents of the model being functions of the 4^{th} and 6^{th} strain invariants respectively leads to $\sum_{\alpha=1}^{m} \sum_{a=4,6} \bar{\psi}_{f\,\alpha\,a}^{\infty} \left[\bar{\mathbf{C}}, \bar{I}_a, \bar{\Gamma}_\alpha\right]$, and the strain-energy function from Equation 4.29 becomes:

$$\psi = U^{\infty}\left[J\right] + \bar{\psi}_{m}^{\infty}\left[\bar{I}_1\right] + \bar{\psi}_{f}^{\infty}\left[\bar{I}_{4,6}\right] + \sum_{\alpha=1}^{m} \bar{\psi}_{f\,\alpha}^{\infty}\left[\bar{\mathbf{C}}, \bar{I}_{4,6}, \bar{\Gamma}_\alpha\right] \tag{4.30}$$

At this stage the symmetric second Piola-Kirchhoff stress tensor can be written describing the equilibrium stress response of the material:

$$\mathbf{S}^{\infty} = \mathbf{S}^{\infty}_{dil} + \mathbf{S}^{\infty}_{m} + \mathbf{S}^{\infty}_{f}. \tag{4.31}$$

The three contributions to the constitutive model, $\mathbf{S}^{\infty}_{dil}$, $\mathbf{S}^{\infty}_{m}$ and $\mathbf{S}^{\infty}_{f}$, describe the dilation, and the isotropic and anisotropic distortion responses of the matrix and fibres respectively. These are given by:

$$\mathbf{S}^{\infty}_{dil} = 2\frac{\partial U^{\infty}}{\partial \mathbf{C}},\ \mathbf{S}^{\infty}_{m} = 2\frac{\partial \psi^{\infty}_{m}}{\partial \mathbf{C}},\ \mathbf{S}^{\infty}_{f} = 2\frac{\partial \psi^{\infty}_{f}}{\partial \mathbf{C}} \tag{4.32}$$

From Holzapfel and Gasser (2001) the rate-dependency is expressed as an additional component to the constitutive equation at time t_{n+1} and an adaptation the stress function is required where the non-equilibrium stresses, $\mathbf{Q}_{\alpha} = J^{-2/3}\mathbb{P} : \hat{\mathbf{Q}}_{\alpha}$ where the 4^{th} order projection tensor, $\mathbb{P}$, is given by:

$$\mathbb{P} = \mathbb{I} - \mathbf{C}^{-1} \otimes (\mathbf{C}/3), \quad \mathbb{I}_{IJKL} = \Big(\delta_{IK}\delta_{JL} + \delta_{IJ}\delta_{KL}\Big)/2 \tag{4.33}$$

and $\hat{\mathbf{Q}}_{\alpha}$ is given by:

$$\hat{\mathbf{Q}}_{\alpha} = 2\frac{\partial \psi_{f\,\alpha}\left[\bar{\mathbf{C}}, \mathbf{A}, \mathbf{B}\right]}{\partial \bar{\mathbf{C}}} \tag{4.34}$$

The internal dissipation is defined as: $\boldsymbol{\mathcal{D}}_{int} = \sum_{\alpha=1}^{m} \mathbf{Q}_{\alpha} : \dot{\bar{\Gamma}}_{\alpha}/2 \geq 0$. As the dissipation vanishes at equilibrium ($t \to \infty$)

$$\mathbf{Q}_{\alpha} = -2\frac{\partial \psi_{f\,\alpha}}{\partial \bar{\Gamma}_{\alpha}}\bigg|_{t\to\infty} = \mathbf{0}, \quad \alpha = 1, \cdots, m \tag{4.35}$$

and Equation 4.31 becomes:

$$\mathbf{S}_{n+1} = \left(\mathbf{S}^{\infty}_{dil} + \mathbf{S}^{\infty}_{m} + \mathbf{S}^{\infty}_{f} + \sum_{\alpha=1}^{m} \mathbf{Q}_{\alpha}\right)_{n+1} \tag{4.36}$$

where the non-equilibrium stresses are defined by:

$$(\mathbf{Q}_{\alpha})_{n+1} = (\boldsymbol{\mathcal{H}}_{\alpha})_{n} + \beta^{\infty}_{\alpha} \exp(\xi_{\alpha}) \left(\mathbf{S}^{\infty}_{f}\right)_{n+1}, \quad \alpha = 1, \cdots, m \tag{4.37}$$

and the definition of the history term, $(\boldsymbol{\mathcal{H}}_\alpha)_n$, $\alpha = 1, \cdots, m$, is modified from Holzapfel and Gasser (2001) providing

$$(\boldsymbol{\mathcal{H}}_\alpha)_n = \exp(\xi_\alpha)\left(\exp(\xi_\alpha)(\mathbf{Q}_\alpha)_n - \beta_\alpha^\infty \left(\mathbf{S}_f^\infty\right)_n\right), \quad \xi_\alpha = -\frac{\Delta t}{2\tau_\alpha} \tag{4.38}$$

$\beta_\alpha^\infty \in [0, \infty]$ and $\tau_\alpha \in [0, \infty]$, $\alpha = 1, \cdots, m$ are non-dimensional and time-dimensional strain-energy factors respectively. These remained to be defined. For mathematical purposes the potentially inaccurate approximation is made that the viscoelastic stress of the reference configuration, $\mathbf{Q}_\alpha^{0+} = \mathbf{0}$. The accuracy of this approximation relates to the implementation of the constitutive model and is discussed later in the study. The stiffness tensor at t_{n+1} can similarly be written as:

$$\mathbf{D}_{n+1} = \left(\mathbf{D}_{dil}^\infty + \mathbf{D}_m^\infty + \mathbf{D}_f^\infty + \sum_{\alpha=1}^{m} \mathbf{D}_{vis}^\alpha\right)_{n+1} \tag{4.39}$$

where

$$\mathbf{D}_{dil}^\infty = 2\frac{\partial \mathbf{S}_{dil}^\infty}{\partial \mathbf{C}}, \quad \mathbf{D}_m^\infty = 2\frac{\partial \mathbf{S}_m^\infty}{\partial \mathbf{C}}, \quad \mathbf{D}_f^\infty = 2\frac{\partial \mathbf{S}_f^\infty}{\partial \mathbf{C}} \tag{4.40}$$

and

$$(\mathbf{D}_{vis}^\alpha)_{n+1} = \delta_\alpha \left(\mathbf{D}_f^\infty\right)_{n+1}, \ \delta_\alpha = \beta_\alpha^\infty \exp(\xi_\alpha), \ \alpha = 1, \cdots, m \tag{4.41}$$

Implementation of Numerical Simulation

Numerical simulations have been conducted using finite element analysis (FEA). Geometric modelling was performed using bespoke software that provides geometry, which can be imported into finite element solvers as an orphan mesh. Finite element solver Abaqus/Standard 6.13 (Dassault Systmes Simulia Corp., Rhode Island, USA) was used. Abaqus is well known for its ability to analyse non-linear problems. However, its ability to provide state-of-the-art representation of biological material properties, and both regional and local variation of these properties, is limited. Thus, Abaqus was used in

conjunction with bespoke subroutines (SDVINI & UMAT) written in FORTRAN to implement the constitutive model described above.

The fibril component of Equation 4.30 is given by:

$$\bar{\psi}_f^{\infty}\left[\bar{\mathbf{C}},\mathbf{A},\mathbf{B}\right]=\zeta\frac{1}{\pi}\int_0^{\pi}\chi\Big(\bar{\psi}_{f,lamellae}^{\infty}\left[\bar{\mathbf{C}},\mathbf{A}\right]+\bar{\psi}_{f,ILC}^{\infty}\left[\bar{\mathbf{C}},\mathbf{B}\right]\Big)d\theta_L, \tag{4.42}$$

The integral of Equation 4.42 was discretised into steps of one degree by $\frac{1}{\pi}\int_0^{\pi} d\theta_L \rightarrow \frac{1}{180}\sum_{i=1}^{180}\theta_{L,i}$, where $\theta_{L,i}$ defines the orientation of the one hundred and eighty directions of anisotropy per integration point within the model. The assumption that the fibril constituent of the model only provided tensile stiffness was adopted throughout all behaviour stages.

Subroutine SDVINI was used to provide initial, reference-configuration and location-based conditions such as fibril density representation. These location-based properties are defined individually for each integration point. These are implemented into the numerical simulation using the UMAT subroutine as demonstrated in the Abaqus User Subroutines Reference Guide (Abaqus, 2013c). UMAT is also used to define current-configuration properties such as anisotropy.

Models were generated by the same methods as described in Section 4.3.3.

Derivation of Material Properties

Characteristic experimental data has been obtained from 48 fresh human donor corneas. Data includes 36 corneas tested under inflation and 12 corneas tested under shear. The corneas tested under inflation were divided into two groups: 23 corneas tested with 37.5 mmHg/min pressure rate and 13 corneas tested with 3.75 mmHg/min rate (Elsheikh et al., 2007a). The age range of the two groups was $51-95$ (77.6 ± 13.2 (mean, SD)) and $50-95$ (75.7 ± 14.2) years respectively. Within each group the corneas were

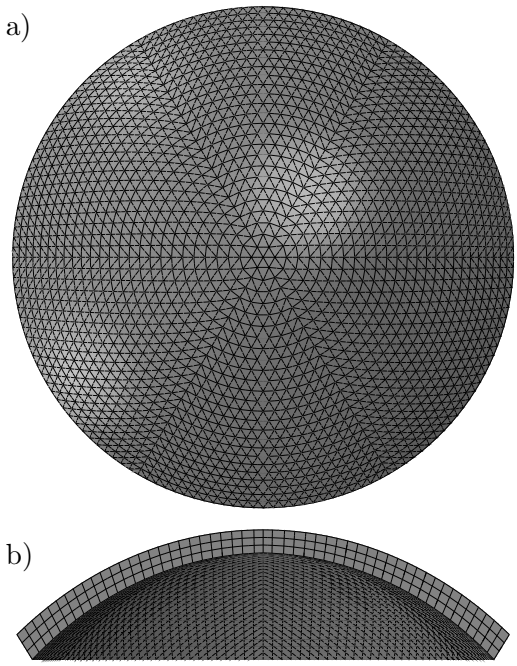

Figure 4.16: Finite element model (FEM) of the human cornea: (a) anterior view; (b) side elevation view

divided into three age subgroups: $50-64$, $65-79$, and $80-95$ years. The number of corneas tested under 37.5 mmHg/min was 4, 6, and 13 within the three age subgroups respectively. The corresponding numbers tested under 3.75 mmHg/min were 4, 4, and 5. 12 human donor corneas, aged between 61 and 74 years (67.7 ± 5.8), were tested to determine the behaviour of stromal tissue under surface shear at a shear deformation rate of 10%/min (with respect to the tissue's thickness) (Elsheikh et al., 2009). As considered in Section 4.3.3, shear tests do not generate strains parallel to the tangent plane; allowing the isolation of out-of-tangential behaviour during numerical analysis. In contrast, inflation generates multi-axis strain, including relatively large tangential strains. The isolation of material behaviour through multi-objective experimental fitting was utilised in Section 4.3.3 and is again utilised in this study. In addition to this isolation of anisotropic stiffness calibration the three different loading rates allow the simultaneous calibration of viscoelastic parameters.

The external parameters (ζ, χ) describing the local and global variation in fibril distribution and the internal parameters (C_{10}, D) which describe the stiffness of the non-

fibril matrix and the volume change are unaffected by the introduction of the internal variables which relate to the viscoelastic behaviour. These values therefore remain as derived in Section 4.3.3. However the internal parameters $(\mu_{1,2}, \gamma_{1,2})$ are intrinsically combined with the viscoelastic parameters in the partial differential equations of the viscoelastic behaviour. Further, in earlier studies describing the anisotropic distribution of collagen fibrils, for example (Pinsky et al., 2005; Studer et al., 2010) and Section 4.3.3, the material parameters were derived to define the hyperelastic response at a non-equilibrium state. The inclusion of the viscoelastic term to the fibril representation requires that parameters $\mu_{1,2}, \gamma_{1,2}$ describing the fibril response are redefined such that they are intended to represent the equilibrium behaviour.

The parameters which remain to be determined $(\mu_{1,2}, \gamma_{1,2}, \beta_\alpha, \tau_\alpha : \alpha = 1, \cdots, m)$, were derived using a multi-objective inverse analysis procedure. The objectives were to reduce the RMS errors between the characteristic experiment results for corneal shear and inflation at different loading rates, and their respective numerical simulations. In Section 4.3.3 the parameters defining shear behaviour could be derived independently as the parameters defining tangential stiffness had no influence on this behaviour. However, due to the necessary approximation that the viscoelastic behaviour of the interlamellae fibrils is the same as the lamellae fibrils the viscoelastic parameters for both family of fibrils require simultaneous derivation. The constitutive model above has been expressed for multiple orders of viscoelastic behaviour which can be represented through the use of the α term $(\alpha = 1, \cdots, m)$. The derivation process for material parameters included trials to determine the appropriate value for m.

Results

Numerical simulations were fitted to characteristic experimental data (Figure 4.17). Initial trials were conducted utilising a first-order viscoelastic model during which a RMS error for the age group $80 - 95$ years of 4% of the total deformation simulated $(200 - 550\ \mu\text{m})$ was achieved. However, the RMS increased to 5% for age group $50 - 65$

and the RMS for shear inflation was 3%. The fitting trend between age groups resulted in overestimation of displacement at low IOP and underestimation at higher IOP for the $50-65$ age groups with a reversal of this trend when representing the $80-95$ age-group. Inverse analysis trials to derive material parameters were also conducted on a second-order viscoelastic model. For these separate trials the RMS for all age-groups and shear was less than 4%.

Parameters of the proposed model have been simultaneously determined to represent characteristic shear and inflation responses across 3 different loading rates and for 3 age groups (Table 4.3 and Figure 4.18). As described above, during the multiple iterations of analysis both γ_2 and μ_2, governing the equilibrium behaviour of ILC fibrils, were free to optimise. However, the output of the procedures consistently provided values within 0.05% of each other. Due to this non-significant difference results have been provided based on the mean of these values and are therefore constant with age. Parameters γ_1, μ_1, β_1 and β_2 are non-dimensional, γ_1 decreases, and μ_1, β_1 increases with age while the contribution of the second order viscoelastic term (controlled by β_2) dissipates to zero form the group $80-95$ years-of-age. τ_1 and τ_2 have units of seconds and increase with age.

Table 4.3: Numerical parameters derived for the constitutive model describing the anisotropic, viscoelastic and hyperelastic corneal behaviour from 50 to 95 years-of-age

Parameter	Value
D (-)	10^{-5}
C_{10} (-)	0.009
μ_2 (-)	3.85
γ_2 (-)	7.42×10^{-6}

Stiffness varies directionally and by location across the entire cornea as previously described. Figure 4.19 provides the stiffness relationships as the tangent modulus at selected discrete locations and directions across the cornea and varying strain rates.

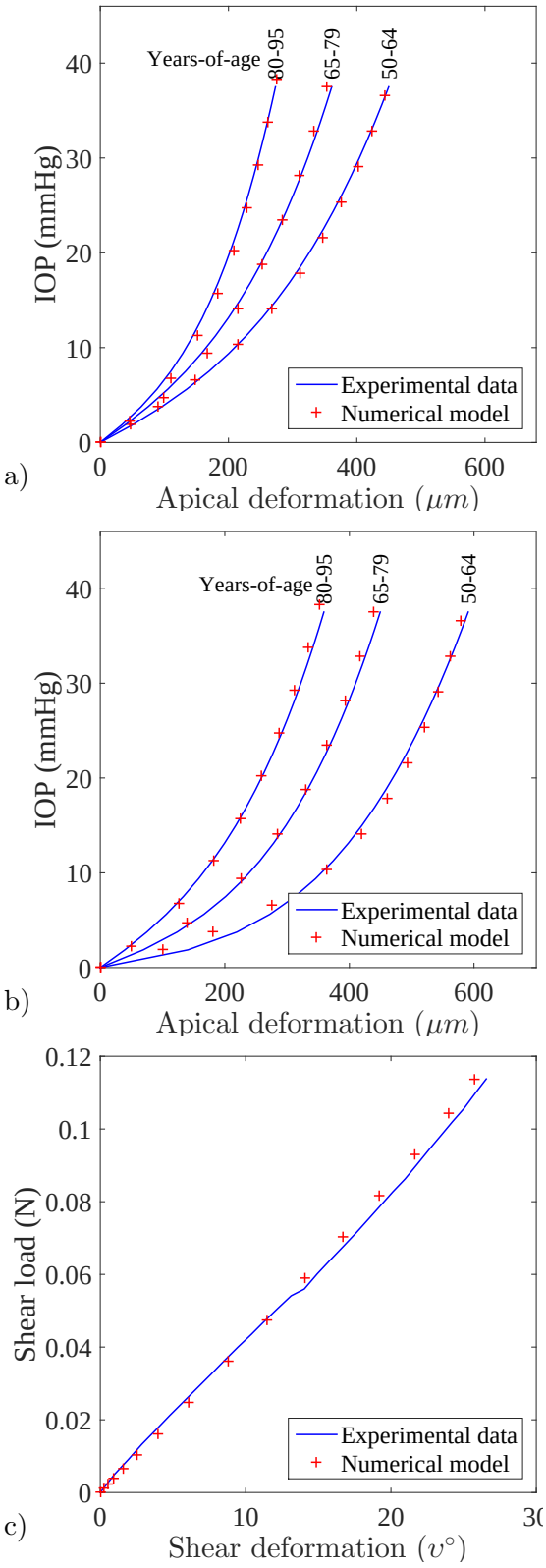

Figure 4.17: Characteristic experimental data and results of numerical simulation: (a) corneal inflation at 37.5 mmHg/min, (b) corneal inflation at 3.75 mmHg/min and (c) corneal shear at 10% /min deformation

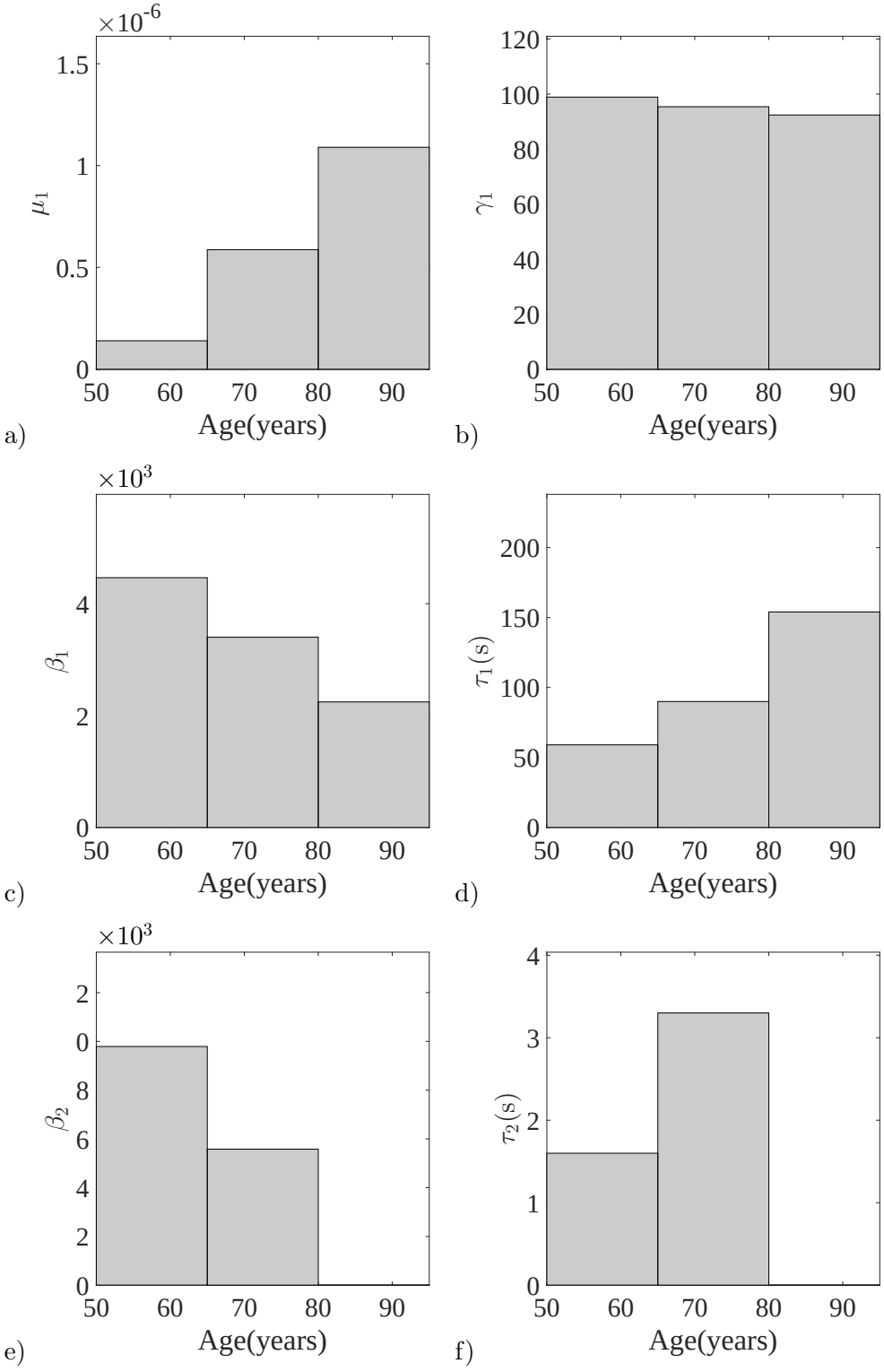

Figure 4.18: Numerical parameters ($\mu_1(a), \gamma_1(b), \beta_1(c), \tau_1(d), \beta_2(e)$ and $\tau_2(f)$) derived for the constitutive model describing the anisotropic, viscoelastic and hyperelastic corneal behaviour from 50 to 95 years-of-age. Bar chart provides the discrete values derived for the best fit with each age group. Other numerical parameters are constant with age and are presented in Table 4.3.

Figure 4.19 (a-c) provide the hyperelastic stress-strain relationships on the tangential plane of the cornea at 0.5% and 5%/min strain. Consistently the higher strain-rate results in higher stiffness when compared to the same location and direction. The greatest stiffness is observed circumferentially at the limbus. Of the stiffness relationships presented, the lowest stiffness is in the diagonal direction at the corneal pole. Figure 4.19 (d) provides the linear stress-strain relationship under shear at 10%/min, where this strain-rate relates to translational motion of the top surface of the cornea in relation to the lower surface with respect to its thickness. Figure 4.19 (e) highlights the tangent modulus at 2% strain and Figure 4.19 (f) presents the shear stiffness. From Figure 4.19 (e & f) it is clear that the shear stiffness is significantly less than tangential stiffness at 31.5 kPa compared to the range presented across the cornea for tangential stiffness, $370 - 1738$ kPa. At the presented strain the tangent modulus almost doubles for a strain-rate of 5%/min compared to 0.5%/min for the respective location and direction.

Discussion

Within this study, a numerical representation of corneal microstucture has been developed within the continuum framework and applied to FEA. The model was applied to an extensive experimental database to obtain numerical relationships which describe regional variation of collagen density and anisotropy; the lamellae and ILC stiffness; the stiffness variation with age; strain-rate dependent viscoelastic behaviour, and the viscoelastic variation with age (density and anisotropy being described in earlier studies and Section 4.3.3). As in Section 4.3.3, density and anisotropic distribution of fibrils could not be observed or modelled with respect to age. It was suggested in that earlier study that variation in stiffness with age could be a function of fibril behaviour, not arrangement. This hypothesis is expanded and reinforcedin the current study due to the ability of the model to accurately and simultaneously represent age-related stiffening and age-related viscoelasticity changes without the need to change mircostructural arrangement representation.

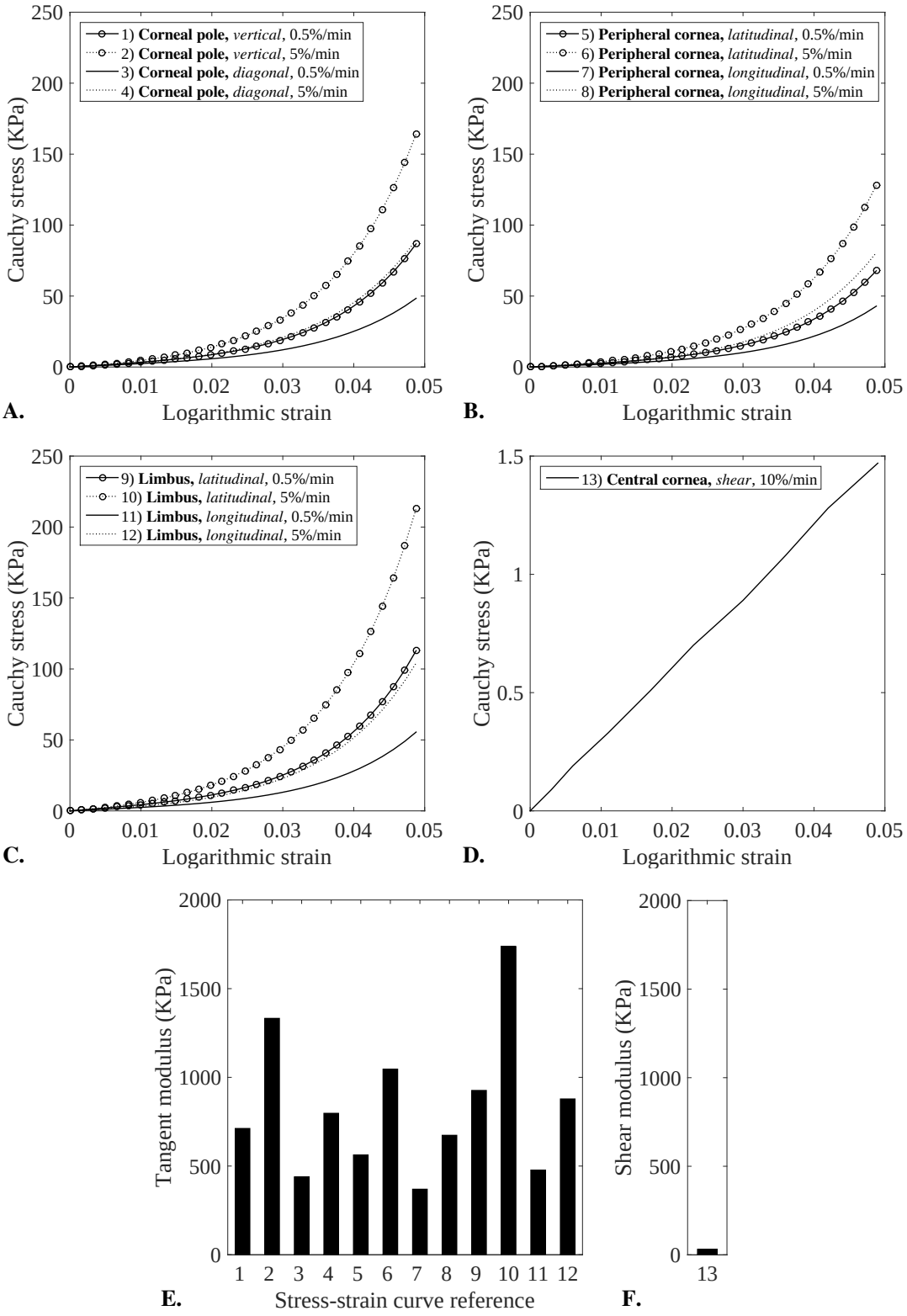

Figure 4.19: Material stiffness relationships representing characteristic behaviour of a 87 year old: (a-c) regional and directional specific stress-strain behaviour obtained parallel to the tangent plane; (d) stress-strain relationship representing shear behaviour (note the different scale on the stress axis compared with plots (a-c)); (e) tangent modulus for stress-strain relationships 1-12 (numbers refer to the labels in a-c); (f) shear modulus. Values represent the stiffness at 0.02 logarithmic strain.

The results of the calibration of the new constitutive model, which has been presented here, is the relationship between viscoelastic behaviour and age. Previous presentations of the cornea's strain-rate dependent stiffness have not been able to isolate the age-related stiffening, equilibrium behaviour from the age-related viscoelastic behaviour. The adopted parameters defining the viscoelastic behaviour, β and τ, define the initial proportion of non-equilibrium behaviour, in this case, the equilibrium behaviour of the fibrils, and the rate of decay of the non-equilibrium proportion. It has been shown that both the rate of decay and initial proportion of the first contribution to viscoelasticity increase with age. However, during trials it was found that a second contribution to viscoelasticity was required to provide reasonable representation particularly in the youngest age group, this contribution to viscoelasticity dissipated to zero in the group $80-95$ years-of-age. Such a finding may be of increased importance where the application of high-speed techniques, such as non-contact tonometry, are utilised to determine ocular behaviour.

The model which has been presented here introduces a viscoelastic constituent to the model presented in Section 4.3.3. That model attributed the regional and anisotropic distribution of stiffness to fibril density and arrangement. In this model the viscoelasticity decays with time ($t \to \infty$), with its initial contribution being proportional to the behaviour of the fibrils. This is a potentially inaccurate assumption as the viscoelastic behaviour could have contributions from the matrix components of the stroma. However, these components have been shown to have relatively low stiffness and therefore it is suggested that inaccuracies in this assumption would not lead to large inaccuracies in the overall behaviour of the model.

The intention, and potential capacity, of this constitutive model is that exclusion of the viscoelastic material component provides a model of the equilibrium state of the material. However, it is not possible to directly derive the equilibrium behaviour from the material parameters which have been presented here. This fact is due to the limita-

tions of the fitting procedure which was limited to three loading rates (two inflation and one shear). The material parameters which have been presented are only valid within the strain-rates from which they were derived and direct derivation of the equilibrium would require extrapolation.

Chapter 5

Overall Discussion

Experimental studies to determine biomechanical properties of porcine eye stromal tissue have become less common in recent years as the science has moved on. The limited number of studies include an assessment of residual stresses in porcine scleral tissue by Wang et al. (2015), in which the purpose was described as the development of techniques, not the derivation of properties. Similarly, Morris et al. (2013) used porcine ocular tissue to test the hypothesis that IOP elevations, induced by controlled increase of intraocular volume, are correlated with the biomechanical responses. The only study which has been identified from recent years with the purpose to determine biomechanical properties of porcine tissue utilised atomic force microscopy to determine nanomechanical properties (Papi et al., 2014). The lack of biomechanical property driven studies on porcine ocular tissue is probably due to the ultimate goal of biomechanics: to improve healthcare. With this goal, the study of non-human biomechanics becomes less desirable as the science progresses.

This study utilised porcine eye globes to develop the methodology and the results of a porcine eye globe was presented to illustrate the suitability of intact globe inflation tests. The human eye globe was included in this study for the same purpose, with the addition of assessing the specific suitability of the procedure to human eye globes. The

methodology of the experimental study was demonstrated through the results to be more suitable to human, than porcine eye globes. The results of the human eye globe study are likely to form part of a wider data set if, and when, more eye globes become available for testing. This is an important issue to consider. The limitation of whole eye globe availability restricted this area of the present study. This is likely to continue restricting research in this field while donor eye acquisition remains such a challenge due to the general priority of corneal transplantation, which requires inspection of the endothelium to determine transplantation suitability, thus rendering the eye globe unsuitable for this test procedure.

There were a number of significant challenges which required a solution from the experimental methodology which was developed for this study. There have been a number of studies which have observed the load-displacement behaviour of sections of the eye globe (see Sections 2 and 3 for examples for a discussion of these studies). However, no previous studies have addressed the challenges associated with observing the whole ocular surface while providing near physiologic conditions to the ocular vessel. These challenges were successfully addressed by this present study. It is expected that similar testing methodologies will become more common. This experimental study technique has now been duplicated in Wenzhou Medical University, China. However, the physical testing aspects of the study have been shown to require the development non-trivial skill-sets which will potentially limit how widespread this methodology becomes.

In addition to the advances in experimental techniques, this present study aimed to further understand the biomechanical properties of the ocular globe by advancing numerical representation of corneal stromal tissue. This was addressed by developing two constitutive material models which represented, amongst other characteristics, the arrangements of collagen fibrils. These 3D models, which described the mechanical effects of the collagen microstructure, related relative stiffness variation to the relative anisotropy and density of collagen fibrils, as observed by wide-angle X-ray scattering measured across the 2D surface. These models were calibrated for absolute stiffness by

fitting to experimental data. The relationship of stiffness variation between the 2D and 3D domains was achieved by creating a second family of fibrils proportional in density and anisotropic distribution to the primary family of fibrils. The first family of fibrils contribute to stiffness parallel to the tangential plane while the second family were inclined 15° from this plane. This proportional relationship of distribution between the fibrils measured in across the 2D surface and those acting in a 3D domain was able to represent the 3D stiffness with errors $< 1.5\%$ by calibrating the absolute stiffness in the 3D domian independently to the tangential stiffness.

In experimental studies, Winkler et al. (2011, 2013) and Abass et al. (2015) describe the changes in out-of-tangential arrangements of lamellae through the thickness of the cornea. However, inconsistencies between those studies suggest there are still gaps in the knowledge. The relationship between the collagen arrangement across the surface of the cornea and the relative, anisotropic stiffness was built upon in this present study and is well accepted. However, the out-of-tangential arrangement of collagen fibrils and lamellae and their relationship to the out-of-tangential stiffness remain to be fully discovered. (Petsche and Pinsky, 2013) adopted a direct relationship from second harmonic-generated images of lamellae (Winkler et al., 2011) where the fibril contribution to stiffness was distributed out of the tangential plane by an angle, ω by:

$$\omega(s) = 28.6^{\circ}\frac{e^{3.19(1-s)} - 1}{e^{3.19} - 1} \tag{5.1}$$

where s was the normalised depth through the thickness of the corneal stroma. There are a number of factors relating to that study which need to be considered: (1) the distribution angle was described as maximum (28.6°) at the anterior surface of the cornea, (2) the model assumes continuity of fibrils across the measured out-of-tangential direction, such that they are fully capable of transferring stresses in the directions considered and (3) the model is calibrated to a shear strain up to only 0.01. Regarding (1), the distribution angle must tend to zero at the surface. The assumption of (2) does not account for any potential straightening or corrugation effect which would reduce the proportional relationship between the lamellae of fibrils measured out-of-tangential and

the relative stiffness. Considering the use by Petsche and Pinsky (2013) of the main fibril hyperelastic model to accommodate shear stiffness, it follows that the stiffness could increase significantly if the calibrated model is extrapolated to describe higher strains than considered in (3). The present study calibrated the 3D stiffness of the models to shear up to 0.5 which allowed for the accurate modelling of deformations associated with non-contact tonometry which exhibited shear strains of 0.25. The shear stiffness was calculated to be $2-3$ orders of magnitude lower than the tangential stiffness, which was in agreement with (Petsche and Pinsky, 2013). In this present study this relationship was observed up to strains of 0.05 as this was considered a sensible range observed considering tangential tensile behaviour. Considering the highly non-linear behaviour observed in the tangential plane, extrapolation of these stress-strain relationships the levels of shear strains observed experimentally and clinically would result in very high stiffness. These findings suggest lamellae and fibrils measured out-of-tangential (Abass et al., 2015; Winkler et al., 2011, 2013) are unlikely to contribute proportionally to the shear stiffness by their out-of-tangential distribution and the link may not be as direct as the established, and accepted, relationships of relative stiffness observed across the surface.

The derived stiffness of the isotropic matrix for the models in Chapter 4 is measured in combination the mechanical effects of the ILC fibril representation as a relationship between stress and shear strain angle. This strain measurement cannot be directly related to the tensile stiffness resulting from the representation of lamellee collagen fibrils due to: (1) the difference in stiffness measurement derived from the difference in the strain measurement (shear strain angle and elongation vs shear and direct uniaxial stiffness respectively) and (2) the contribution to uniaxial direct stiffness in the tangential plane from the isotropically represented non-fibril matrix. The model represents experimental behaviour of shear and tangential mechanical responses. By doing so, a measurement of a non-fibrilar isotropic matrix stiffness which was $2-3$ orders of magnitude lower than the fibril contribution was derived. This observation was indicated by the relationship between the shear and direct stiffnesses as described above. Due to the stated

limitations of this comparison, it was necessary to assess this relationship further. Figure 4.13 provides the stress vs strain relationships for various locations and directions across the cornea. A fibril density function was introduced in Chapter 4 to represent the known regional variation of collagen fibril density and also provides a mechanism to assess the relationship between non-fibrilar matrix stiffness and collagen fibril stiffness contributions. In this study models without variation of density were assessed. It was shown that there was an almost linear relationship between the magnitude of the density function parameter ρ and the direct stiffness. As described above the isotropic non-fibrilar matrix and ILC fibril representations also contribute to the direct stiffness. It follows that a isotropic non-fibrilar matrix which is unaffected by the density function (Chapter 4) must provide very little contribution to direct tangential stiffness if the measured linear relationship resulting from the density function is to be achieved.

Relationships describing the relative fibril density across the surface of the cornea where extracted from experimental WAXS data as part of this study. The constitutive models introduced in this present study introduced numerical representations describing these density variations. Previous studies have omitted these known relationships which are known to relate to the relative stiffness. An important aspect of the inclusion of this characteristic in the model relates to the physiologic condition of central and peripheral corneal stiffness and therefore deformation. The cornea acts to absorb dynamic changes in IOP such as those resulting from OPA etc. (further details can be found in Chapter 1). The cornea is able to provide this dynamic mechanical behaviour and maintain a central topography which provides two-thirds of the optical power of the eye. During increases in IOP the cornea deforms. Due to the relative lower stiffness of the peripheral cornea this region deforms more than the central cornea. The central 4mm of the cornea is the primary region of vision and therefore the cornea's ability to absorb deformation outside this region acts to maintain visual quality during changes of IOP. It was therefore important to include this characteristic within models. Further, the work presented in this study is a significant development in the accuracy of numerical simulations.

The models and tools developed in this present study are suitable for simple modification to describe through-thickness variations as they become characteristically defined. The ability to model such features would likely be of most benefit when modelling surgery such as keratotomy were the anterior arrangement, which is being shown to exhibit greater relative density of fibrils (Abass et al., 2015), becomes discontinuous and therefore contributes less to the overall stiffness.

The experimental study highlighted the importance of accurately describing the circumferential (latitudinal) variation of mechanical properties. Collagen arrangements have been characterised by a number of methods, however, the most accepted is by X-ray scattering. Characteristic relationships describing the arrangement of collagen fibrils in the cornea have been developed, using this technique, over many years of study, including early studies by (Newton and Meek, 1998). It is hypothesised that the application of characteristic collagen arrangement data to the whole-eye globe will improve the accuracy of this area of numerical representation. Currently, the characteristic relationships required are not available for the human sclera. This task is made more complex due to the relative complexity of the collagen arrangement in the sclera compared to the cornea. This is evidenced by Pijanka et al. (2013) who performed WAXS to determine collagen arrangement on a single human eye globe specimen.

The experimental study of intact eye globes suggested that preconditioning cycles may not be required. An objective of this study was to provide a method for determining the material stiffness of the eye globe which more accurately represents *in vivo* state. The realignment of collagen fibrils during load cycles can be considered a mircostructural effect of surgical manipulation and occurs in non-physiological loading conditions as evidenced by Quinn and Winkelstein (2011) and Tonge et al. (2013). During experimental testing of ocular tissue in a non-physiological state, such as on separated corneas, preconditioning effects are known to stiffen the tissue. As a time-dependent behaviour, the process of preconditioning interferes with the observation of natural

viscoelastic behaviour, which is also a time-dependent characteristic. In the future, it is expected that experimental studies which present true characteristic stress-strain relationships will be *ex vivo* intact eye globe tests and *in vivo* clinical measurements.

This study introduced the first viscoelastic anisotropic hyperelastic model for ocular tissue, which was calibrated to a large data set of *ex vivo* human corneas. To build on this progression of numerical representation, new experimental data is required. This should include equilibrium state responses unaffected by fibre realignment, as discussed above, and further strain-rate-variable data.

Studies presenting viscoelastic models of the cornea are currently very limited. The present study hopes to address this. Trials to determine appropriate constitutive parameters included the investigation of the behaviour of the order of the viscoelastic contribution. It was found that a second order model was required to accurately represent the changes in response in the younger age-groups. The best fit models for single order viscoelastic contributions can be seen in Figure 5.1.

While the quantitative fit is reasonable but not desirable ($< 6\%$ RMS error), a qualitative assessment of the fit shows an overestimation of displacement at low IOP and underestimation at higher IOP for the $50-65$ age-groups with a reversal of this trend when representing the $80-95$ age-group. This is not a desirable representation and therefore a second order viscoelastic contribution was trialled which was shown to better represent the rate-dependant behaviour in younger ages.

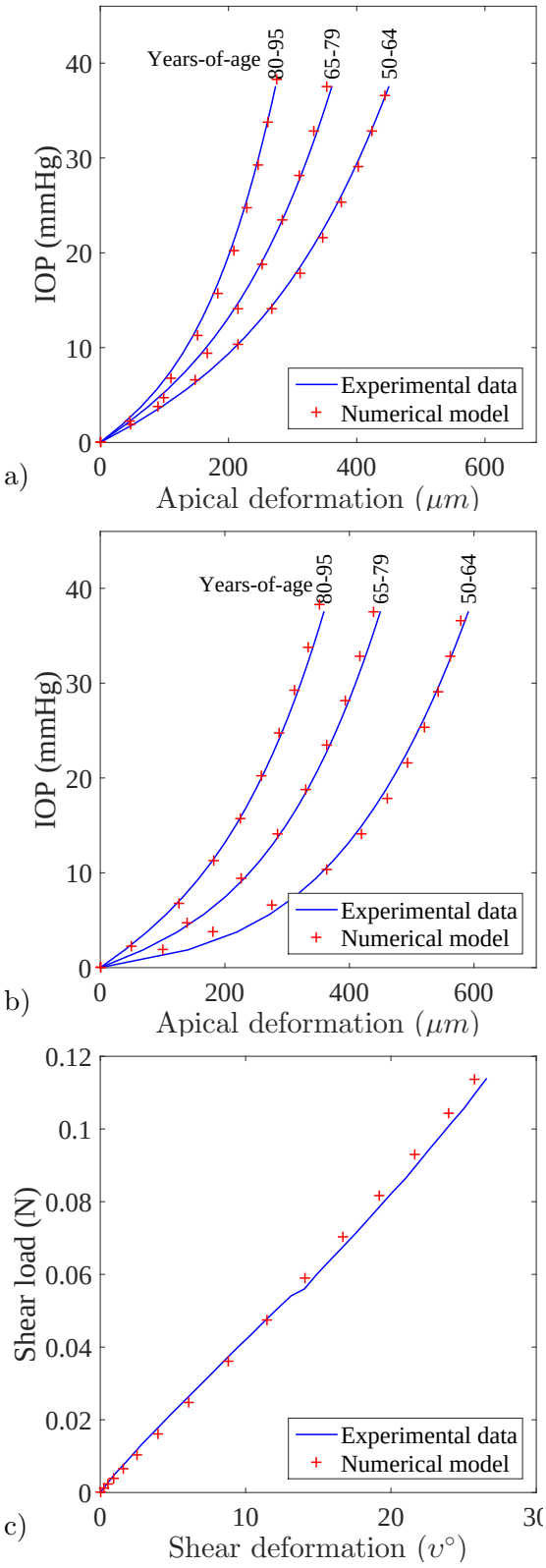

Figure 5.1: Characteristic experimental data and results of numerical simulation of a single order viscoelastic model: (a) corneal inflation at 37.5 mmHg/min, (b) corneal inflation at 3.75 mmHg/min and (c) corneal shear at 10% /min deformation

Chapter 6

Conclusions

This present study significantly progressed the understand of biomechanical properties of the ocular globe through *ex vivo* testing and multiscale numerical modelling. In conclusion:

1. a novel test procedure was developed which provided strain distribution across the intact eye globe and, more closely than before, represented physiological conditions;
2. the generation of bespoke software and non-contact image analysis provided specimen specific geometric models which replicated the complex geometry with a mean error of 49 μm;
3. the regional variation of mechanical behaviour across the intact eye globe was calculated for human and porcine eye globes;
4. a new constitutive model of the human cornea was developed which represented age-related stiffening, 3D anisotropy and inhomogeneity, where:
   (a) the model was fitting to an extensive database of 121 human corneas;
   (b) the shear stiffness was discovered and modelled to be $2-3$ orders of magnitude lower than the tangential tensile stiffness;

(c) existing WAXS data describing regional variation of collagen content was modulated for variation in stromal thickness and therefore deriving density relationships;

(d) the introduction of regional variation of density in an anisotropic model showed that the stiffness was modified by upto to 21% compared with the assumption of consistent density distribution in earlier studies;

(e) the variation in stiffness controlling corneal inflation behaviour was described with an accuracy $< 1.5\%$ as a function of age ranging from $50 - 95$ years.

5. the creation of a second new constitutive model based on the continuum mechanics theory represented the viscoelastic response of the human cornea which:

   (a) was simultaneously calibrated to three different loading scenarios / rates;

   (b) accurately described experimental data across three age-groups with an error $< 3\%$;

   (c) a second order viscoelastic model was demonstrated to be more suitable for modelling age-groups younger than 80 years-of-age;

   (d) the model demonstrated that the rate of decay and initial proportion of viscoelastic contributions decayed with age.

6.1 Recommendations for Future Work

Experimental data relating to the shear behaviour of the stroma is limited and there is a need to measure material properties of the ocular vessel, and in particular the cornea, *in vivo*. These two factors are related as the most likely avenue to measure material properties *in vivo* which is non-contact tomometry. This method involves significant bending of the cornea with large shear strains (as described in Chapter 4). A fuller understanding of shear behaviour in relation to factors such as ageing and fibril alignment would benefit numerical simulations which could lead to tools capable of deriving material properties of the cornea from techniques such as non-contact tonometry.

The experimental data utilised to calibrate the viscoelastic model included three different loading rates (two inflation and one shear). There is currently a gap in the knowledge regarding very slow loading rate data which could be used to calibrate equilibrium responses. Modelling equilibrium responses prior to viscoelastic responses would provide a more scientific bases for viscoelastic analysis and would be expected to result in more accurate simulations across a wider range of strain-rates. Further, once the stiffness contribution from microstructural arrangements is represented numerically together with equilibrium and viscoelastic responses it is likely that isolation of fibril realignment effects which have contributed to stiffening observed in *ex vivo* studies such as (Elsheikh and Anderson, 2005) will be possible. These studies, which advanced in numerical representation, have the potential to include mechanobiology models to represent fibril realignment in the time domain. Such models are predicted to be of great benefit in modelling surgeries such as refractive surgery.

The methodology developed in this study, and the methodologies of many similar studies investigated in earlier chapters, utilise 2D DIC techniques to acquire measurements of displacement and deformation which relate to strain. It is recommended for future work that the methods developed in this study are expanded to utilise 3D DIC which has the benefits of: (1) being able to measure deformation across the full field of view in contrast to the horizon plane, (2) having measurements with a closer link to tissue strain which would be expected to reduce errors in the analysis stages of a study, and (3) if multiple 3D topography maps where obtained and combined a more geometrically representative model could be generated. These three factors would be expected to improve the accuracy numerical simulations.

Appendix A

LabVIEW Control Software

Appendix B

Experimental Preparation Procedure

Appendix C

Element Selection Results

Bibliography

Abaqus, 2013a. Abaqus Analysis User's Manual. Dassault Systems, Providence, USA.

Abaqus, 2013b. Abaqus Theory Manual.

Abaqus, 2013c. Abaqus User Subroutine Reference Manual. Dassault Systems, Providence, USA.

Abass, A., Hayes, S., White, N., Sorensen, T., Meek, K. M., Meek, K. M., mar 2015. Transverse depth-dependent changes in corneal collagen lamellar orientation and distribution. Journal of the Royal Society, Interface / the Royal Society 12 (104), 20140717.

Aghaian, E., Choe, J. E., Lin, S., Stamper, R. L., dec 2004. Central corneal thickness of Caucasians, Chinese, Hispanics, Filipinos, African Americans, and Japanese in a glaucoma clinic. Ophthalmology 111 (12), 2211–9.

Aghamohammadzadeh, H., Newton, R. H., Meek, K. M., feb 2004. X-ray scattering used to map the preferred collagen orientation in the human cornea and limbus. Structure 12 (2), 249–56.

Alastrue, V., Calvo, B., Pena, E., Doblare, M., 2006. Biomechanical Modeling of Refractive Corneal Surgery. Journal of Biomechanical Engineering 128 (1), 150.

Anderson, K., El-Sheikh, a., Newson, T., nov 2004. Application of structural analysis to the mechanical behaviour of the cornea. Journal of the Royal Society, Interface / the Royal Society 1 (1), 3–15.

Avetisov, E. S., Savitskaya, N. F., Vinetskaya, M. I., Iomdina, E. N., jan 1983. A study of biochemical and biomechanical qualities of normal and myopic eye sclera in humans of different age groups. Metabolic, Pediatric, and Systemic Ophthalmology 7 (4), 183–8.

Baba, T., Ohno-Matsui, K., Futagami, S., Yoshida, T., Yasuzumi, K., Kojima, A., Tokoro, T., Mochizuki, M., mar 2003. Prevalence and characteristics of foveal retinal detachment without macular hole in high myopia. American Journal of Ophthalmology 135 (3), 338–342.

Bailey, M. D., mar 2011. How should we measure the ciliary muscle? Investigative Ophthalmology & Visual Science 52 (3), 1817–8.

Baker, T. Y., sep 1943. Ray tracing through non-spherical surfaces.

Bao, F., Deng, M., Wang, Q., Huang, J., Yang, J., Whitford, C., Geraghty, B., Yu, A., Elsheikh, A., 2015. Evaluation of the relationship of corneal biomechanical metrics with physical intraocular pressure and central corneal thickness in ex vivo rabbit eye globes. Experimental Eye Research 137 (August), 11–17.

Baskaran, M., Raman, K., Ramani, K. K., Roy, J., Vijaya, L., Badrinath, S. S., aug 2006. Intraocular pressure changes and ocular biometry during Sirsasana (headstand posture) in yoga practitioners. Ophthalmology 113 (8), 1327–32.

Bayless, K. J., Kwak, H.-I., Su, S.-C., jan 2009. Investigating endothelial invasion and sprouting behavior in three-dimensional collagen matrices. Nature protocols 4 (12), 1888–98.

Bell, J., Hayes, S., Whitford, C., Elshiekh, A., Meek, K. M., 2016. Hierarchical changes in corneal collagen structure under load. In: The Association for Research in Vision and Ophthalmology. Baltimore.

Bennet, A., Rabbetts, R., 1989. Clinical Visual Optics, vol. 2 Edition. Butterworths, London.

Berman, E. R., jul 1991. Biochemistry of the eye, 1st Edition. Vol. 19. Plenum Press, New York, New York, USA.

Boote, C., Dennis, S., Newton, R. H., Puri, H., Meek, K. M., jul 2003. Collagen fibrils appear more closely packed in the prepupillary cornea: optical and biomechanical implications. Investigative Ophthalmology & Visual Science 44 (7), 2941–8.

Boote, C., Hayes, S., Abahussin, M., Meek, K. M., mar 2006. Mapping collagen organization in the human cornea: left and right eyes are structurally distinct. Investigative Ophthalmology & Visual Science 47 (3), 901–908.

Boote, C., Hayes, S., Young, R. D., Kamma-Lorger, C. S., Hocking, P. M., Elsheikh, A., Inglehearn, C. F., Ali, M., Meek, K. M., may 2009. Ultrastructural changes in the retinopathy, globe enlarged (rge) chick cornea. Journal of Structural Biology 166 (2), 195–204.

Borcherding, M. S., Blacik, L. J., Sittig, R. a., Bizzell, J. W., Breen, M., Weinstein, H. G., jul 1975. Proteoglycans and collagen fibre organization in human corneoscleral tissue. Experimental Eye Research 21 (1), 59–70.

Boschetti, F., Triacca, V., Spinelli, L., Pandolfi, a., mar 2012. Mechanical Characterization of Porcine Corneas. Journal of Biomechanical Engineering 134 (3), 031003.

Boyce, B. L., Grazier, J. M., Jones, R. E., Nguyen, T. D., oct 2008. Full-field deformation of bovine cornea under constrained inflation conditions. Biomaterials 29 (28), 3896–3904.

Boyce, B. L., Jones, R. E., Nguyen, T. D., Grazier, J. M., jan 2007. Stress-controlled viscoelastic tensile response of bovine cornea. Journal of Biomechanics 40 (11), 2367–76.

Bragg, M., Fara, P., Ayliffe, W., Lliffe, R., 2014. BBC Radio 4 - In Our Time, The Eye.

Brandt, J. D., apr 2004. Corneal thickness in glaucoma screening, diagnosis, and management. Current Opinion in Ophthalmology 15 (2), 85–9.

Broman, A. T., Quigley, H. a., West, S. K., Katz, J., Munoz, B., Bandeen-Roche, K., Tielsch, J. M., Friedman, D. S., Crowston, J., Taylor, H. R., Varma, R., Leske,

M. C., Bengtsson, B., Heijl, A., He, M., Foster, P. J., jan 2008. Estimating the rate of progressive visual field damage in those with open-angle glaucoma, from cross-sectional data. Investigative Ophthalmology & Visual Science 49 (1), 66–76.

Bron, A., Tripathi, R., 1998. Wolff's Anatomy of the eye and orbit, 8th Edition. Taylor & Francis.

Bron, A. M., Creuzot-Garcher, C., Goudeau-Boutillon, S., D'Athis, P., mar 1999. Falsely elevated intraocular pressure due to increased central corneal thickness. Graefe's Archive for Clinical and Experimental Ophthalmology 237 (3), 220–4.

Brubaker, R. F., Ezekiel, S., Chin, L., Young, L., Johnson, S. A., Beeler, G. W., 1975. The stress-strain behavior of the corneoscleral envelope of the eye I. Development of a system for making in vivo measurements using optical interferometry. Experimental Eye Research 21 (1), 37–46.

Brubaker, R. F., Johnson, S. A., Beeler, G. W., 1977. The stress-strain behavior of the corneoscleral envelope of the eye II. In vivo measurements in rhesus monkey eyes. Experimental Eye Research 24 (5), 425–435.

Bryant, M. R., McDonnell, P. J., 1996. Constitutive laws for biomechanical modeling of refractive surgery. Journal of biomechanical engineering 118 (4), 473–481.

Burd, H. J., Judge, S. J., Cross, J. A., 2002. Numerical modelling of the accommodating lens. Vision Research 42 (18), 2235–2251.

Chen, M.-J., Liu, Y.-T., Tsai, C.-C., Chen, Y.-C., Chou, C.-K., Lee, S.-M., mar 2009. Relationship between central corneal thickness, refractive error, corneal curvature, anterior chamber depth and axial length. Journal of the Chinese Medical Association : JCMA 72 (3), 133–7.

Cheng, S., Clarke, E. C., Bilston, L. E., jun 2009. The effects of preconditioning strain on measured tissue properties. Journal of biomechanics 42 (9), 1360–2.

Cheung, S. W., Cho, P., Douthwaite, W., mar 2000. Corneal shape of Hong Kong-Chinese. Ophthalmic & physiological optics : the journal of the British College of Ophthalmic Opticians (Optometrists) 20 (2), 119–25.

Christensen, R., 1982. Theory of viscoelasticity: an introduction, 2nd Edition. Elsevier, New York.

Cogan, D. G., 1951. Applied anatomy and physiology of the cornea. Transactions - American Academy of Ophthalmology and Otolaryngology. American Academy of Ophthalmology and Otolaryngology 55, 329–59.

Congdon, N. G., Broman, A. T., Bandeen-Roche, K., Grover, D., Quigley, H. a., may 2006. Central corneal thickness and corneal hysteresis associated with glaucoma damage. American Journal of Ophthalmology 141 (5), 868–75.

Coudrillier, B., Tian, J., Alexander, S., Myers, K. M., Quigley, H. A., Nguyen, T. D., apr 2012. Biomechanics of the human posterior sclera: age- and glaucoma-related changes measured using inflation testing. Investigative Ophthalmology & Visual Science 53 (4), 1714–28.

Cui, Y.-h., Huang, J.-f., Cheng, S.-y., Wei, W., Shang, L., Li, N., Xiong, K., 2015. Study on establishment and mechanics application of finite element model of bovine eye. BMC ophthalmology 15, 1–16.

Curtin, B. J., jan 1969. Physiopathologic aspects of scleral stress-strain. Transactions of the American Ophthalmological Society 67, 417–61.

Darrigol, O., 2012. A History of Optics from Greek Antiquity to the Nineteenth Century. OUP Oxford.

Daxer, A., Misof, K., Grabner, B., Ettl, A., Fratzl, P., mar 1998. Collagen fibrils in the human corneal stroma: structure and aging. Investigative Ophthalmology & Visual Science 39 (3), 644–8.

Doughty, M. J., Jonuscheit, S., apr 2007. An assessment of regional differences in corneal thickness in normal human eyes, using the Orbscan II or ultrasound pachymetry. Optometry 78 (4), 181–90.

Downs, J. C., Suh, J.-K. F., Thomas, K. a., Bellezza, A. J., Burgoyne, C. F., Hart, R. T., 2003. Viscoelastic Characterization of Peripapillary Sclera: Material Properties by

Quadrant in Rabbit and Monkey Eyes. Journal of Biomechanical Engineering 125 (1), 124.

Downs, J. C., Suh, J.-K. F., Thomas, K. a., Bellezza, A. J., Hart, R. T., Burgoyne, C. F., feb 2005. Viscoelastic material properties of the peripapillary sclera in normal and early-glaucoma monkey eyes. Investigative Ophthalmology & Visual Science 46 (2), 540–6.

Dua, H. S., Faraj, L. A., Said, D. G., Gray, T., Lowe, J., may 2013. Human corneal anatomy redefined: a novel pre-Descemet's layer (Dua's layer). Ophthalmology 120 (9), 1778–85.

Dubbelman, M., Weeber, H. a., van der Heijde, R. G. L., Völker-Dieben, H. J., aug 2002. Radius and asphericity of the posterior corneal surface determined by corrected Scheimpflug photography. Acta Ophthalmologica Scandinavica 80 (4), 379–83.

Dupps, W. J., Wilson, S. E., oct 2006. Biomechanics and Wound Healing in the Cornea.

Elsheikh, A., Alhasso, D., jun 2009. Mechanical anisotropy of porcine cornea and correlation with stromal microstructure. Experimental Eye Research 88 (6), 1084–91.

Elsheikh, A., Alhasso, D., Gunvant, P., Garway-Heath, D., 2011a. Multiparameter correction equation for Goldmann applanation tonometry. Optometry & Vision Science 88 (1), 102–112.

Elsheikh, A., Alhasso, D., Rama, P., feb 2008a. Assessment of the epithelium's contribution to corneal biomechanics. Experimental Eye Research 86 (2), 445–51.

Elsheikh, A., Alhasso, D., Rama, P., may 2008b. Biomechanical properties of human and porcine corneas. Experimental eye research 86 (5), 783–90.

Elsheikh, A., Anderson, K., jun 2005. Comparative study of corneal strip extensometry and inflation tests. Journal of the Royal Society, Interface / the Royal Society 2 (3), 177–85.

Elsheikh, A., Brown, M., Alhasso, D., Rama, P., Campanelli, M., Garway-Heath,

D., feb 2008c. Experimental assessment of corneal anisotropy. Journal of Refractive Surgery 24 (2), 178–87.

Elsheikh, A., Geraghty, B., Alhasso, D., Knappett, J., Campanelli, M., Rama, P., may 2010a. Regional variation in the biomechanical properties of the human sclera. Experimental Eye Research 90 (5), 624–33.

Elsheikh, A., Geraghty, B., Rama, P., Campanelli, M., Meek, K. M., oct 2010b. Characterization of age-related variation in corneal biomechanical properties. Journal of the Royal Society, Interface / the Royal Society 7 (51), 1475–1485.

Elsheikh, A., Kassem, W., Jones, S. W., jan 2011b. Strain-rate sensitivity of porcine and ovine corneas. Acta of bioengineering and biomechanics / Wrocław University of Technology 13 (2), 25–36.

Elsheikh, A., McMonnies, C. W., Whitford, C., Boneham, G. C., 2015. In vivo study of corneal responses to increased intraocular pressure loading. Eye and Vision 2 (1), 20.

Elsheikh, A., Ross, S., Alhasso, D., Rama, P., jan 2009. Numerical study of the effect of corneal layered structure on ocular biomechanics. Current Eye Research 34 (1), 26–35.

Elsheikh, A., Wang, D., apr 2007. Numerical modelling of corneal biomechanical behaviour. Computer methods in biomechanics and biomedical engineering 10 (2), 85–95.

Elsheikh, A., Wang, D., Brown, M., Rama, P., Campanelli, M., Pye, D., jan 2007a. Assessment of corneal biomechanical properties and their variation with age. Current Eye Research 32 (1), 11–19.

Elsheikh, A., Wang, D., Kotecha, A., Brown, M., Garway-Heath, D., oct 2006. Evaluation of Goldmann applanation tonometry using a nonlinear finite element ocular model. Annals of Biomedical Engineering 34 (10), 1628–40.

Elsheikh, A., Wang, D., Pye, D., oct 2007b. Determination of the modulus of elasticity of the human cornea. Journal of refractive surgery (Thorofare, N.J. : 1995) 23 (8), 808–18.

Elsheikh, A., Wang, D., Rama, P., Campanelli, M., Garway-Heath, D., mar 2008d. Experimental assessment of human corneal hysteresis. Current Eye Research 33 (3), 205–13.

Elsheikh, A., Whitford, C., Hamarashid, R., Kassem, W., Joda, A., Büchler, P., feb 2013. Stress free configuration of the human eye. Medical engineering & physics 35 (2), 211–6.

Epstein, M., 2012. The elements of continuum biomechanics. John Wiley & Sons.

Ethier, C. R., Johnson, M., Ruberti, J., jan 2004. Ocular biomechanics and biotransport. Annual Review of Biomedical Engineering 6, 249–273.

Eysteinsson, T., Jonasson, F., Sasaki, H., Arnarsson, A., Sverrisson, T., Sasaki, K., Stefánsson, E., feb 2002. Central corneal thickness, radius of the corneal curvature and intraocular pressure in normal subjects using non-contact techniques: Reykjavik eye study. Acta Ophthalmologica Scandinavica 80 (1), 11–5.

Fatt, I., 1978. Physiology of the eye: An introduction to the vegetative functions. Butterworths, London.

Forrester, J. V., 1996. The eye: basic sciences in practice. W.B. Saunders.

Francis, B. a., Hsieh, A., Lai, M.-Y., Chopra, V., Pena, F., Azen, S., Varma, R., jan 2007. Effects of corneal thickness, corneal curvature, and intraocular pressure level on Goldmann applanation tonometry and dynamic contour tonometry. Ophthalmology 114 (1), 20–26.

Freegard, T. J., jan 1997. The physical basis of transparency of the normal cornea. Eye 11 (Pt 4), 465–471.

Friberc, R., Lace, W., 1988. of the Elastic Properties and Sclera of Human Choroid. Experimental Eye Research 47, 429–436.

Fung, Y. C., dec 1967. Elasticity of soft tissues in simple elongation. The American Journal of Physiology 213 (6), 1532–44.

Fung, Y.-C., 1990. Biomechanics: motion, flow, stress and growth. Springer, New York, New York, USA.

Galgauskas, S., Norvydaite, D., Krasauskaite, D., Stech, S., Stanislovas Ašoklis, R., oct 2013. Age-related changes in corneal thickness and endothelial characteristics. Clinical Interventions in Aging 8, 1445.

Gasser, T. C., Ogden, R. W., Holzapfel, G. a., mar 2006. Hyperelastic modelling of arterial layers with distributed collagen fibre orientations. Journal of the Royal Society, Interface / the Royal Society 3 (6), 15–35.

Gee, M. W., Förster, C., Wall, W. A., jan 2010. A computational strategy for prestressing patient-specific biomechanical problems under finite deformation. International Journal for Numerical Methods in Biomedical Engineering 26 (1), 52–72.

Geraghty, B., 2012. Biomechanical behaviour of the cornea and sclera. Ph.D. thesis, University of Dundee.

Geraghty, B., Jones, S. W., Rama, P., Akhtar, R., Elsheikh, A., 2012. Age-related variations in the biomechanical properties of human sclera. Journal of the Mechanical Behavior of Biomedical Materials 16 (1), 181–191.

Geraghty, B., Whitford, C., Boote, C., Akhtar, R., Elsheikh, A., 2015. Age-related variation on the biomechanical and structural properties of the corneo-scleral tunic. In: Derby, B., Akhtar, R. (Eds.), Mechanical properties of aging soft tissues. Springer, Ch. 9, pp. 207–235.

Girard, M. J. a., Downs, J. C., Bottlang, M., Burgoyne, C. F., Suh, J.-K. F., may 2009a. Peripapillary and posterior scleral mechanics–part II: experimental and inverse finite element characterization. Journal of biomechanical engineering 131 (5), 051012.

Girard, M. J. a., Downs, J. C., Burgoyne, C. F., Suh, J.-K. F., aug 2008. Experimental surface strain mapping of porcine peripapillary sclera due to elevations of intraocular pressure. Journal of biomechanical engineering 130 (4), 041017.

Girard, M. J. a., Downs, J. C., Burgoyne, C. F., Suh, J.-K. F., may 2009b. Peripapillary and posterior scleral mechanics–part I: development of an anisotropic hyperelastic constitutive model. Journal of biomechanical engineering 131 (5), 051011.

Girton, T. S., Barocas, V. H., Tranquillo, R. T., oct 2002. Confined compression of a tissue-equivalent: collagen fibril and cell alignment in response to anisotropic strain. Journal of biomechanical engineering 124 (5), 568–75.

Glass, D. H., Roberts, C. J., Litsky, A. S., Weber, P. a., sep 2008. A viscoelastic biomechanical model of the cornea describing the effect of viscosity and elasticity on hysteresis. Investigative ophthalmology & visual science 49 (9), 3919–26.

Glasser, A., Kaufman, P. L., 1999. The mechanism of accommodation in primates. Ophthalmology 107 (5), 221–222.

Govindjee, S., Mihalic, P. A., nov 1998. Computational methods for inverse deformations in quasi-incompressible finite elasticity. International Journal for Numerical Methods in Engineering 43 (5), 821–838.

Govrin-Yehudain, J., Levanon, D., Hirshowitz, B., mar 1986. Collagen Fiber Alignment in the Human Preauricular Dermis Before and After Rhytidectomy-A Scanning Electron Microscopy Study. Annals of Plastic Surgery 16 (3), 200–203.

Greene, P., 1985. Stress-strain behavior exponential strips. Bulletin of Mathematical Biology 47 (6), 757–764.

Groves, R. B., Coulman, S. A., Birchall, J. C., Evans, S. L., jan 2012. Quantifying the mechanical properties of human skin to optimise future microneedle device design. Computer methods in biomechanics and biomedical engineering 15 (1), 73–82.

Grytz, R., Downs, J. C., jan 2012. A forward incremental prestressing method with application to inverse parameter estimations and eye-specific simulations of posterior scleral shells. Computer methods in biomechanics and biomedical engineering (January), 37–41.

Grytz, R., Meschke, G., oct 2009. Constitutive modeling of crimped collagen fibrils in soft tissues. Journal of the mechanical behavior of biomedical materials 2 (5), 522–533.

Grytz, R., Meschke, G., apr 2010. A computational remodeling approach to predict the physiological architecture of the collagen fibril network in corneo-scleral shells. Biomechanics and modeling in mechanobiology 9 (2), 225–235.

He, M., Zeng, J., Liu, Y., Xu, J., Pokharel, G. P., Ellwein, L. B., mar 2004. Refractive error and visual impairment in urban children in southern china. Investigative Ophthalmology & Visual Science 45 (3), 793–9.

Hjortdal, J. O., jul 1996. Regional elastic performance of the human cornea. Journal of Biomechanics 29 (7), 931–42.

Hjortdal, J. O., Jensen, P. K., feb 1995. In vitro measurement of corneal strain, thickness, and curvature using digital image processing. Acta ophthalmologica Scandinavica 73 (1), 5–11.

Hoeltzel, D. A., Altman, P., Buzard, K., Choe, K., may 1992. Strip extensiometry for comparison of the mechanical response of bovine, rabbit, and human corneas. Journal of biomechanical engineering 114 (2), 202–215.

Holzapfel, G., Gasser, T., Stadler, M., jan 2002. A structural model for the viscoelastic behavior of arterial walls: Continuum formulation and finite element analysis. European Journal of Mechanics - A/Solids 21 (3), 441–463.

Holzapfel, G. A., 2000. Nonlinear solid mechanics: a continuum approach for engineering, 1st Edition. Wiley.

Holzapfel, G. A., Gasser, T. C., 2001. A viscoelastic model for fiber-reinforced composites at finite strains: Continuum basis, computational aspects and applications. Computer methods in applied mechanics and ... 190.

Holzapfel, G. A., Gasser, T. C., Ogden, R. A. Y. W., 2000. A new constitutive framework for arterial wall mechanics and a comparative study of material models. Journal of Elasticity (61), 1–48.

Howland, H. C., Rand, R. H., Lubkin, S. R., 1992. A thin-shell model of the cornea and its application to corneal surgery. Refractive & corneal surgery .

Huff, T. E., 2003. The Rise of Early Modern Science: Islam, China and the West. Cambridge University Press.

Humphrey, J. D., jan 2003. Review Paper: Continuum biomechanics of soft biological tissues. Proceedings of the Royal Society A: Mathematical, Physical and Engineering Sciences 459 (2029), 3–46.

Ings, S., 2008. The Eye: A Natural History. Bloomsbury.

Irgens, F., 2008. Continuum mechanics. Springer, Berlin.

Jayasuriya, a. C., Scheinbeim, J. I., Lubkin, V., Bennett, G., Kramer, P., aug 2003. Piezoelectric and mechanical properties in bovine cornea. Journal of biomedical materials research. Part A 66 (2), 260–5.

Jaycock, P. D., Lobo, L., Ibrahim, J., Tyrer, J., Marshall, J., jan 2005. Interferometric technique to measure biomechanical changes in the cornea induced by refractive surgery. Journal of cataract and refractive surgery 31 (1), 175–84.

Jonuscheit, S., Doughty, M. J., Button, N. F., mar 2007. On the use of Orbscan II to assess the peripheral corneal thickness in humans: a comparison with ultrasound pachometry measures. Ophthalmic & Physiological Optics 27 (2), 179–89.

Jue, B., Maurice, D. M., Ophthalmology, D., Stanford, M., jan 1991. The mechanical properties of the rabbit and human cornea. Journal of Biomechanics 24 (9), 869–872.

Kampmeier, J., Radt, B., Birngruber, R., Brinkmann, R., 2000. Thermal and biomechanical parameters of porcine cornea. Cornea .

Kapnisis, K., Doormaal, M. V., Ross Ethier, C., nov 2009. Modeling aqueous humor collection from the human eye. Journal of Biomechanics 42 (15), 2454–7.

Kaufmann, C., Bachmann, L. M., Robert, Y. C., Thiel, M. A., aug 2006. Ocular pulse amplitude in healthy subjects as measured by dynamic contour tonometry. Archives of Ophthalmology 124 (8), 1104–8.

Keeley, F. W., Morin, J. D., Vesely, S., nov 1984. Characterization of collagen from normal human sclera. Experimental Eye Research 39 (5), 533–42.

Kennedy, R. H., Bourne, W. M., Dyer, J. A., mar 1986. A 48-year clinical and epidemiologic study of keratoconus. American Journal of Ophthalmology 101 (3), 267–273.

Khan, M. A., feb 2014. Numerical study on human cornea and modified multiparametric correction equation for Goldmann applanation tonometer. Journal of the mechanical behavior of biomedical materials 30, 91–102.

Kling, S., Bekesi, N., Dorronsoro, C., Pascual, D., Marcos, S., jan 2014. Corneal viscoelastic properties from finite-element analysis of in vivo air-puff deformation. PloS one 9 (8), e104904.

Kling, S., Remon, L., Pérez-Escudero, A., Merayo-Lloves, J., Marcos, S., aug 2010. Corneal biomechanical changes after collagen cross-linking from porcine eye inflation experiments. Investigative ophthalmology & visual science 51 (8), 3961–8.

Kobayashi, A. S., Staberg, L. G., Schlegel, W. A., 1973. Viscoelastic properties of human cornea. In: SESA International Congress on Experimental Mechanics. pp. 497–503.

Komai, Y., Ushiki, T., jul 1991. The three-dimensional organization of collagen fibrils in the human cornea and sclera. Investigative Ophthalmology & Visual Science 32 (8), 2244–58.

Kroese, D. P., Brereton, T., Taimre, T., Botev, Z. I., nov 2014. Why the Monte Carlo method is so important today. WIREs Computational Statistics 6 (6), 386–392.

Lanchares, E., Calvo, B., Cristóbal, J. A., Doblaré, M., Aghamohammadzadeh, H., Newton, R., Meek, K., Alastrué, V., Calvo, B., Peña, E., Doblaré, M., Bryant, M., McDonnell, P., Buzard, K., Fernández, D. C., Niazy, A., Kurtz, R., Djotyan, G., Juhasz, T., Cristobal, J., Flory, P., Gardiner, J., Weiss, J., Hobbit, Karlsson and Sorensen, I., Hoeltzel, D., Altman, P., Buzard, D., Choe, K., Holzapfel, G., Holzapfel, G., Gasser, T., Holzapfel, G., Gasser, T., Ogden, R., Munnerlyn, C.,

Koons, S., Marshall, J., Newton, R., Meek, K., Pandolfi, A., Maganiello, F., Pena, E., Calvo, B., Martinez, M., Doblaré, M., Pena, E., Martinez, M., Calvo, B., Doblaré, M., del Palomar, A. P., Doblaré, M., Pinsky, P., Datye, V., Pinsky, P., Heide, D., Chernyak, D., Pioletti, D., Rakotomanana, L., Benvenuti, J., Leyvraz, P., Shin, T., Vito, R., Johnson, L., McCarey, B., Simo, J., Taylor, R., Spencer, A., Tallec, P. L., Rahier, C., Kaiss, A., Velinsky, S., Bryant, M., Vito, R., Shin, T., McCarey, B., Weiss, J., Maker, B., Govindjee, S., 2008. Finite element simulation of arcuates for astigmatism correction. Journal of Biomechanics 41 (4), 797–805.

Lari, D. R., Schultz, D. S., Wang, A. S., Lee, O.-T., Stewart, J. M., jan 2012. Scleral mechanics: comparing whole globe inflation and uniaxial testing. Experimental eye research 94 (1), 128–35.

Leske, M. C., Wu, S.-Y., Hennis, A., Honkanen, R., Nemesure, B., jan 2008. Risk factors for incident open-angle glaucoma: the Barbados Eye Studies. Ophthalmology 115 (1), 85–93.

Li, L.-y. Y., Tighe, B., feb 2007. Nonlinear analysis of static axisymmetric deformation of the human cornea. Computational Materials Science 38 (4), 618–624.

Lin, L.-K. L., Shih, Y.-F. F., Hsiao, C. K., Chen, C.-J. J., Lee, L.-A. A., Hung, P.-T. T., oct 2001. Epidemiologic study of the prevalence and severity of myopia among schoolchildren in Taiwan in 2000. Journal of the Formosan Medical Association = Taiwan yi zhi 100 (10), 684–91.

Lin, L. L. K., Shih, Y. F., Hsiao, C. K., Chen, C. J., jan 2004. Prevalence of myopia in Taiwanese schoolchildren: 1983 to 2000. Annals of the Academy of Medicine, Singapore 33 (1), 27–33.

Lu, J., Zhou, X., Raghavan, M. L., jan 2007. Inverse elastostatic stress analysis in pre-deformed biological structures: Demonstration using abdominal aortic aneurysms. Journal of biomechanics 40 (3), 693–6.

Ludwig, K., Wegscheider, E., Hoops, J. P., Kampik, A., 1999. In vivo imaging of the

human zonular apparatus with high-resolution ultrasound biomicroscopy. Graefe's Archive for Clinical and Experimental Ophthalmology 237 (5), 361–371.

Markert, B., Ehlers, W., Karajan, N., dec 2005. A general polyconvex strain-energy function for fiber-reinforced materials. PAMM 5 (1), 245–246.

Marshall, G. E., Konstas, A. G., Lee, W. R., 1993. Collagens in ocular tissues. The British Journal of Ophthalmology 77 (8), 515–524.

Mattson, M. S., Huynh, J., Wiseman, M., Coassin, M., Kornfield, J. a., Schwartz, D. M., jun 2010. An in vitro intact globe expansion method for evaluation of cross-linking treatments. Investigative ophthalmology & visual science 51 (6), 3120–8.

Mauger, R. R., Likens, C. P., Applebaum, M., jan 1984. Effects of accommodation and repeated applanation tonometry on intraocular pressure. American Journal of Optometry and Physiological Optics 61 (1), 28–30.

Maurice, D., 1969. The cornea and sclera. Academic Press;, New York.

Maurice, D. M., apr 1957. The structure and transparency of the cornea. The Journal of Physiology 136 (2), 263–86.

McMonnies, C. W., mar 2012. Assessing corneal hysteresis using the Ocular Response Analyzer. Optometry and vision science : official publication of the American Academy of Optometry 89 (3), E343–9.

Meek, K. M., Boote, C., mar 2004. The organization of collagen in the corneal stroma. Experimental Eye Research 78 (3), 503–512.

Meek, K. M., Leonard, D. W., jan 1993. Ultrastructure of the corneal stroma: a comparative study. Biophysical Journal 64 (1), 273–80.

Metzler, K. M., Mahmoud, A. M., Liu, J., Roberts, C. J., 2014. Deformation response of paired donor corneas to an air puff: Intact whole globe versus mounted corneoscleral rim. Journal of Cataract and Refractive Surgery 40 (6), 888–896.

Moiseeva, I. N., Stein, A. A., 2013. Investigation of the Pressure Volume Relationship for the Eyeball Loaded by a Thin Rod. Fluid Dynamics 48 (4), 425–434.

Montiani-Ferreira, F., Li, T., Kiupel, M., Howland, H., Hocking, P., Curtis, R., Petersen-Jones, S., sep 2003. Clinical features of the retinopathy, globe enlarged (rge) chick phenotype. Vision Research 43 (19), 2009–2018.

Mooney, M., apr 1940. A Theory of Large Elastic Deformation. Journal of Applied Physics 11 (9), 582.

Moran, R., Smith, J. H., García, J. J., 2014. Fitted hyperelastic parameters for Human brain tissue from reported tension, compression, and shear tests. Journal of biomechanics 47 (15), 3762–6.

Morris, H. J., Tang, J., Cruz Perez, B., Pan, X., Hart, R. T., Weber, P. A., Liu, J., nov 2013. Correlation Between Biomechanical Responses of Posterior Sclera and IOP Elevations During Micro Intraocular Volume Change. Investigative Opthalmology & Visual Science 54 (12), 7215.

Myers, K. M., Coudrillier, B., Boyce, B. L., Nguyen, T. D., nov 2010. The inflation response of the posterior bovine sclera. Acta biomaterialia 6 (11), 4327–35.

Newton, R. H., Meek, K. M., jun 1998. Circumcorneal annulus of collagen fibrils in the human limbus. Investigative Ophthalmology & Visual Science 39 (7), 1125–34.

Nguyen, T. D., Boyce, B. L., jun 2011. An inverse finite element method for determining the anisotropic properties of the cornea. Biomechanics and modeling in mechanobiology 10 (3), 323–337.

Nguyen, T. D., Jones, R. E., Boyce, B. L., aug 2008. A nonlinear anisotropic viscoelastic model for the tensile behavior of the corneal stroma. Journal of biomechanical engineering 130 (4), 041020.

NI, 2016. National Instruments white papers.

Norman, R. E., Flanagan, J. G., Rausch, S. M. K., Sigal, I. a., Tertinegg, I., Eilaghi, A., Portnoy, S., Sled, J. G., Ethier, C. R., feb 2010. Dimensions of the human sclera: thickness measurement and regional changes with axial length. Experimental Eye Research 90 (2), 277–84.

Norman, R. E., Flanagan, J. G., Sigal, I. A., Rausch, S. M. K., Tertinegg, I., Ethier, C. R., jul 2011. Finite element modeling of the human sclera: influence on optic nerve head biomechanics and connections with glaucoma. Experimental Eye Research 93 (1), 4–12.

Ogden, R. W., feb 1972. Large Deformation Isotropic Elasticity - On the Correlation of Theory and Experiment for Incompressible Rubberlike Solids. Proceedings of the Royal Society A: Mathematical, Physical and Engineering Sciences 326 (1567), 565–584.

Ogden, R. W., 1984. Non-Linear Elastic Deformations. Ellis Horwood Limited, Chichester.

Olsen, T. W., Aaberg, S. Y., Geroski, D. H., Edelhauser, H. F., feb 1998. Human sclera: thickness and surface area. American Journal of Ophthalmology 125 (2), 237–41.

Orssengo, G. J., Pye, D. C., may 1999. Determination of the true intraocular pressure and modulus of elasticity of the human cornea in vivo. Bulletin of mathematical biology 61 (3), 551–72.

Oxford English Dictionary, 2014. Oxford English Dictionary Online.

Oyster, C., 1999. The human eye: structure and function. Sinauer Associates Inc., Sunderland.

Pandolfi, A., Fotia, G., Manganiello, F., aug 2008. Finite element simulations of laser refractive corneal surgery. Engineering with Computers 25 (1), 15–24.

Pandolfi, A., Holzapfel, G. a., dec 2008. Three-dimensional modeling and computational analysis of the human cornea considering distributed collagen fibril orientations. Journal of biomechanical engineering 130 (6), 61006.

Pandolfi, A., Manganiello, F., nov 2006. A model for the human cornea: constitutive formulation and numerical analysis. Biomechanics and modeling in mechanobiology 5 (4), 237–46.

Papi, M., Paoletti, P., Geraghty, B., Akhtar, R., mar 2014. Nanoscale characterization of the biomechanical properties of collagen fibrils in the sclera. Applied Physics Letters 104 (10), 103703.

Pepose, J. S., Feigenbaum, S. K., Qazi, M. a., Sanderson, J. P., Roberts, C. J., jan 2007. Changes in corneal biomechanics and intraocular pressure following LASIK using static, dynamic, and noncontact tonometry. American journal of ophthalmology 143 (1), 39–47.

Perez, B. C., Morris, H. J., Hart, R. T., Liu, J., dec 2013. Finite element modeling of the viscoelastic responses of the eye during microvolumetric changes. Journal of biomedical science and engineering 6 (12A), 29–37.

Petsche, S. J., Chernyak, D., Martiz, J., Levenston, M. E., Pinsky, P. M., feb 2012. Depth-dependent transverse shear properties of the human corneal stroma. Investigative ophthalmology & visual science 53 (2), 873–80.

Petsche, S. J., Pinsky, P. M., jan 2013. The role of 3-D collagen organization in stromal elasticity: a model based on X-ray diffraction data and second harmonic-generated images. Biomechanics and modeling in mechanobiology (1938).

Pijanka, J. K., Abass, A., Sorensen, T., Elsheikh, A., Boote, C., oct 2013. A wide-angle X-ray fibre diffraction method for quantifying collagen orientation across large tissue areas: application to the human eyeball coat. Journal of Applied Crystallography 46 (5), 1481–1489.

Pijanka, J. K., Coudrillier, B., Ziegler, K., Sorensen, T., Meek, K. M., Nguyen, T. D., Quigley, H. A., Boote, C., aug 2012. Quantitative mapping of collagen fiber orientation in non-glaucoma and glaucoma posterior human sclerae. Investigative Ophthalmology & Visual Science 53 (9), 5258–70.

Pinsky, P. M., van der Heide, D., Chernyak, D., jan 2005. Computational modeling of mechanical anisotropy in the cornea and sclera. Journal of Cataract & Refractive Surgery 31 (1), 136–45.

Pioletti, D. P., Rakotomanana, L. R., sep 2000. Non-linear viscoelastic laws for soft biological tissues. European Journal of Mechanics - A/Solids 19 (5), 749–759.

Plato, 1971. Timaeus and Critias. Penguin Books.

Qazi, M. a., Sanderson, J. P., Mahmoud, A. M., Yoon, E. Y., Roberts, C. J., Pepose, J. S., oct 2009. Postoperative changes in intraocular pressure and corneal biomechanical metrics Laser in situ keratomileusis versus laser-assisted subepithelial keratectomy. Journal of cataract and refractive surgery 35 (10), 1774–88.

Quinn, K. P., Winkelstein, B. A., 2011. Preconditioning is Correlated With Altered Collagen Fiber Alignment in Ligament. Journal of biomechanical engineering 133 (June 2011), 28–31.

Rashed, R., 1990. A Pioneer in Anaclastics: Ibn Sahl on Burning Mirrors and Lenses. Isis 81 (3), 464.

Read, S. A., Collins, M. J., Sander, B., 2010. Human optical axail length and defocus. Investigative Ophthalmology & Visual Science 51 (12), 6262–9.

Rivlin, R., 1997. Collected Papers of R.S. Rivlin. Springer New York, New York, NY.

Robert, Y. C. A., nov 2007. What do we measure with various techniques when assessing IOP? Survey of Ophthalmology 52 Suppl 2 (November), S105–8.

Roberts, C., 2000. The cornea is not a piece of plastic. Journal of Refractive Surgery 16 (4), 407–13.

Rose, K. a., Morgan, I. G., Smith, W., Burlutsky, G., Mitchell, P., Saw, S.-M., apr 2008. Myopia, lifestyle, and schooling in students of Chinese ethnicity in Singapore and Sydney. Archives of Ophthalmology 126 (4), 527–30.

Roy, A. S., Dupps, W. J., oct 2009. Effects of altered corneal stiffness on native and postoperative LASIK corneal biomechanical behavior: A whole-eye finite element analysis. Journal of Refractive Surgery 25 (10), 875–87.

Roy, A. S., Dupps, W. J., jan 2011. Patient-specific modeling of corneal refractive surgery outcomes and inverse estimation of elastic property changes. Journal of biomechanical engineering 133 (1), 011002.

Sabra, A. I., 1981. Theories of Light, from Descartes to Newton. CUP Archive.

Sánchez, P., Moutsouris, K., Pandolfi, A., 2014. Biomechanical and optical behavior of human corneas before and after photorefractive keratectomy. Journal of Cataract and Refractive Surgery 40 (6), 907–917.

Saude, T., 1993. Ocular anatomy and physiology. Wiley.

Sheppard, A. L., Davies, L. N., dec 2010. In vivo analysis of ciliary muscle morphologic changes with accommodation and axial ametropia. Investigative Ophthalmology & Visual Science 51 (12), 6882–9.

Sheppard, A. L., Davies, L. N., mar 2011. The effect of ageing on in vivo human ciliary muscle morphology and contractility. Investigative ophthalmology & visual science 52 (3), 1809–16.

Siam, A., jan 1969. Macular hole with central retinal detachment in high myopia with posterior staphyloma. The British Journal of Ophthalmology 53 (1), 62–3.

Sigal, I. a., Flanagan, J. G., Ethier, C. R., nov 2005. Factors influencing optic nerve head biomechanics. Investigative ophthalmology & visual science 46 (11), 4189–99.

Spang, M., Sorensen, T., Whitford, C., Elsheikh, A., Boote, C., 2015. Individual-specific microstructural characterisation of human ocular tunics for whole eye numerical modelling. In: The Association for Research in Vision and Ophthalmology.

Stachs, O., Martin, H., Behrend, D., Schmitz, K. P., Guthoff, R., 2006. Three-dimensional ultrasound biomicroscopy, environmental and conventional scanning electron microscopy investigations of the human zonula ciliaris for numerical modelling of accommodation. Graefe's Archive for Clinical and Experimental Ophthalmology 244 (7), 836–844.

Strenk, S. A., Semmlow, J. L., Strenk, L. M., Munoz, P., Gronlund-Jacob, J., DeMarco, J. K., may 1999. Age-related changes in human ciliary muscle and lens: a magnetic resonance imaging study. Investigative Ophthalmology & Visual Science 40 (6), 1162–9.

Studer, H., 2011. Simulation of Refractive Surgery for Optimization of Vision Correction. Ph.D. thesis, University of Bern.

Studer, H., Larrea, X., Riedwyl, H., Büchler, P., mar 2010. Biomechanical model of human cornea based on stromal microstructure. Journal of biomechanics 43 (5), 836–42.

Su, P., Yang, Y., Xiao, J., Song, Y., 2015. Corneal hyper-viscoelastic model: derivations, experiments, and simulations. Acta of Bioengineering and Biomechanics 17 (2), 73–84.

Tamm, E. R., apr 2009. The trabecular meshwork outflow pathways: structural and functional aspects. Experimental Eye Research 88 (4), 648–55.

Tektas, O.-Y., Lütjen-Drecoll, E., apr 2009. Structural changes of the trabecular meshwork in different kinds of glaucoma. Experimental Eye Research 88 (4), 769–75.

Thylefors, B., Négrel, A. D., jan 1994. The global impact of glaucoma. Bulletin of the World Health Organization 72 (3), 323–6.

Tong, P., Fung, Y.-C., jan 1976. The stress-strain relationship for the skin. Journal of Biomechanics 9 (10), 649–657.

Tonge, T. K., Murienne, B. J., Coudrillier, B., Alexander, S., Rothkopf, W., Nguyen, T. D., 2013. Minimal Preconditioning Effects Observed for Inflation Tests of Planar Tissues. Journal of Biomechanical Engineering 135 (11), 114502.

van der Meulen, M. C., Huiskes, R., 2002. Why mechanobiology? Journal of Biomechanics 35 (4), 401–414.

Vieira, G. M., Oliveira, H. B., de Andrade, D. T., Bottaro, M., Ritch, R., sep 2006. Intraocular pressure variation during weight lifting. Archives of Ophthalmology 124 (9), 1251–4.

Wang, R., Raykin, J., Gleason, R. L., Ethier, C. R., Chuong, C., Fung, Y., Takamizawa, K., Hayashi, K., Rachev, A., Hayashi, K., Cardamone, L., Valentín, A., Eberth, J., Humphrey, J., Vaishnav, R., Vossoughi, J., Taber, L., Humphrey, J., Xie, J., Liu, S., Yang, R., Fung, Y., Dou, Y., Fan, Y., Zhao, J., Gregersen, H., Humphrey, J., Rajagopal, K., Omens, J., Fung, Y.-C., Han, H., Fung, Y., Coleman, D., Trokel, S., Ethier, C., Johnson, M., Ruberti, J., Greene, P., Alamouti, B., Funk, J., Tan, C., Ouyang, Y., Ruiz, H., Sadda, S., Olsen, T., Aaberg, S., Geroski, D., Edelhauser, H., Eilaghi, A., Flanagan, J., Tertinegg, I., Simmons, C., Brodland, G., Ethier, C., Chen, K., Rowley, A., Weiland, J., Worthington, K., Wiley, L., Bartlett, A., Stone, E., Mullins, R., Salem, A., Guymon, C., Tucker, B., Holzapfel, G., Sommer, G., Auer, M., Regitnig, P., Ogden, R., Flugel-Koch, C., May, C., Lutjen-Drecoll, E., Humphrey, J., Rachev, A., Greenwald, S., Wang, R., Gleason, R., apr 2015. Residual deformations in ocular tissues. Journal of the Royal Society, Interface / the Royal Society 12 (105), 189–192.

Whitford, C., Studer, H., Boote, C., Meek, K. M., Elsheikh, A., feb 2015. Biomechanical model of the human cornea: Considering shear stiffness and regional variation of collagen anisotropy and density. Journal of the Mechanical Behavior of Biomedical Materials 42 (September 2015), 76–87.

Winkler, M., Chai, D., Kriling, S., Nien, C. J., Brown, D. J., Jester, B., Juhasz, T., Jester, J. V., jan 2011. Nonlinear optical macroscopic assessment of 3-D corneal collagen organization and axial biomechanics. Investigative ophthalmology & visual science 52 (12), 8818–27.

Winkler, M., Shoa, G., Xie, Y., Petsche, S. J., Pinsky, P. M., Brown, D. J., Jester, J. V., Collagen, C., Harmonic, S., Imaging, G., Discovery, T., Foundation, E., Hall, H., 2013. Three-dimensional distribution of transverse collagen fibers in the anterior

human corneal stroma. The Association for Research in Vision and Ophthalmology 13 (13150).

Wong, F. F., Lari, D. R., Schultz, D. S., Stewart, J. M., oct 2012. Whole globe inflation testing of exogenously crosslinked sclera using genipin and methylglyoxal. Experimental eye research 103, 17–21.

Woo, S. L., Kobayashi, A. S., Schlegel, W. A., Lawrence, C., jul 1972. Nonlinear material properties of intact cornea and sclera. Experimental Eye Research 14 (1), 29–39.

Yu, J.-g., Bao, F.-j., Feng, Y.-f., Whitford, C., Ye, T., Huang, Y.-b., Wang, Q.-m., Elsheikh, A., 2013. Assessment of Corneal Biomechanical Behavior Under Posterior and Anterior Pressure. Journal of Refractive Surgery 29 (1), 64.71.

Zavala, J., López Jaime, G. R., Rodríguez Barrientos, C. A., Valdez-Garcia, J., may 2013. Corneal endothelium: developmental strategies for regeneration. Eye 27 (5), 579–88.